The Thesis Committee for Brian William Willsey
Certifies that this is the approved version of the following thesis:

Reaction Controlled Kinetic Assembly of Small Gold Nanoclusters with High NIR Extinction

APPROVED BY
SUPERVISING COMMITTEE:

Keith P. Johnston, Supervisor

Thomas E. Milner

Reaction Controlled Kinetic Assembly of Small Gold Nanoclusters with High NIR Extinction

by

Brian William Willsey, B.S.

Thesis

Presented to the Faculty of the Graduate School of
The University of Texas at Austin
in Partial Fulfillment
of the Requirements
for the Degree of

Master of Science in Engineering

The University of Texas at Austin
August 2011

Dedication

To my family and friends, who have always helped to support me and without whom I would not have made it this far.

Acknowledgements

Throughout my two years in the Department of Chemical Engineering, I have cherished the opportunity to further my skills academically as a functioning unit of a research team. I have been fortunate in learning a great deal through my studies and have come to appreciate the dynamics of working in a group of intelligent, motivated individuals with extensive knowledge of their fields. I extend my greatest thanks to those who have aided me in my endeavors to further my professional growth. My advisor, Keith P. Johnston, for the great deal of time he spent working with me toward the goal of self improvement, and helping to prepare me for my career after UT. Also, my collaborators in Marc Feldman and Thomas Milner with whom I learned a great deal in the art of working in a diverse group, and who encouraged me to be confident as a valued constituent of our team. My success is largely thanks to Ameya Borwankar and Leo Li Ma, with whom I spent many enjoyable hours planning, implementing, and analyzing experiments, as well as discussing the science behind our results. I would like to thank April Twu, Tianyi Wang, Veronika Sapozhnikova, Jake Mancuso, Travis Jenkins, Justina Tam, and Jennifer Phipps for their help in pursuing the goals of my research. Finally, I would like to thank my lab mates, who have always been there for support and a supply of new ideas: Avi Murthy, Ki Youl Yoon, Dan Slanac, Andrea Miller, Yunshen Chen, Aileen Dinin, William Hardin, Bobby Stover, and Andrew Worthen. I wish them all the greatest success in the future.

Abstract

Reaction Controlled Kinetic Assembly of Small Gold Nanoclusters with High NIR Extinction

Brian William Willsey, MSE
The University of Texas at Austin, 2011

Supervisor: Keith P. Johnston

Nanoclusters with sizes of ~50nm with high NIR extinction at wavelengths beyond 800 nm are of interest in various fields including biomedical optical imaging, microelectronics, plasmonic sensors, and catalysis. Herein we report gold nanoclusters with hydrodynamic diameters of ~50 nm composed of ~10 nm primary particles. The kinetically controlled assembly of clusters occurs simultaneously with the reaction to synthesize the primary particles. The clustering is induced by attractive van der Waals forces that dominate over the steric and electrostatic repulsive forces present. Stability is provided using a single, biocompatible polysaccharide in either carboxymethyl dextran or dextran. High NIR shifts of the surface Plasmon resonance are achieved through close interparticle spacings of primary particles, deviations in morphology from that of a sphere of primaries, and the surface roughness that results from the clustering process. The cluster size is mediated by controlling the relative nucleation and growth rates of

primary particles using a moderate reducing agent in NH2OH and glucose at pH 8.7. It will be shown that cluster size is also dependent on Au concentrations in solution. Maintaining low Au concentrations will allow for smaller clusters. In particular, the small size and high NIR extinction at longer wavelengths (800-1100 nm) makes these particles of interest for optical imaging applications in biology, as particles with a hydrodynamic diameter of ~50 nm have long blood lifetimes.

Table of Contents

List of Tables

List of Figures

List of Illustrations

Chapter 1: Introduction

Gold plasmonic nanoparticles have applications that involve their unique optical and surface properties in such areas as nanomedicine[1,2], catalysis[3], and plasmonic sensors[4,5]. Of particular interest are particles for biomedical applications. Nanoparticles for injection should have a size between 10 and 100 nm in order to optimize blood lifetime.[6-10] Gold nanoparticles exhibit a surface Plasmon resonance as a result of collective oscillations of surface electrons.[2] This Plasmon resonance exhibits a shift toward the NIR region as a result of morphologies that are asymmetric (vary from that of a sphere) as well as close spacings between individual gold nanoparticles.[2,11,12] For tissue applications, SPR that is shifted in the NIR region is desired as water and bodily tissues absorb minimally in this region. Difficulty incorporating highly asymmetric domains required for strong NIR shifts into particles <100 nm challenging.[11]

Nanoclusters presented in Chapter 2 have a hydrodynamic diameter of ~50 nm and strong extinction coefficients in the NIR at wavelengths between 800-1100 nm. Clusters are formed from growing primary particles in solution that are ~10 nm. The colloidal forces between primary particles are tuned such that cluster growth results in particles with controlled size. A polymer stabilizer in carboxymethyl dextran or dextran is utilized to prevent cluster to cluster aggregation. Controlling the nucleation and growth rates of the primary particles governs the size and number of primary particles synthesized. This will affect the attractive forces between particles, allowing control of particle size. As a result of their small size and high optical functionality, the nanoclusters presented are of interest for optical imaging applications such as two photon imaging[13-16], confocal microscopy[17], and optical coherence tomography[18,19].

The data presented in Appendix A has been previously presented in the doctoral dissertation of Ma, L.[20] In this study, the uptake of gold coated iron oxide nanoclusters, termed nanorose[2], into cells was studied. A novel conjugation technique allowed covalent binding of anti-epidermal growth factor receptor (EGFR) monoclonal antibody clone 225 to the surface of nanorose allowed specific uptake into cancer cells overexpressing EGFR. The author of this thesis was highly involved in planning, implementing, and analyzing experiments utilizing Alexa Fluor 488 dye to label antibodies to be conjugated. Measures taken included calculating the number of antibodies require for complete monolayer coverage and comparing these calculations to experiments. Also, the author was engaged in the incubating and imaging of cells with varying levels of fluorescently labeled antibodies on nanoparticles.

Appendix B also presents data presented in Chapter 3 of the doctoral dissertation presented by Ma, L. A mechanism for thin autocatalytic growth on nanoparticle substrates (TAGS) is presented for gold reduced onto the surface of 42 nm iron oxide clusters. This Au shells are avoided by utilizing low Au monomer concentrations in order to prevent excessive autocatalytic growth. Resulting nanoparticles had hydrodynamic diameters less than 60 nm and high optical functionality with SPR spectra shifted toward the NIR. Also, the iron oxide clusters provided magnetic functionality displaying superparamagnetic character and a saturation magnetization of ~65emu/g Fe. The author of this thesis conducted and analyzed experiments investigating the nucleation and growth rate kinetics of Figure B.3. Also, this author was instrumental in synthesizing and observing the morphological and spectral differences resulting from different number of injections (1 vs 3 vs 5 iterations) as shown in Figure B.4 and B.5. For both studies presented in Appendix A and Appendix B, a vital role to conducting, characterizing, and analyzing experiments was played by the author of this paper, though it should benoted the primary author of these sections was Li Leo Ma, PhD.

1.1 REFERENCES

(1) Hirsch, L. R.; Stafford, R. J.; Bankson, J. A.; Sershen, S. R.; Rivera, B.; Price, R. E.; Hazle, J. D.; Halas, N. J.; West, J. L. *Proc. Nat. Acad. Sci.* **2003**, *100*, 13549.

(2) Ma, L. L.; Feldman, M. D.; Tam, J. M.; Paranjape, A. S.; Cheruku, K. K.; Larson, T. A.; Tam, J. O.; Ingram, D. R.; Paramita, V.; Villard, J. W.; Jenkins, J. T.; Wang, T.; Clarke, G. D.; Asmis, R.; Sokolov, K.; Chandrasekar, B.; Milner, T. E.; Johnston, K. P. *Acs Nano* **2009**, *3*, 2686.

(3) Zhang, J.; Sasaki, K.; Sutter, E.; Adzic, R. R. *Science* **2007**, *315*, 220.

(4) Anker, J. N.; Hall, W. P.; Lyandres, O.; Shah, N. C.; Zhao, J.; Van Duyne, R. P. *Nat. Mater.* **2008**, *7*, 442.

(5) Stewart, M. E.; Anderton, C. R.; Thompson, L. B.; Maria, J.; Gray, S. K.; Rogers, J. A.; Nuzzo, R. G. *Chem. Rev.* **2008**, *108*, 494.

(6) Arruebo, M.; Fernandez-Pacheco, R.; Ibarra, M. R.; Santamaria, J. *Nano Today* **2007**, *2*, 22.

(7) Betancourt, T.; Brown, B.; Brannon-Peppas, L. *Nanomedicine* **2007**, *2*, 219.

(8) Boal, A. K.; Ilhan, F.; DeRouchey, J. E.; Thurn-Albrecht, T.; Russell, T. P.; Rotello, V. M. *Nature* **2000**, *404*, 746.

(9) Davis, M. E.; Chen, Z.; Shin, D. M. *Nat. Rev. Drug Discov.* **2008**, *7*, 771.

(10) Kooi, M. E.; Cappendijk, V. C.; Cleutjens, K.; Kessels, A. G. H.; Kitslaar, P.; Borgers, M.; Frederik, P. M.; Daemen, M.; van Engelshoven, J. M. A. *Circulation* **2003**, *107*, 2453.

(11) Tam, J. M.; Murthy, A. K.; Ingram, D. R.; Nguyen, R.; Sokolov, K. V.; Johnston, K. P. *Langmuir* **2010**, *26*, 8988.

(12) Tam, J. M.; Tam, J. O.; Murthy, A.; Ingram, D. R.; Ma, L. L.; Travis, K.; Johnston, K. P.; Sokolov, K. V. *Acs Nano* **2010**, *4*, 2178.

(13) Douma, K.; Prinzen, L.; Slaaf, D. W.; Reutelingsperger, C. P. M.; Biessen, E. A. L.; Hackeng, T. M.; Post, M. J.; van Zandvoort, M. *Small* **2009**, *5*, 544.

(14) Durr, N. J.; Larson, T.; Smith, D. K.; Korgel, B. A.; Sokolov, K.; Ben-Yakar, A. *Nano Letters* **2007**, *7*, 941.

(15) Jiang, Y. Q.; Horimoto, N. N.; Imura, K.; Okamoto, H.; Matsui, K.; Shigemoto, R. *Adv Mater* **2009**, *21*, 2309.

(16) Zhu, J.; Yong, K. T.; Roy, I.; Hu, R.; Ding, H.; Zhao, L. L.; Swihart, M. T.; He, G. S.; Cui, Y. P.; Prasad, P. N. *Nanotechnology* **2010**, *21*.

(17) Qiu, L.; Larson, T. A.; Smith, D. K.; Vitkin, E.; Zhang, S. H.; Modell, M. D.; Itzkan, I.; Hanlon, E. B.; Korgel, B. A.; Sokolov, K. V.; Perelman, L. T. *Ieee Journal of Selected Topics in Quantum Electronics* **2007**, *13*, 1730.

(18) Adler, D. C.; Huang, S. W.; Huber, R.; Fujimoto, J. G. *Optics Express* **2008**, *16*, 4376.

(19) Skrabalak, S. E.; Chen, J.; Au, L.; Lu, X.; Li, X.; Xia, Y. *Adv Mater* **2007**, *19*, 3177.

(20) Ma, L., University of Texas at Austin, 2010.

Chapter 2: Reaction Controlled Kinetic Assembly of Small Gold Nanoclusters with High NIR Extinction

2.1 INTRODUCTION

Gold nanoclusters with controlled optical and surface properties are of interest for applications in areas such as nanomedicine[1,2], catalysis[3], and plasmonic sensors[4,5]. Gold nanoclusters with high extinction cross sections in the near infrared (NIR) region are of interest as optical imaging agents in biomedical applications, as water, soft tissues, and blood absorb minimally in this region. Long blood residence times, necessary for the accumulation of nanoparticles in targeted sites such as atherosclerotic plaques or cancerous tumors, can be achieved for particle sizes between 6 and 100nm, and especially 30 to 60 nm.[6,7,9,10,21,22] To incorporate high levels of functionality into clusters with sizes smaller than 100nm, robust synthesic strategies are needed.

The surface plasmon resonance (SPR) of Au nanoparticles, due to collective oscillations of free electrons, is strongly dependent upon the nanoparticle geometry and environment surrounding the particle. It has a maximum at ~530 nm for spherical geometry.[23] The SPR undergoes a red shift into the NIR region for a variety of asymmetric shapes (deviations from spherical morphology) whereby higher order dipole, quadrupole, and other plasmon modes introduce hybridization.[2,24-27] For nanorods, the red shift increases with aspect ratio,[14,16,17,28,29] with shell geometry for nanoshells[1,18,30] and similarly for nanocages[19]. Particles with high aspect ratio features on the surface, such as points in the case of nanostars, also absorb in the NIR.[31-42] Nanostars are typically grown from pre-existing Au seeds ranging in size from 2 to 50 nm. The selective adsorption of a variety of ligands on particular facets directs growth on the seeds to produce branched nanoparticles,[31,33,42] nanostars,[32,37,39] urchin-shaped particles,[34] and nanoflowers.[40]

Morphologies range from nanoflowers with spherical protrusions[40] to nanostars that have cone-shaped extensions with base to length aspect ratios greater than 1.[37] In each of these cases, protrusions extend from a central core. The core contributes to the total size of the particle, along with relatively long points, such that the total size is greater than 60nm,[33,37,41,42] except for specific cases.[31,34,36,40] Furthermore, the core is relatively symmetric and thus contributes relatively little to the NIR absorbance.

An alternative method to achieve NIR absorbance is to produce asymmetry by forming clusters of closely spaced Au nanoparticles. The spacing between the clusters may be tuned with ligands on the particles surface.[8,11,12,43-46] The mechanisms of particle growth are quite different for nanoclusters relative to single particle entities such as nanorods, nanostars, nanoshells, and nanocages. Polymer templates have been used to direct the assembly of pre-synthesized gold nanoparticles[8,46] or growing nanoparticles[34,37] into clusters. The formation of clusters is aided by strong interactions between the nanoparticles and templating polymers.

Clusters of Au nanoparticles may also be formed without polymer templates via attractive interparticle interactions to raise the Au to polymer ratio, and thus the NIR active content. Several hundred nanometer clusters of citrate capped gold nanoparticles have been grown physically through screening of the electrostatic repulsion between particles by variation of pH or ionic strength of the solution.[47,48] More recently, biodegradable Au nanoclusters ranging from 30 to 100nm have been formed by kinetically controlled colloidal assembly of ~5nm charged citrate coated Au nanospheres with weakly adsorbing polymers. The size is controlled by balancing of Van der Waals, electrostatic, steric, and depletion interactions with small amounts of polymers including a PLA(2K)-b-PEG(10K)-b-PLA(2K) triblock copolymer or PEG (MW = 3350) for a total organic loading of ~20%.[11,12] These clusters of nanoparticles differ from ultrasmall clusters of <100 gold atoms.[49,50]

Current gold nanoparticles that achieve high NIR extinction even from 1000 to 1100 nm typically have sizes around 100 nm[37,42] or larger[33,41] as observed for nanostars or Au nanoclusters larger than ~400 nm.[47] For nanoflowers around 50nm, the extinction is low at 800nm.[31,34,36,40] For nanoparticles 50 nm or smaller, it is challenging to introduce sufficient asymmetry in structure to produce high extinction coefficients in the 800-1100nm range.[11] For 35 nm Au/iron oxide nanoclusters of closely spaced primary particles with asymmetry in the shapes of the Au domains produces a maximum extinction at 750 nm and a ratio in the extinction coefficients at 1000 relative to 750 nm of 0.61.[2] These nanoclusters were formed by reducing $HAuCl_4$ in the presence of iron oxide nanoclusters and a polymeric stabilizer, dextran. Additionally, ~30nm nanoclusters of kinetically assembled ~5nm primary gold particles have exhibited broad extinction spectra measured up to 900nm.[11] Hollow morphologies, such as nanocages with ~45nm edge lengths exhibit extinction peaks around 840nm.[19] To our knowledge, none of the nanoparticles above reported on the order of 50 nm or smaller exhibited strong NIR absorbance at 1000 to 1100 nm, and relatively few even at 800 nm.[25,28,30,34] Furthermore, it would be desirable to simplify the Au/iron oxide nanoclusters[2] to form particles without any iron oxide.

Herein, we introduce a Au nanoparticle on the order of 50 nm with strong absorbance in the NIR even up to 1100 nm. Primary Au nanoparticles are synthesized directly from $HAuCl_4$ by homogeneous nucleation and growth in the presence of a polymer stabilizer, either dextran or carboxymethyl dextran. The precursor concentration and polymer/Au ratio are adjusted to prevent excessive autocatalytic growth to produce particles on the order of 10 to 15 nm. Furthermore, we attempt to balance the primary particle concentration and size such that they assemble to form Au nanoclusters of controlled size. For a particle size on the order of 10 nm, van der Waals attraction will be shown to favor kinetic assembly into a cluster. The weakly adsorbing polymer on the nanocluster surface can provide steric and electrostatic (for CMD) stabilization between individual clusters. Finally, the Au precursor is added in single or multiple iterations to provide additional control over the nucleation and growth of primary particles, and the addition of primary particles to pre-existing clusters. We attempt to optimize the goals of small particle size for bloodstream lifetime and cellular uptake versus an increase in the NIR absorbance with cluster size. The unusually strong red shift to 1100nm is a result of close spacings between the gold domains of primary particle surfaces and some asymmetric growth beyond spherical geometry for the primary particles.

The new Au nanoclusters are shown to offer benefits versus earlier particles. The lack of a solid core, as in the case of nanoflowers and nanostars, is beneficial for keeping the particle size small. Whereas the nanoclusters are synthesized at pH 8.7, we also report nanoflowers at pH 9 and 9.3 to contrast the different synthetic mechanisms and spectral properties. Relative to nanoflowers, the nanoclusters minimizes the symmetric spherical core (visible extinction region) to the SPR from a relatively spherical core. Unlike the case of Au nanoclusters formed by kinetic assembly of citrate/lysine coated Au nanospheres, we do not need to add a ligand such as citrate on the primary particles. Perhaps the lack of this ligand will allow even closer spacings between particles to strengthen the red shift. Stabilization is achieved with a single, biocompatible polysaccharide, either carboxymethyl dextran or dextran, without a secondary ligand. In addition, the nanoclusters are synthesized from precursor in a single step. Finally, they provide even stronger NIR at 1000 nm than in the case of Au/iron oxide nanoclusters, and do not have the complication of the iron oxide component (The magnetic properties of iron oxide are of interest for multimodal imaging).

The dextran coatings interact with dextran receptors on macrophage cells which are present in diseased tissue such as atherosclerotic plaques and provide mechanism for targeting these cells.[2,51] Thus, the optical properties and size of these particles reinforces their potential as contrast agents in biomedical applications such as two photon imaging[13-16], confocal microscopy[17], optical coherence tomography[13,18,19], photothermal therapy[1,2,19,28-30,52], and combined photoacoustic imaging and photothermal therapies[53-55] .

2.2 METHODS

All reagents used were analytical grade. Ammonium hydroxide, hydroxylamine hydrochloride, and dextrose anhydrous were purchased from Fisher Chemicals (Fairlawn, NJ), carboxymethyl dextran sodium salt (MW = 10,000) and dextran (MW = 10,000) from Sigma Aldrich (St. Louis, MO), and tetrachloroauric acid trihydrate from MP Biomedicals LLC. (Solon, Ohio).

2.2.1 Synthesis of Au Clusters - First Iteration

Au nanocluster synthesis followed a modified procedure utilized previously for Au/iron oxide nanoclusters.[2] The primary difference in the new approach was that we did not use iron oxide nanoparticles or iron in any form. For carboxymethyl dextran coated nanoclusters, a 70.4mL aqueous reducing solution was prepared at room temperature with 2.0 mM NH2OH.HCl, 0.3 mM carboxymethyl dextran, and 475mM dextrose. Synthesis of dextran nanoclusters followed the same procedure with the same concentration, 0.3mM dextran. The pH of the solution was adjusted between pH 8.7 or 9.0 using 7% ammonium hydroxide in water. It decreases less than 0.1 unit after addition of the precursor. Under rigorous stirring, a given volume of aqueous Au precursor at a concentration of 12.7mM was rapidly injected into the reducing solution to achieve the desired Au concentration. Reactions began to exhibit an initial blue color at ~2min. At pH 8.7 the color of the solution turned blue. At pH 9.0 or pH 9.3, the solution turned blue and then gradually transitioned to purple and finally pink after ~10 minutes. After ten minutes, nanoclusters were recovered by centrifugation at 6,000 rpm for 7 min. The nanoparticles formed a pellet and the supernatant was then decanted. The nanoparticles were redispersed by bath sonication for ~1min.

2.2.2 Synthesis of Au Clusters – Further Iterations

Additional iterations of precursor at a known concentratin and volume were injected directly into the dipsersions of nanoparticles prepared in the first iteration. After iteration including the first one, ~10 min was allowed for reaction. The color always stabilized during these ten minutes. For each iteration, a given amount of Au precursor solution at 12.7mM Au was injected in order to achieve the desired concentration of Au precursor in solution. Final samples were concentrated by centrifugation at 6,000 rpm for 7 min, after which the supernatant was decanted. The clusters were redispersed into about 0.5 mol of the supernatant that was not removed with ~1min bath sonication to help remove this mixture from the centrifuge tube. Finally, this concentrated dispersion was diuted in DI water at various levels depending upon the characterization procedure.

2.2.3 Materials Characterization

Dynamic light scattering (DLS) measurements were performed in triplicate on a custom-made Brookhaven instruments ZetaPlus apparatus at a scattering angle of 90 and temperature of 25C.[56] Nanoparticle concentrations were adjusted using DI H2O in order to get signal count rates between 150-400 kcps. Prior to DLS measurements, samples were bath sonicated for ~2 minutes. The autocorrelation functions were analyzed with a non-negative least-squared (NNLS) method to determine distributions by volume.

Low resolution TEM (FEI Tecnai Spirit BioTwin) was performed at an 80kV accelerating voltage. A drop of the dispersion of particles before centrifugation was put on a 400 mesh ultrathin carbon-coated copper TEM grid. Excess liquid was blotted with a tissue and the grid was allowed to dry in 30 in Hg vacuum. Next the samples on the grid were further washed using a drop of DI H2O on the grid that was blotted with tissue.

Thermogravimetric analysis was performed using a Perkin-Elmer TGA 7 under a nitrogen atmosphere at a gas flow rate of 20mL/min. Nanoparticle samples for TGA were washed 3 times with DI water using centrifugation at 6,000 rpm for 7 minutes. The recovered samples were dried to a powder in a low pressure environment at 30 in Hg in vacuum. Samples were heated to 100C in the TGA instrument for 20 minutes to remove moisture. The samples were then heated from 100C to 900C at a rate of 15C/min, and then held at 900C for 30 minutes.

Measurements of Au concentrations in solution were obtained by first dissolving the nanoparticles in aqua regia. To a small glass vial, 0.25mL HNO3 was added followed by 0.03mL of sample solution. To this, ~0.75mL of HCl was injected and the samples were allowed to sit overnight (~12hr), during which time the sample solutions changed from blue to clear. Samples were then diluted with DI H2O until Au concentration was between 1 and 5 μg/ml. The concentrations were obtained with a GBC 908AA flame atomic absorption spectrometer (GBC Scientific Equipment Pty Ltd) equipped with an air-acetylene flame furnace. The absorption for Au was recorded at 242.8 nm.

3 RESULTS

2.3.1 Au Nanocluster Formation at pH 8.7

All of the experiments at pH 8.7 will be shown to result in Au nanoclusters of primary particles, with either CMD or dextran as the stabilizer. Low resolution TEM results are shown for nanoclusters made with CMD in Figure 1 for either one or two equal iterations of Au precursor. The nanocluster is an assembly relatively uniform primary nanoparticles on the order of 10 nm, much like previously reported nanoclusters.[2,11,12] To compliment these results for single particles, DLS was utilized to provide an ensemble average of nanoparticle hydrodynamic diameters, D_hs. The D_h, of the nanoclusters synthesized with a single iteration of 0.018mM Au was on the order of ~33 nm as measured by DLS (Figure 2a and Table 1), consistent with the size of the Au domain (polymer not visible by TEM) in the TEM image. Although it is difficult to see through the thick central region of the clusters, primary particles are visible on the outer surface (Figure 1a). After a second iteration of 0.018mM Au, the cluster size increased to ~45 nm as measured by DLS (Figure 2a). For two iteration nanoclusters, the primary particles within the clusters appeared to be more elongated in some cases. Furthermore, the particles on the surface appeared to be more distinct, or equivalently, the surface appeared to be rougher (Figure 1b). The inability to accurately capture individual gold domains is a result of the resolution of the TEM and the inherent high electron density of gold atoms that prevents imaging of domains at these cluster thicknesses. Figure 2b provides the reproducibility in D_h for these 45 nm nanoclusters. The standard deviation in the mean D_h was ~2 nm. Similar reproducibility was observed for the other clusters in this study.

Sample	Final Gold Concentration (mM)	Number of Gold Additions	Hydrodynamic Diameter (nm)	Extinction ratio (800nm/500nm)	Extinction Coefficient (cm2/µg Au)
CMD pH = 8.7	.018	1	33	1.03	
CMD pH = 8.7	.036	2	46	1.46	.027
CMD pH = 8.7	.036	1	67	1.34	
Dextran pH = 8.7	.018	1	39	1.24	
Dextran pH = 8.7	.036	2	49	1.55	.017
Dextran pH = 8.7	.036	1	64	1.41	

Table 1: Summary of nanoclusters coated with CMD and dextran at pH 8.7.

Sample	Final Gold Concentration (mM)	Number of Gold Additions	Hydrodynamic Diameter (nm)	Extinction ratio (800nm/500nm)	Extinction Coefficient (cm2/µg Au)
CMD pH = 9.0	.036	1	35	0.20	
CMD pH = 9.0	.072	2	43	1.05	.003
CMD pH = 9.0	.072	1	47	0.79	
Dextran pH = 9.3	.018	1	19	0.24	
Dextran pH = 9.3	.108	6	45	1.41	.022
Dextran pH = 9.3	.108	1	54	0.98	

Table 2: Summary of nanoflowers coated with CMD at pH 9.0 and dextran at pH 9.3.

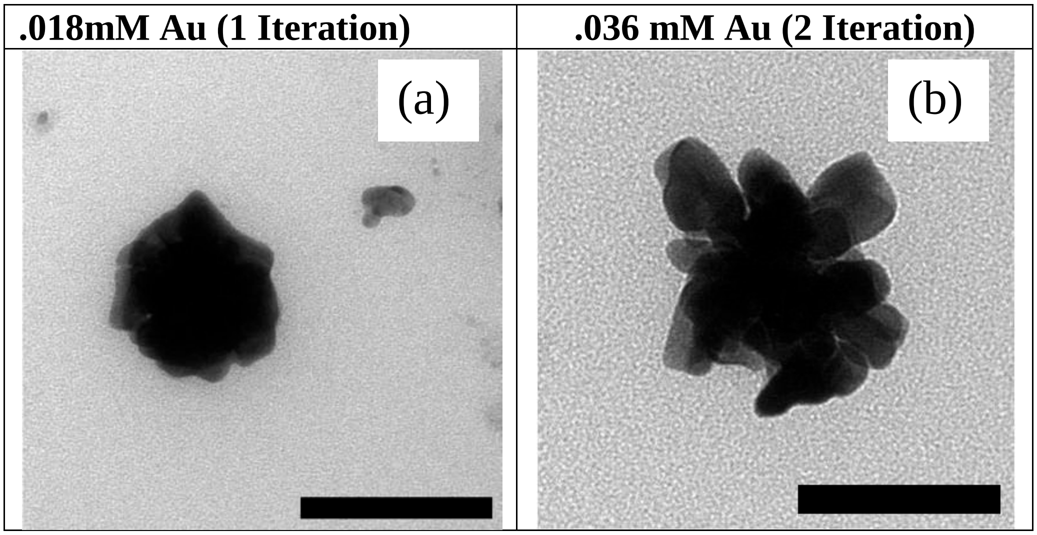

Figure 1: Low resolution TEM of nanoclusters after 1(a) and 2(b) iterations synthesized with CMD at pH=8.7. Scale bar is 50nm

For particles synthesized with a single iteration of two fold larger Au concentration of 0.036 mM, the D_h of the nanoclusters was measured to be ~67 nm(Figure 2a). Here the D_h was twice as large as for the 33 nm particles synthesized with 0.018mM Au. They were also larger than the 45 nm particles synthesized with the same total amount of Au, but in two equal iterations rather than one. Thus, the Au concentration and number of iterations offers a way to tune the particle size.

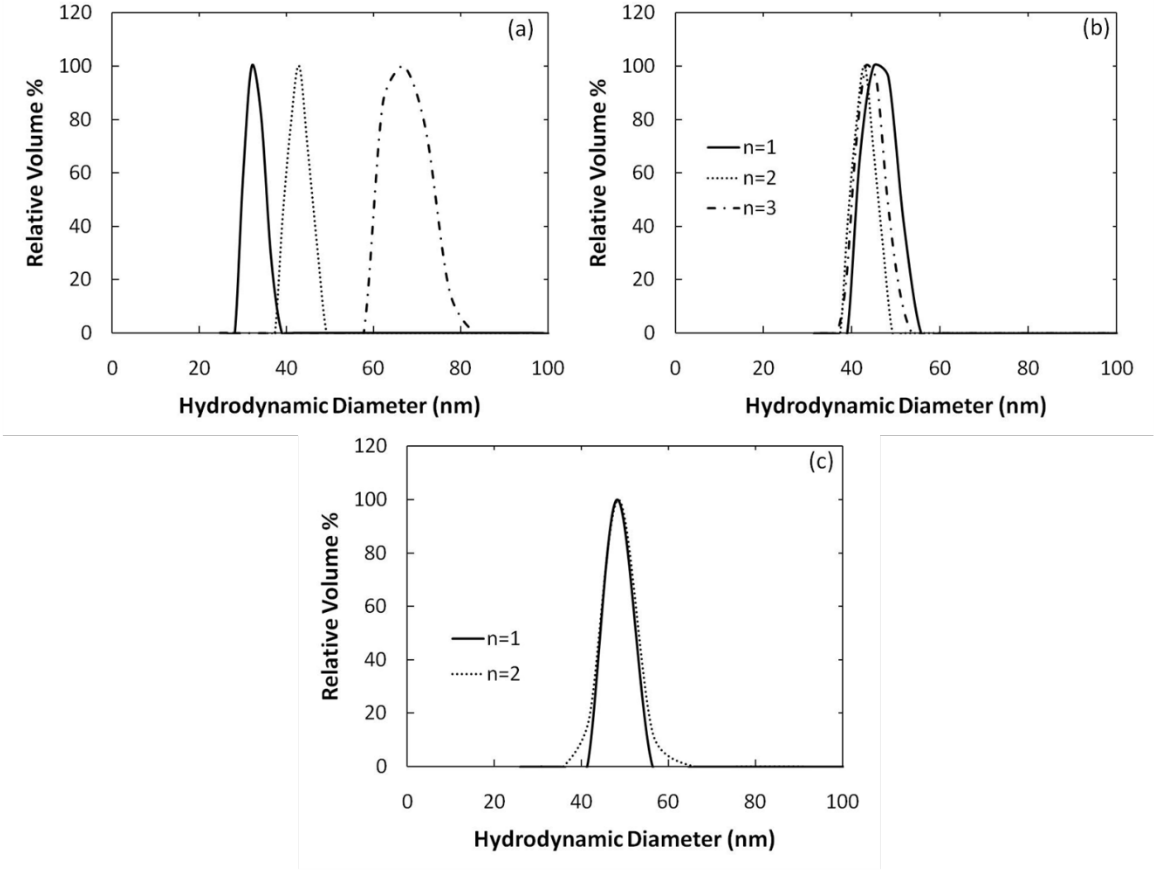

Figure 2: DLS hydrodynamic diameter after 1 and 2 iterations at 0.018 mM Au per iteration, and 1 iteration at 0.036 mM Au with CMD coating at pH=8.7 (a), 2 iterations at 0.018 mM Au per iteration with CMD coating at pH 8.7 again (b), and 2 iterations at 0.018mM Au per iteration with dextran coating at pH 8.7.

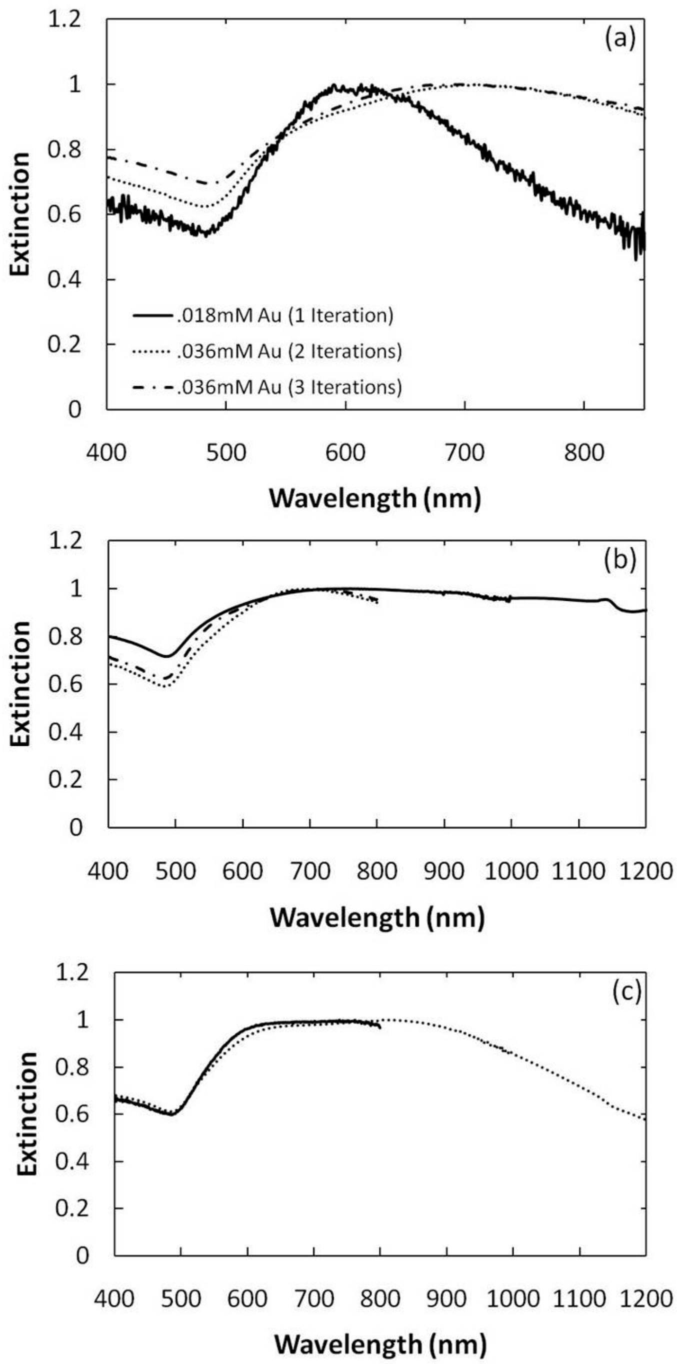

Figure 3: Extinction spectra after 1 and 2 iterations at 0.018 mM Au per iteration, and 1 iteration at 0.036 mM Au with CMD coating at pH=8.7 (a), 2 iterations at 0.018 mM Au per iteration with CMD coating at pH 8.7 again (b), and 2 iterations at 0.018mM Au per iteration with dextran coating at pH 8.7.

Each of the nanoclusters had a significant level of extinction in the NIR as shown in Fig. 3a. We define $A_{800/500}$ as the ratio of absorbance at 800 to 500 nm (Table 1). The spectra are shown on an arbitrary scale with the peak extinction set to unity. The smallest 33 nm particle synthesized with one iteration of 0.018 mM Au exhibited a peak at ~600 nm that gradually decreased to 800 nm (Figure 3a). For the two larger particles, the peak was much broader and red shifted to ~700 nm. A comparison of the extinction ratios $A_{800/500}$ is shown in Table 1. The ratio was largest for the 46 nm clusters made with two iterations, quite large for the 67 nm clusters, and still more than unity for the smallest 33 nm clusters.

For the 45 nm particle, the extinction coefficient was determined at 755 nm, on the basis of a Au concentration of 0.017 $cm^2/\mu g$ Au measured by atomic absorption spectroscopy (Table 1). The reproducibility in the spectra was excellent out to 800 nm (Figure 3b) Finally, the extinction spectra was measured over an extended range all the way to 1200 nm for this 45 nm particle. Remarkably, it did not decrease but remained high and fairly constant. To our knowledge, strong extinction in the near IR over this wavelength range has not been reported previously for any type of sub-50 nm Au particle.

The strong NIR absorbance is a consequence of the particle morphology[2,11,12], in particular the close spacing of primary particles in the nanocluster geometry deviation in the shape of the primary particles from spheres, as was explained in the introduction. If the particles were solid spheres instead of nanoclusters, the NIR spectra would be much weaker as will become evident in other particles presented below.

To understand the role of the polymer structure, the negatively charged carboxymethyl functionalized dextran polymer coating was replaced with a neutral dextran coating at pH 8.7. Nanoclusters synthesized with dextran (n=2) using two injections of Au at 0.018 mM, resulted in nanoclusters with a D_h of ~49 nm and low polydispersity (Figurere 2c). This size was essentially the same as for the same two iteration synthesis performed with CMD. Therefore, the charge on the polymer for the two types of dextran did not influence the D_h.

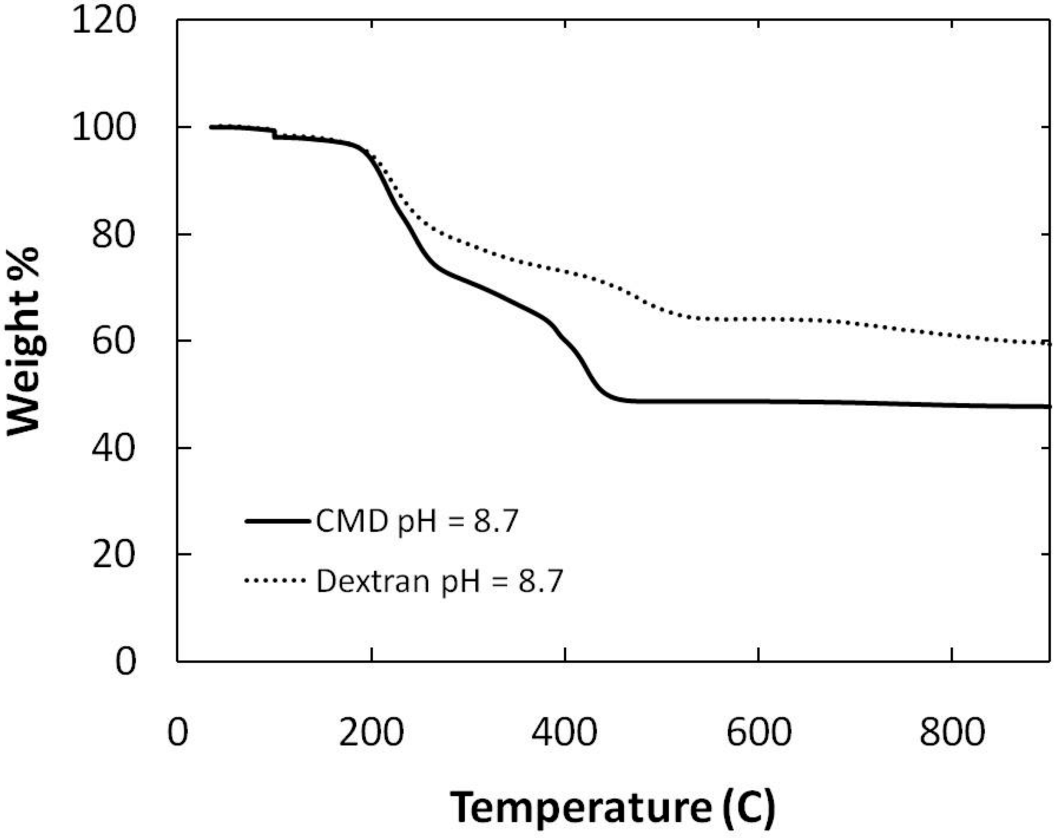

Figure 4: Figure 9: TGA of gold nanoclusters synthesized with 2 iterations at .018 mM Au per iteration with a CMD and a dextran coating at pH 8.7.

In order to determine the degree of polymer on the nanocluster surface, the polymer to gold mass ratios were determined using TGA analysis. The mass percent of polymer on the the CMD coated clusters with two iterations (0.018 mM Au per iteration) at pH 8.7 was 50% (Figure 4). For the dextran coated clusters at pH 8.7 with two iterations (0.018mM Au per iteration) polymer mass percent was measured to be 40% (Figure 4). Thus, similar levels of polymer stabilizers on the surface were experienced for both nanocluster coatings.

2.3.2 Au Nanoflower formation at pH 9.0

In this section, the pH of the reducing solution was adjusted to 9.0 using ammonium hydroxide. These experiments utilized CMD as a polymer stabilizer with either 1 or two iterations of Au precursor. The D_h is shown for either one or two iterations with 0.018 mM Au, the same as for the nanoclusters above formed at the lower pH. Interestingly, the results were very different. The D_h values were much smaller. For the ~20 nm spheres produced with one interation, the spectra was only shifted slightly from that of pure Au spheres.[11,12] After a second iteration the size was still only ~32 nm with a modest red shift (Figure 5). Since the goal of this study was to produce much stronger red shifts, we decided to double the Au precursor concentrations to form larger particles.

For the new choice of a new Au concentration for each iteration of 0.036 nm, low resolution TEM images demonstrate significant morphological differences for one versus two iterations (Figure 6). Relatively low surface roughness is apparent after one iteration. It appeared that the particles were relatively spherical in shape (Figure 6a). This spherical morphology is extremely different than that of the nanoclusters of primary particles in Figure 6 formed at pH 8.7.

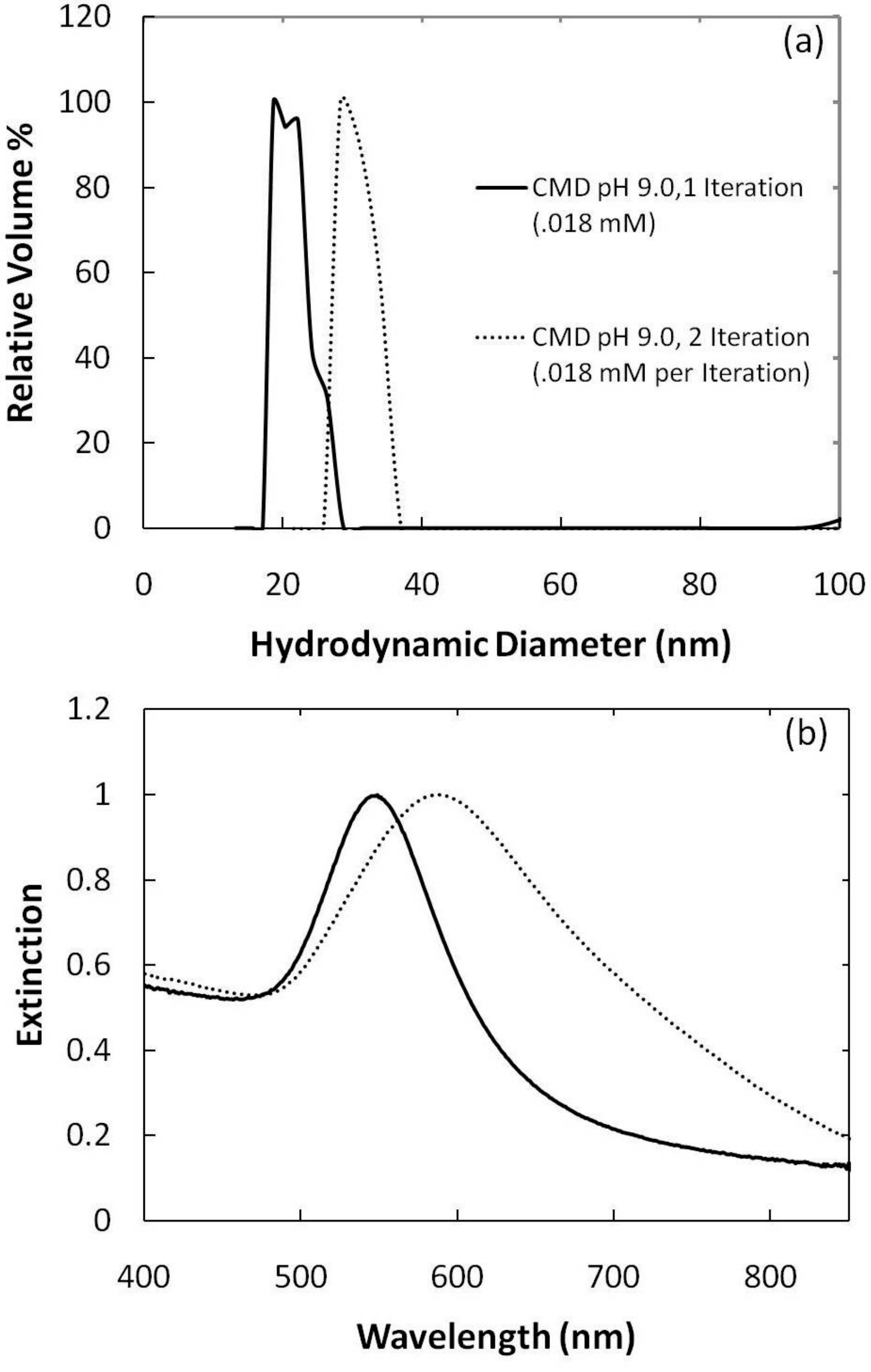

Figure 5: DLS hydrodynamic diameter (a) and UV-Vis Extinction spectra (b) of gold nanoclusters synthesized with 2 iterations at .018 mM per iteration with CMD coating at pH 9.0.

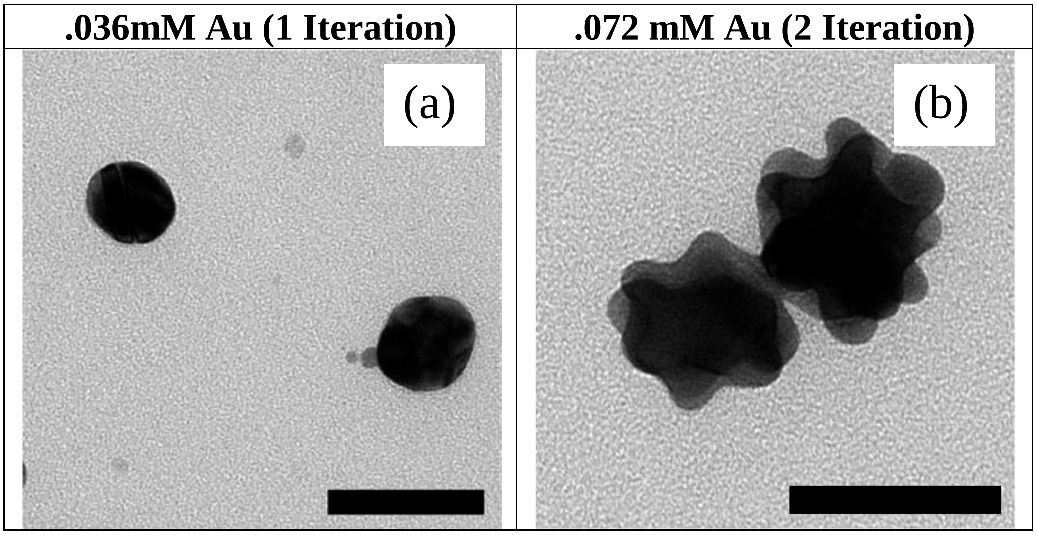

Figure 6: Low resolution TEM of nanoflowers after 1(a) and 2(b) iterations synthesized with CMD at pH=9.0. Scale bar is 50nm.

The surface was much rougher than after one iteration as shown by TEM. Given that these particles were composed from relatively spherical particles after one interaction, it is likely the central regions remained as nearly spherical cores. It is difficult to observe the outline of this denser core region by low resolution TEM given the thickness of the particles, which is manifested as a dark solid mass in the center. Primary small nanoparticles are evident on the surface of these particles. Thus these particles will be called nanoflowers to suggest petals on the outside of a core, as done previously.[35,36,38,40]

The DLS results were consistent with TEM. Nanoparticles synthesized with a single iteration of 0.036 mM Au exhibited a D_h of ~35nm (Figure 7a), much larger than for a concentration of only 0.018 mM in Figure 5a. After a second iteration of Au at 0.036 mM, the size of the nanoparticles increased to ~43 nm (Figure 7a).

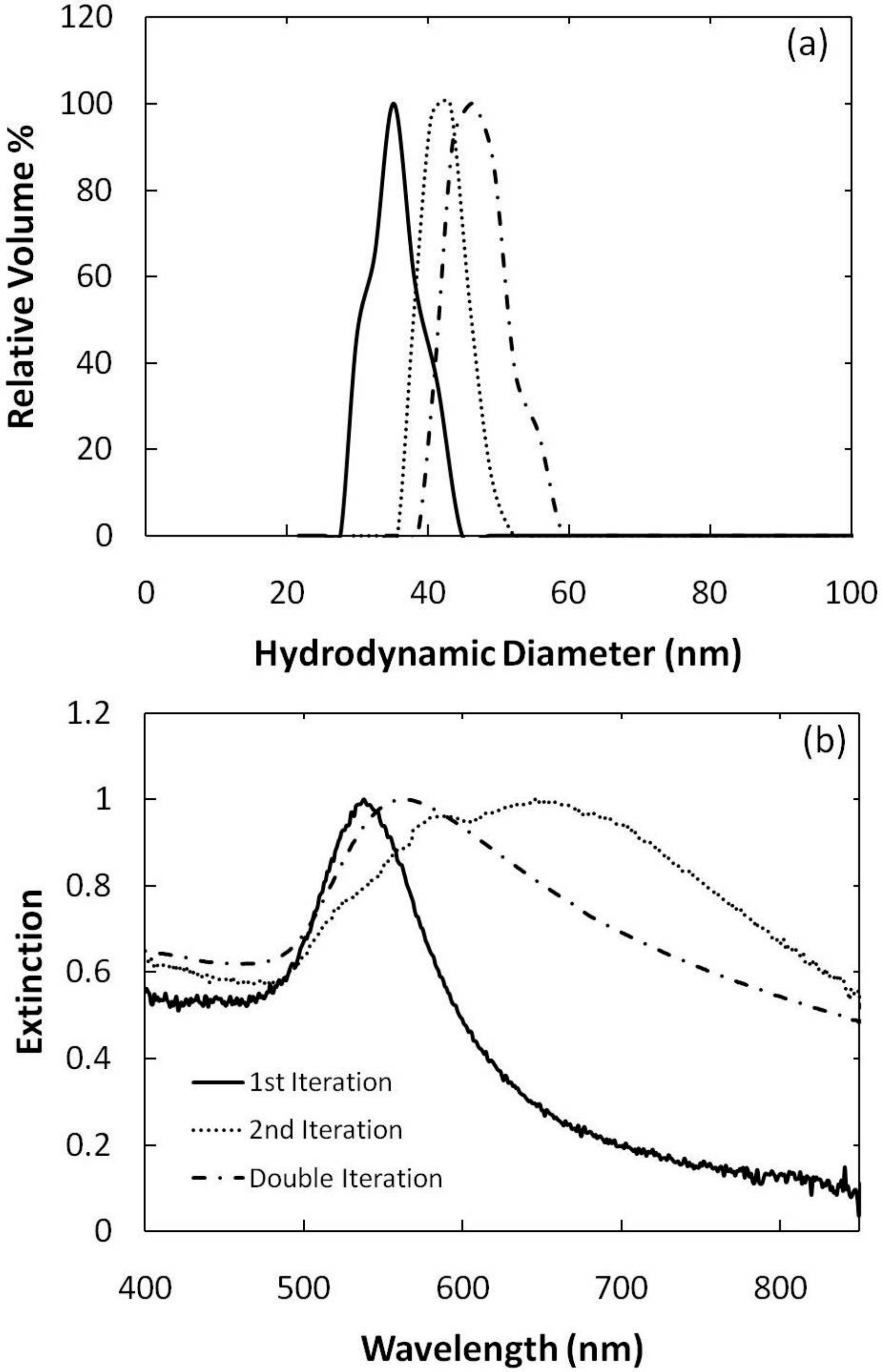

Figure 7: DLS hydrodynamic diameter (a) and UV-Vis extinction spectra (b) of nanoflowers after 1 and 2 iterations at .036 mM Au per iteration, and 1 iteration at .072 mM Au with CMD coating at pH=9.0.

A single injection of Au at a two fold higher concentration of 0.072 mM Au resulted in nanoflowers with a D_h of ~47 nm by DLS (Figure 7a). These particles are larger than the 43 nm particles formed with two equal iterations of Au for a total of 0.072 mM. Thus, this trend of larger particle for a single injection versus two injections at a constant overall amount of Au is consistent with the behavior seen in Figure 2a at the lower pH of 8.7.

Nanoparticles synthesized with one injection of Au monomer at 0.036 mM Au exhibited a sharp extinction peak at ~540 nm with cross sections dropping dramatically at 800 nm (Figure 7b with an $A_{800/500}$ of only 0.20. This spectra was red-shifted only modestly from the known behavior for spherical Au particles. For the two larger particles, the shift was larger for the 43 nm particles produced with two iterations than the larger 47 nm particle produced with a single one. Thus the order in the red shifts was the same as at pH 8.7 for the nanoclusters. However, for the nanoflowers, the peaks were not nearly as broad and the extinction spectra was not as strong wavelengths from 600 to 1200 nm.(Figure S1) as for the nanoclusters in Figure 3. However, the high extinction even at 900 to 1000 nm is still quite rare for such a small particle, if not unprecedented.

The weaker red shift for the nanoflowers in Figure 5 versus nanoclusters in Figure 3 suggests a relatively solid spherical core part is present for the nanoflowers and not for the nanoclusters. Thus, the NIR spectra support our morphological TEM analysis of Au nanoparticle petals on a relatively solid spherical Au core. For the nanoflowers, as seen at pH 8.7 the concentration of Au and number of iterations may be used to tune both the morphology and the spectra of the particles.

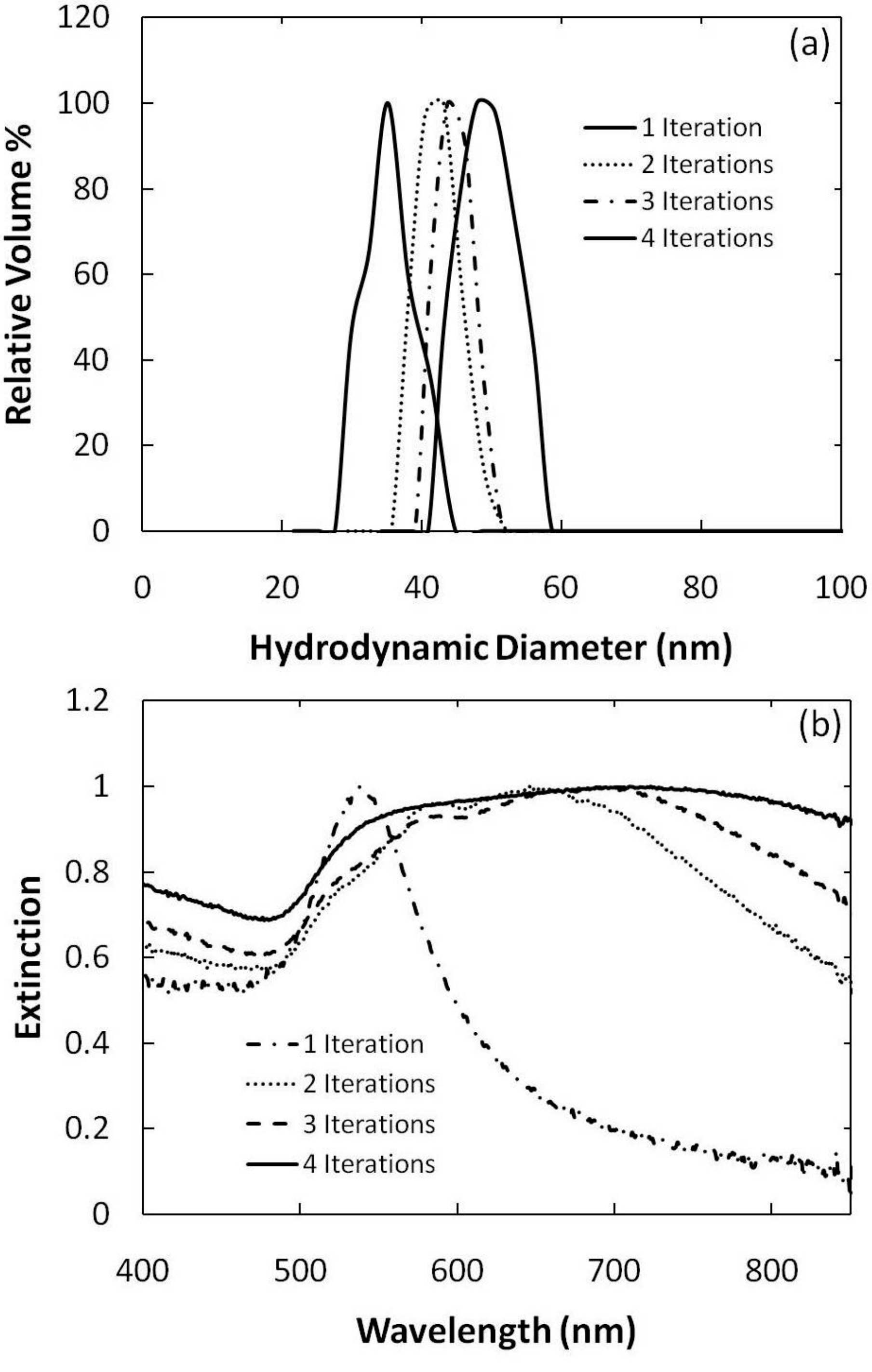

Figure 8: DLS hydrodynamic diameter (a) and UV-Vis extinction spectra (b) of nanoflowers after 1-4 iterations at .036 mM Au per iteration with CMD coating at pH=9.0.

2.3.3 More than two Au Iterations for Nanoflowers at pH 9.0 and 9.3

Given the larger red shifts for two iteractions versus one, we took this concept further to explore even larger numbers of iterations with CMD as a surface coating at pH 9.0 and 9.3. The number of iteration, each at 0.036 mM, ranges from one to four in Figure 8. The first two iterations were already shown in Figures 7. With a third and fourth iteration, D_h increased monotonically. After the fourth iteration, with a total Au concentration of 0.144 mM, the nanoflower D_h reached ~55nm (Figure 8a). Thus, each successive increase in D_h with iteration decreases, and the D_h approached a plateau.

The trends in the extinction spectra may be seen to be consistent with the D_h change. Again, the first two iterations were already shown in Figure 7. The third and fourth iterations increased the extinction significantly at 800 nm, continuing the trend seen after the second iteration (Figure 8b).

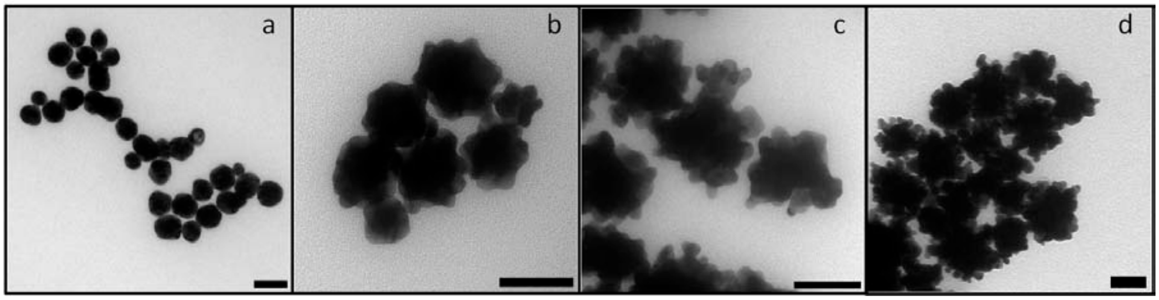

Figure 9: Low resolution TEM of nanoflowers after 1(a), 3(b), 7(c), and 10(d) iterations synthesized with dextran (3mM) at pH=9.3. Scale bar is 50nm.

An even more detailed study was done for a total of 12 iterations, this time at a slightly higher pH of 9.3. Here the stabilizer was dextran with a higher concentration of 3 mM. The concentration was increased to stabilize the higher total Au surface area for the larger nanoflowers with large numbers of iterations. For this homologous series, each iteration introduced 0.018 mM Au into the reaction mixture. The morphological changes associated with the increasing number of Au iterations are demonstrated in the low resolution TEM images of Figure 9. After one iteration, the nanoparticles are spherical in shape with a relatively smooth surface boundary as seen at for the similar experiment in Figure 6. Here the D_h was only ~18 nm as measured by DLS (Figure 10a), suggesting greater passivation of growth with the higher polymer concentration and low concentration of Au. The nanoflower D_h increased monotonically with the number of iterations injected (Figure 10a) with fairly linear behavior, consistent with TEM. For the last few iterations, the polydispersity in D_h increased significantly. This increase in size is accompanied by the appearance of increased roughness on the surface of the nanoflowers, as observed for 1, 3, 7, and 10 iterations through low resolution TEM (Figure 9). The proximity of the nanoclusters to each other was an artifact of the TEM sample preparation, used to collect multiple particles. Primary particles become more apparent on the particle surface with an increase in the number of iterations. Furthermore, deviations of these primary particle from purely spherical shape, for example elongated shapes (early stages of transitions to rod-like morphology) became more apparent(Figure 9c versus 9b). The final D_h observed after 12 iterations of Au was measured to be ~63 nm (Figure 10a). Thus, in a similar manner to the experiments with CMD at pH 9.0, multiple iterations of Au result in the monotonic increase in the D_h of the nanoflowers. This increase in D_h is accompanied by increased roughness on the nanoflower surface.

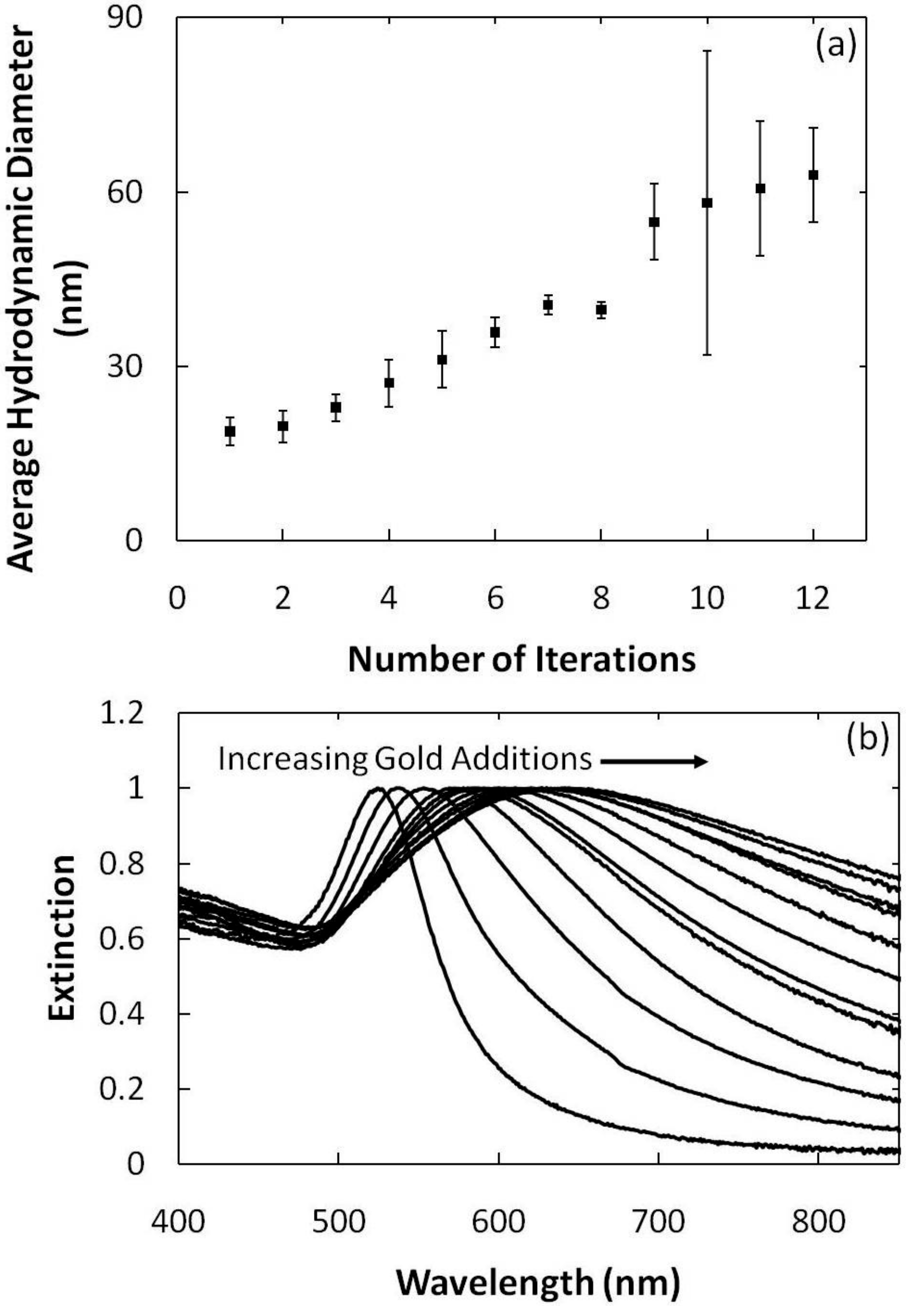

Figure 10: DLS hydrodynamic diameter (a) and UV-Vis extinction spectra (b) of nanoflowers after 1-12 iterations at .018 mM Au per iteration with dexran coating at pH=9.3.

The extinction spectra was measured between 400 and 800 nm for each iteration, again at pH 9.3 with dextran as the stabilizer (Figure 10b). The initial iteration produced a spectra with a maximum at ~530 nm indicative of a spherical particle consistent with TEM. After a second iteration, the extinction peak shifts to ~540 nm with slightly higher $A_{800/500}$. With each new iteration, the extinction spectra shifts to the red, the peak continues to broaden, with the associated increase in $A_{800/500}$. After 12 iterations of Au for a total concentration of 0.216 mM Au, the extinction peak has shifted to ~650 nm with an $A_{800/500}$ of 1.25

The reproducibility of nanoflowers synthesized with CMD at pH 9.0 and dextran nanoflowers at pH 9.3 is shown in Figure 11. For CMD coated nanoflowers synthesized at pH 9.0 with two iterations of 0.036mM Au, the D_h was 43nm with a standard deviation of 2 nm. Dextran nanoflowers synthesized with 6 iterations at a concentration of 0.018mM per iteration and a pH of 9.3 had an average D_h of 45nm with a standard deviation of 2nm by DLS. Furthermore, the extinction spectra peaks were around 620 nm with cross sections decreasing as wavelengths increased to 800nm. A summary of these nanoflowers comparing them to nanoclusters are included in Table 1 and Table 2.

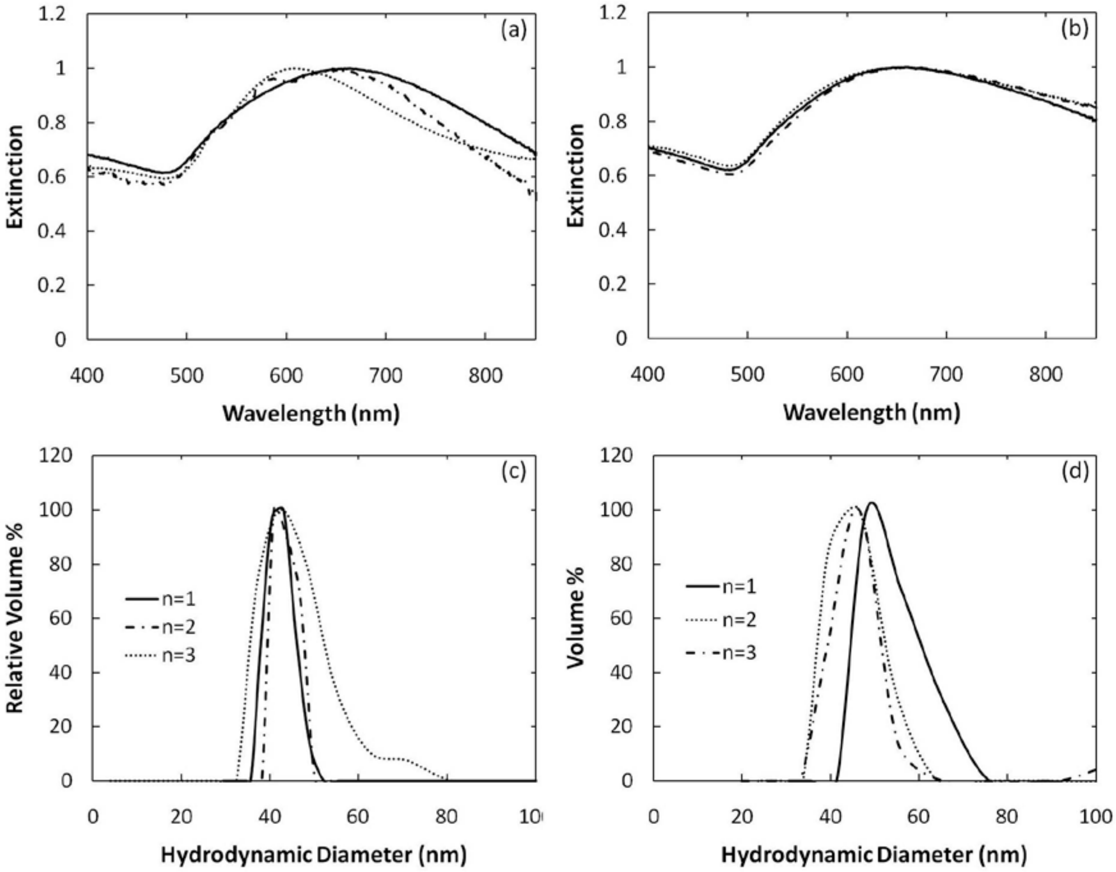

Figure 11: DLS hydrodynamic diameter (a) and UV-Vis Extinction spectra (b) of gold nanoflowers synthesized for the conditions in Figure 6. DLS hydrodynamic diameter (c) and UV-Vis Extinction spectra (d) of gold nanoflowers synthesized with 6 iterations at .018 mM Au per iteration with dextran coating at pH 9.3.

4 DISCUSSION

2.4.1 Control of Primary Particle Size

Herein, we present a mechanism to synthesize gold nanoclusters as a result of the aggregation of primary gold particles into nanoclusters as seen in Scheme 1. Control over the nucleation and growth of primary particles, as represented in the first and second diagrams in the top panel of Scheme 1, determines the size and number of building blocks to be used in synthesizing clusters. Furthermore, control over cluster sizes is dependent on the size and number of primary particles per cluster as shown in the third diagram in the top panel of Scheme 1. As will be discussed in the next section, initiation of aggregation of primary particles requires sufficiently sized particles that attractive forces will overcome repulsive forces.

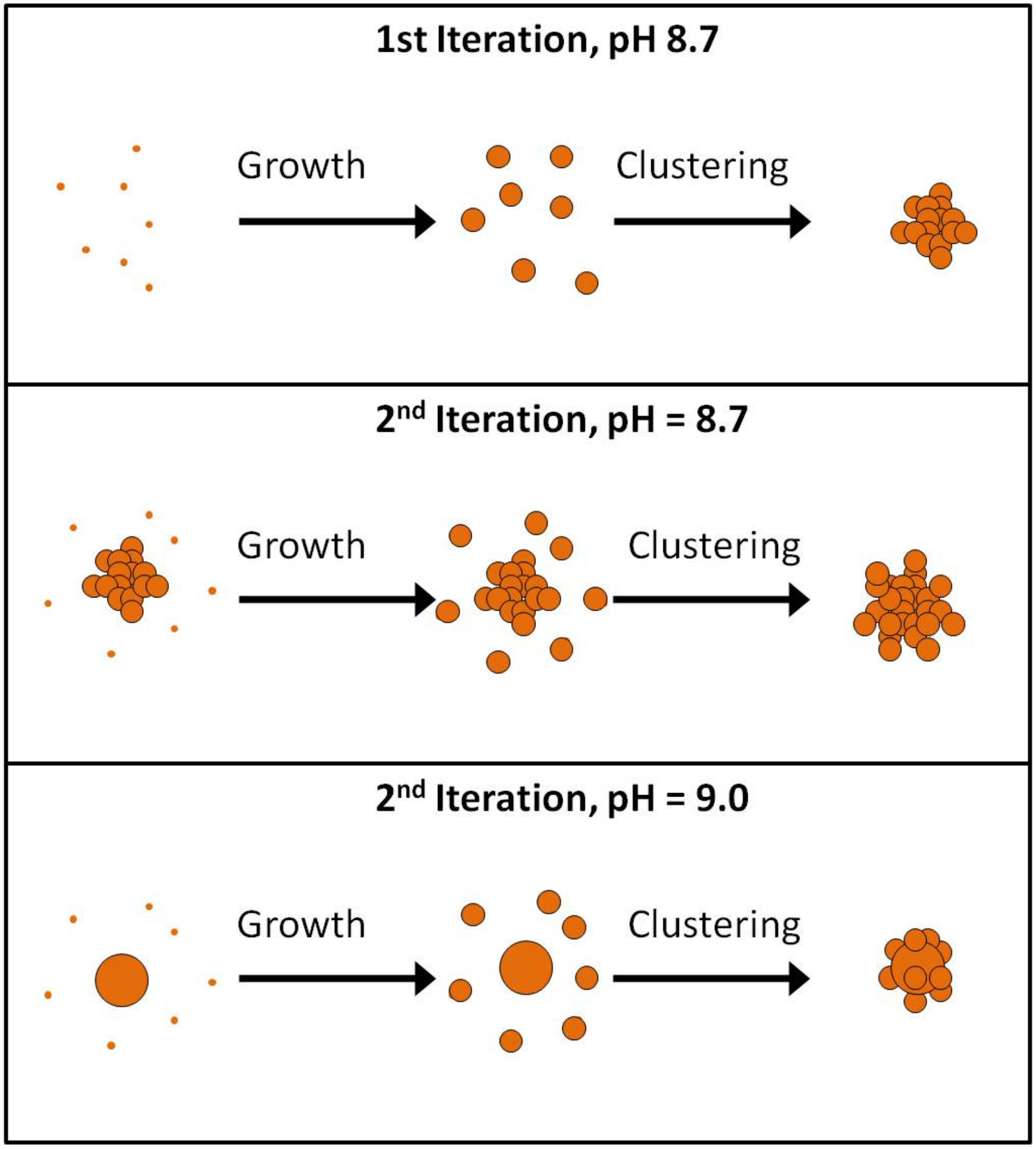

Scheme 1: Diagram of growth mechanism for the 1st and 2nd iterations of Au in the case of nanoclusters and for the 2nd iteration in the case of nanoflowers.

A mechanism of homogenous nucleation to produce Au particles followed by autocatalytic growth on the particles has been widely used to synthesize nanoparticles of controlled size with narrow polydispersity.[57,58] Homogenous nucleation to form Au particles can be expressed as

$$nAu^{3+} \xrightarrow{k_1} nAu^0 \; (nucleation) \qquad (1)$$

The nucleation rate can also be represented through crystallization and reaction kinetics as –

$$\rho(t) = 4\pi a n_c^{1/3} D c^2 e^{-\Delta G_c/kT} \qquad (2)$$

Growth on the Au nuclei formed in the previous step is given as

$$nAu^{3+} + nAu^0 \xrightarrow{k_2} 2nAu^0 \; (growth) \qquad (3)$$

where n is chosen arbitrarily to represent the number of gold atoms in one gold nuclei, k_1 and k_2 represent rate constants for nucleation and growth, respectively, $[Au^{3+}]_0$ is the initial concentration of precursor, and Au^0 is gold that has been reduced from solution.[59,60] The expression for growth presented in Eq. 2 has reduced Au as a reactant, and thus this growth is considered autocatalytic by definition. Autocatalytic growth as a mechanism for Au reduction is in agreement with previously synthesized particles.[57,61]

The relative rates of nucleation (Eq. 1) and growth (Eq. 3) determine the primary particle size. As the k1/k2 ratio increases, nucleation becomes dominant and more nuclei are produced. For a given amount of Au reacting, the same amount of material is spread over more nuclei for high k1/k2, leading to smaller particles. Control over the size of primaries formed will involve tuning the relative rates of nucleation and growth.

The key factor affecting the relative rates k1 and k2 is the strength of the reducing agent. Sodium borohydride is a strong reducing agent, and for the correspondingly high k1 gold was rapidly consumed during nucleation.[11,12,62,63] Subsequent growth in the presence of sodium borohydride was limited as Au monomer had been depleted during nucleation. Each nucleus grew into an individual particle, and sizes remained small at ~5 nm. In contrast, when using a weaker reducing agent, such as aminodextran at high temperatures, the rate of nucleation was lessened (k_1 is relatively smaller with respect to k_2). Therefore, the number of nuclei was reduced. Furthermore, autocatalytic growth onto Au surfaces was more prevalent resulting in ~20 nm particles.[21] A similar trend was observed when formamide was used as the reducing agent leading to 30 nm particles.[64] In this paper, a moderate reducing agent was utilized to synthesize nanoparticles with an intermediate size. Hydroxylamine and glucose were utilized to reduce Au precursor into ~10 nm gold particles.

The rate expression for consumption of Au monomer in the autocatalytic reaction is[59,60]

$$\frac{d[Au^0]}{dt} = k_1[Au^{3+}] + k_2[Au^{3+}][Au^0] = k_1[Au^{3+}] + k_2[Au^{3+}]([Au^{3+}]_0 - [Au^{3+}]) \tag{4}$$

because the expression for amount of reduced gold can be written . As the reaction proceeds, the growth contribution will thus depend on the amount of Au injected. Higher initial injections will favor growth over nucleation as is greater, leading to increased particle size. The D_h of nanoclusters synthesized with a single Au injection of 0.036 mM resulted in larger clusters at ~67 nm than those clusters synthesized with two smaller injections of 0.018 mM with a D_h of ~46 nm as shown in Figure 2a and summarized in Table 1. Thus, another parameter controlling the particle size is the level of Au monomer initially injected.

2.4.2 Nanocluster Synthesis

Previous clustering of particles was initiated by manipulating forces that govern particle-particle interactions.[11] Repulsion of particles is provided through electrostatic and steric interactions. Van der waals, VdW, forces supply an attractive potential between nanoparticles. The total interaction potential between particles is represented as a superposition of these potentials[11]:

$$\text{Vtotal} = \text{Velectrostatic} + \text{Vsteric} + \text{VvdW} \qquad (5)$$

The electrostatic repulsion between particles is given by[65]

$$\frac{V_{EL}}{k_B T} = \frac{64\pi R \Gamma_0^2 \eta_\infty}{\kappa^2} exp(-\kappa[r-2R]) V_{VdW} \qquad (6)$$

where R is the radius of the particle, Γ_0 is a function of ψ_0 the particle surface potential[65], η_∞ is the bulk ion concentration, κ is the inverse Debye length and r is the center to center distance between two particles. Note that the magnitude of the electrostatic repulsion depends on both the charge and the size of the particles. VdW attraction between spheres of equal radii is described by the equation[65]

$$V_{VdW} = \frac{-A}{6}\left(\frac{2R^2}{d(4R+d)} + \frac{2R^2}{(2R+d)^2} + \ln\left(\frac{d(4R+d)}{(2R+d)^2}\right)\right) \qquad (7)$$

where A is the Hamaker constant of particles interacting in an aqueous medium, R is the radius of the particles, and d is the interparticle distance between particle surfaces. The steric interactions will depend on ligands attached to the nanoparticle surface, and will be taken into consideration later.

Clustering of nanoparticles requires a reduction in the stability of the primary particles by way of attractive forces that are stronger than stabilizing, repulsive forces. Tam et al. directed the formation of clusters by screening the electrostatic charge of ~5 nm citrate coated gold particles using an adsorbing polymer to lessen electrostatic repulsion.[11,12] High volume fractions of particles generated sufficient VdW forces to overcome the weakened electrostatic repulsive force. Thus, the ~5 nm gold particles aggregated into controlled clusters with diameters ranging from 30-100 nm.

Nanoparticle stability can also be reduced using solutions with high ionic strength or pH near the isoelectric point of the particles.[66-68] Solutions near the isoelectric point will reduce the charge per area on the surface of particles, thus reducing the electrostatic potential by reducing Γ_0 in Eq. 6. High ionic solutions will also alter the repulsive potential by reducing the length of electrostatic interactions. Goia et al. utilized high ionic solutions in order to cluster ~15 nm gold particles into clusters stabilized by gum arabic.

We present a mechanism where colloidal forces are manipulated to form nanoclusters from growing primary particles as shown in Scheme 1. Repulsive electrostatic forces were relatively weak on the primary particles as the surface charge was low. Polymer that was weakly adsorbed to the gold surface also contributed a steric component to repulsion. The VdW force between particles strengthened as primary particle autocatalytic growth increased particle sizes, as shown for increasing r in Eq. 7. Particle aggregation was initiated when VdW forces were sufficient to overcome the steric and electrostatic repulsive forces. The choice of polymeric stabilizer in CMD, that would also contribute electrostatically to repulsion, had little effect on particle sizes as shown experimentally by comparing Figure 2b and Figure 2c. The repulsive forces present from the adsorbed polymer were likely too low to prevent particle aggregation as a result of incomplete coverage of primary particle surfaces.

The formation of size selective clusters from primary particles has been studied using a theoretical model by Matijevic and Goia et al. Nanoclusters presented in Figure 2a exhibited narrow size distributions as one iteration clusters had an average D_h of ~33 nm with a standard deviation of 2 nm (Figure 2a).

According to Matijevic, the aggregation of primaries would result in the focusing of nanocluster sizes given specific reaction conditions. Firstly, it was assumed that addition of primaries was diffusion controlled as capture of primaries is irreversible.[66-68] Tuning colloidal forces such that attraction greatly outweighs repulsion allows diffusion controlled attachment for nanocluster growth.

Also, cluster to cluster aggregation needs to be avoided so the population exhibits a single, sharp peak.[66-68] Stability of kinetically assembled clusters is observed for experiments using CMD as a coating with D_h around 46 nm as well as dextran with a D_h of ~49nm as shown in Figure 2b and Figure 2c, respectively. Prevention of aggregation of clusters is achieved as the nanoclusters are sparsely populated in the system and are not likely to collide as a result of the forces of population dynamics.[66-68] Using Au concentrations of 0.018mM for the cluster synthesis shown in Figure 2a ensured dilute concentrations of clusters. Goia et al. utilized ~4 orders of magnitude higher Au concentrations to synthesize monodisperse clusters of primaries. Furthermore, the diffusion constant of primary particles is much greater than that of clusters as the size of primaries is significantly less than the size of clusters. The faster diffusing primaries are more likely to interact with the surface of slower diffusing clusters than other clusters. Thus, the prevalent method for cluster growth is through primary to cluster particle attachment.

The last condition for size focusing described by Matijevic is that the process of forming primaries must be coupled with the process of forming clusters.[66-68] Specifically, the progression of clustering of primaries must occur later in the process of primary particle formation. Furthermore, the concentration of primary particles in solution must be decreasing in time as particles become incorporated into clusters. The initial nucleation burst followed by autocatalytic growth reduces Au monomer supersaturation, thus mitigating nucleation of new particles simultaneously with cluster formation.

The growth of clusters “focuses” in terms of the diameter distribution of the clusters as they grow larger.[66-68] This focusing is analogous to the focusing observed in the homogeneous nucleation and growth of particles.[69,70] The number of primary particles needed to increase the diameter of a cluster by a preset amount becomes larger with the size of the cluster due to the geometric effect that the diameter increases as volume raised to the third. Therefore, smaller clusters grow faster and larger clusters grow slower leading to narrowing of the size distribution of the clusters as the primaries are added at the same rate to the clusters in the diffusion controlled regime of cluster growth. This effect which is mentioned in Park et al. is in agreement with what is observed for the analogous case of homogeneous nucleation and growth of nanoparticles.[66-70]

Further stability is provided for entire clusters by polymers adsorbed at the cluster surface that provide steric repulsion. High organic loadings of CMD at 50% and dextran at 40% prevent aggregation of clusters synthesized at pH 8.7 (Figure 5). The single sharp peaks exhibited by the CMD and dextran nanoclusters with standard deviations of 4% and 6%, respectively, reinforces the stability provided by the polymer stabilizers.

Existing cluster growth resulted from additional injections of Au monomer as depicted in panel 2 of Scheme 1. Heightened concentrations of Au monomer in the presence of clusters resulted in a burst of new nuclei. Similar Au nuclei were observed for Au injections in the presence of 12nm Au particles by Jana et al. Rapid growth of these newly formed primaries mitigated growth on existing Au clusters.[70] As the newly formed primaries grew, the increased VdW forces and high diffusion constant caused them to attach to the surface of existing nanoclusters, evidenced in Figure 1b. As shown in Figure 2a, these newly incorporated primaries on the surface of clusters resulted in an increase of D_h with an additional injection of Au to existing nanoclusters.

2.4.3 Nanoflower Synthesis

Morphological differences are introduced during the synthesis of nanoflowers compared to nanoclusters as shown in the third panel of Scheme 1. During nanoflower synthesis at pH 9.0 and pH 9.3, the initial injection of Au resulted in spherical particles with a smooth surface, demonstrated in Figure 6a and Figure 9a. Also, the SPR of these particles was representative of a sphere with a sharp peak near 530 nm as shown in Figure 8b and Figure 10b. At pH 9.0 and 9.3, the rate of Au reduction is slower than at pH 8.7 as the rate of reduction of Au precursor is inversely related to pH.[61] As seen in the synthesis of nanoclusters, injections of Au monomer at the higher pH values yielded primary particles that clustered as a result of dominant VdW forces. However, Au monomer is not significantly depleted from solution as seen at pH 8.7 as a result of the lower rate of reduction. Thus, precursor remaining in solution is reduced directly onto cluster surfaces such that the thermodynamically desirable spherical morphology is favored.

Upon further injections of Au monomer, the surface of the nanoparticles shifted from smooth to rough demonstrated in Figure 6b and 9b. This resulted in a redshift of SPR as shown in Figure 8b and 10b. Also, the D_h measured by DLS of the clusters increased as seen in Figure 8a and 10a. The Au injection in the presence of Au spheres induced nucleation of new primaries as previously observed for Au injections in the presence of nanoclusters. Furthermore, these nuclei grew rapidly and clustered to the surface of existing spherical particles as a result of increasing VdW forces and insufficient polymer coverage. The roughened surface of nanoflowers was maintained as insufficient levels of Au remained to completely cover and remove protrusions on the surface. Continued iterations of Au monomer repeated the process of primary particle formation and attachment to the surface. The increase in size is shown experimentally in Figure 8a and Figure 10a.

The immediate formation of clusters following the initial injection of Au is crucial to synthesizing nanoclusters with high NIR in sizes <50 nm. By adjusting the pH of the reducing solution to 8.7, formation of primary particles that aggregate to form clusters is favored (Scheme 1 and Figure 1a). For these nanoclusters, there is no evidence that Au ions reduce onto the cluster surface removing interparticle gaps and roughness that result from particle clustering (Figure 1). As shown in Figure 7 and Figure 10, at pH 9.0 or 9.3, high NIR cross sections at 800nm were not achieved for nanoflowers <50 nm. The initial spherical particle was incorporated into the nanoflowers as a solid, symmetric core that added to overall particle size without contributing to NIR extinction.

2.4.4 Comparison to Existing Au nanoparticles

As mentioned, nanoclusters synthesized using ~5 nm nanoparticles have been demonstrated by Tam et al resulting in ~30 nm nanoclusters and significant NIR extinction that gradually decreased as cross sections approached 900 nm. The NIR shift is attributed to high gold volume fractions and low polymer loadings in clusters that allow close spacings between primary particles. The small secondary stabilizer, citrate or lysine, provided a limit to interparticle spacing due to steric repulsion between these tightly bound surface ligands. In contrast, clusters synthesized through chemical reaction without secondary stabilizers, as presented here, have potential for closer spacing between primaries.

It has been shown that Au/iron oxide nanoclusters may be synthesized with NIR extinction peaks at ~750 nm for a Dh of ~35 nm through the reduction of Au monomer in the presence of iron oxide.[2] The close spacing of asymmetric gold domains and porosity of the nanoclusters favors high NIR extinction. Stabilization of these Au/iron oxide nanoclusters was achieved using two adsorbing polymers, dextran and polyvinyl alcohol. The gold only nanoclusters presented utilized a single polymer for stabilization. The magnetic properties of iron oxide are of interest for certain dual mode magnetic and optical applications. In the case where no magnetic functionality is required, the composite system is not necessary as only Au contributes to the optical properties of the clusters.

An alternative is the formation of nanonages that have edge lengths of 45 nm and an extinction peak of ~840 nm.[19] During nanocage synthesis, presynthesized Ag nanocubes are used as particle templates for a surface galvanic displacement reaction of Au for Ag. Resulting NIR extinctions are a result of the hollow structure, thin gold domain, and sharp nanocage edges.

Previous Au nanoflowers and nanostars have been shown to produce NIR shifts similar to the nanoflowers presented here. In the case of nanoflowers with small diameters around ~50 nm, the SPR shift was insufficient for high extinction cross sections at 800 nm.[31,34-36] Sufficient NIR extinction was only realized for particles with overall diameters approaching 100 nm.[33,37,41,42] The necessary large sizes for significant SPR shifts in nanoflowers are a result of the solid, symmetric core as seen for the nanoflowers presented herein. The nanoflower core contributes to the overall size of the nanoparticle with minimal contribution to shifting the SPR.

2.5 CONCLUSION

Strong extinction in the NIR region between 800-1100nm has been attained for gold nanoparticles smaller than 50nm. The nanoclusters exhibited very broad extinction spectra with a peak around 690nm in a cluster with an overall hydrodynamic diameter of

~45nm. The large red shift in the SPR is a result of close spacing between gold domains, and devations from a purely spherical geometry for the primary particles. Au nanoclusters were synthesized by first nucleating and growing nanoparticles homogeneously in the presence of a weakly adsorbing polymer. Growing nanoparticles aggregated into clusters as a result of Van der Waals attraction indicating the size of the primary particles was sufficient for clustering. The nanocluster size was mediated by controlling growth of primary particles with the Au monomer/polymer ratio and Au precursor concentration. The polydispersity was low. A small amount of additional growth on the primary particles makes them less spherical; this asymmetry further shifts the spectra into the NIR. This nonspherical growth is more prevalent at pH 8.7 versus 9. For two iterations, attachment of new primary particles to existing clusters further extends the spectra into the NIR. The spectra and morphology of these nanoclusters are somewhat similar to those formed by kinetically controlled physical assembly[11,12] of pre-synthesized primary particles. Unlike the case for the physical assembly, in the current study, the nanocluster synthesis is performed in a single step and with only a single polymeric stabilizer, without a secondary stabilizer for the primary particles. For nanostars, the required size is on the order of ~100 nm to achieve NIR at 1000nm.[33,37,41,42] The lack of a seed core allows for smaller sizes for the NIR active nanoclusters for two reasons. First, the core adds to the size. Secondly, a spherical seed core does not contribute to NIR extinction. In contrast all of the nanocluster comprises of asymmetric domains that contribute in the NIR. Stabilization of clusters is provided by charged (CMD) or uncharged (dextran) polymer on the particle surface. Given polymers both result in similar sizes, the electrostatic component for CMD was not needed. These small nanoparticles with intense NIR extinction are of great interest in cellular and optical imaging as well as therapy for such diseases such as atherosclerosis and cancer.

2.6 References

(1) Hirsch, L. R.; Stafford, R. J.; Bankson, J. A.; Sershen, S. R.; Rivera, B.; Price, R. E.; Hazle, J. D.; Halas, N. J.; West, J. L. *Proc. Nat. Acad. Sci.* **2003**, *100*, 13549.

(2) Ma, L. L.; Feldman, M. D.; Tam, J. M.; Paranjape, A. S.; Cheruku, K. K.; Larson, T. A.; Tam, J. O.; Ingram, D. R.; Paramita, V.; Villard, J. W.; Jenkins, J. T.; Wang, T.; Clarke, G. D.; Asmis, R.; Sokolov, K.; Chandrasekar, B.; Milner, T. E.; Johnston, K. P. *Acs Nano* **2009**, *3*, 2686.

(3) Zhang, J.; Sasaki, K.; Sutter, E.; Adzic, R. R. *Science* **2007**, *315*, 220.

(4) Anker, J. N.; Hall, W. P.; Lyandres, O.; Shah, N. C.; Zhao, J.; Van Duyne, R. P. *Nat. Mater.* **2008**, *7*, 442.

(5) Stewart, M. E.; Anderton, C. R.; Thompson, L. B.; Maria, J.; Gray, S. K.; Rogers, J. A.; Nuzzo, R. G. *Chem. Rev.* **2008**, *108*, 494.

(6) Arruebo, M.; Fernandez-Pacheco, R.; Ibarra, M. R.; Santamaria, J. *Nano Today* **2007**, *2*, 22.

(7) Betancourt, T.; Brown, B.; Brannon-Peppas, L. *Nanomedicine* **2007**, *2*, 219.

(8) Boal, A. K.; Ilhan, F.; DeRouchey, J. E.; Thurn-Albrecht, T.; Russell, T. P.; Rotello, V. M. *Nature* **2000**, *404*, 746.

(9) Davis, M. E.; Chen, Z.; Shin, D. M. *Nat. Rev. Drug Discov.* **2008**, *7*, 771.

(10) Kooi, M. E.; Cappendijk, V. C.; Cleutjens, K.; Kessels, A. G. H.; Kitslaar, P.; Borgers, M.; Frederik, P. M.; Daemen, M.; van Engelshoven, J. M. A. *Circulation* **2003**, *107*, 2453.

(11) Tam, J. M.; Murthy, A. K.; Ingram, D. R.; Nguyen, R.; Sokolov, K. V.; Johnston, K. P. *Langmuir* **2010**, *26*, 8988.

(12) Tam, J. M.; Tam, J. O.; Murthy, A.; Ingram, D. R.; Ma, L. L.; Travis, K.; Johnston, K. P.; Sokolov, K. V. *Acs Nano* **2010**, *4*, 2178.

(13) Douma, K.; Prinzen, L.; Slaaf, D. W.; Reutelingsperger, C. P. M.; Biessen, E. A. L.; Hackeng, T. M.; Post, M. J.; van Zandvoort, M. *Small* **2009**, *5*, 544.

(14) Durr, N. J.; Larson, T.; Smith, D. K.; Korgel, B. A.; Sokolov, K.; Ben-Yakar, A. *Nano Letters* **2007**, *7*, 941.

(15) Jiang, Y. Q.; Horimoto, N. N.; Imura, K.; Okamoto, H.; Matsui, K.; Shigemoto, R. *Adv Mater* **2009**, *21*, 2309.

(16) Zhu, J.; Yong, K. T.; Roy, I.; Hu, R.; Ding, H.; Zhao, L. L.; Swihart, M. T.; He, G. S.; Cui, Y. P.; Prasad, P. N. *Nanotechnology* **2010**, *21*.

(17) Qiu, L.; Larson, T. A.; Smith, D. K.; Vitkin, E.; Zhang, S. H.; Modell, M. D.; Itzkan, I.; Hanlon, E. B.; Korgel, B. A.; Sokolov, K. V.; Perelman, L. T. *Ieee Journal of Selected Topics in Quantum Electronics* **2007**, *13*, 1730.

(18) Adler, D. C.; Huang, S. W.; Huber, R.; Fujimoto, J. G. *Optics Express* **2008**, *16*, 4376.

(19) Skrabalak, S. E.; Chen, J.; Au, L.; Lu, X.; Li, X.; Xia, Y. *Adv Mater* **2007**, *19*, 3177.

(20) Ma, L., University of Texas at Austin, 2010.

(21) Ma, Y.; Li, N.; Yang, C.; Yang, X. R. *Analytical and Bioanalytical Chemistry* **2005**, *382*, 1044.

(22) Schipper, M. L.; Iyer, G.; Koh, A. L.; Cheng, Z.; Ebenstein, Y.; Aharoni, A.; Keren, S.; Bentolila, L. A.; Li, J. Q.; Rao, J. H.; Chen, X. Y.; Banin, U.; Wu, A. M.; Sinclair, R.; Weiss, S.; Gambhir, S. S. *Small* **2009**, *5*, 126.

(23) Daniel, M. C.; Astruc, D. *Chem. Rev.* **2004**, *104*, 293.

(24) Hu, Y.; Noelck, S. J.; Drezek, R. A. *Acs Nano* **2010**, *4*, 1521.

(25) Knight, M. W.; Halas, N. J. *New Journal of Physics* **2008**, *10*.

(26) Levin, C. S.; Hofmann, C.; Ali, T. A.; Kelly, A. T.; Morosan, E.; Nordlander, P.; Whitmire, K. H.; Halas, N. J. *Acs Nano* **2009**, *3*, 1379.

(27) Ma, L. L.; Tam, J. O.; Willsey, B. W.; Rigdon, D.; Ramesh, R.; Sokolov, K.; Johnston, K. P. *Langmuir* **2011**, *27*, 7681.

(28) Huang, X.; El-Sayed, I. H.; Qian, W.; El-Sayed, M. A. *Journal of the American Chemical Society* **2006**, *128*, 2115.

(29) Pissuwan, D.; Valenzuela, S. M.; Killingsworth, M. C.; Xu, X. D.; Cortie, M. B. *J. Nanopart. Res.* **2007**, *9*, 1109.

(30) Loo, C.; Lowery, A.; Halas, N. J.; West, J.; Drezek, R. *Nano Letters* **2005**, *5*, 709.

(31) Kuo, C. H.; Huang, M. H. *Langmuir* **2005**, *21*, 2012.

(32) Nehl, C. L.; Liao, H. W.; Hafner, J. H. *Nano Letters* **2006**, *6*, 683.

(33) Zou, X. Q.; Ying, E. B.; Dong, S. J. *Nanotechnology* **2006**, *17*, 4758.

(34) Lu, L. H.; Ai, K.; Ozaki, Y. *Langmuir* **2008**, *24*, 1058.

(35) Wang, W.; Yang, X.; Cui, H. *Journal of Physical Chemistry C* **2008**, *112*, 16348.

(36) Zhao, L. L.; Ji, X. H.; Sun, X. J.; Li, J.; Yang, W. S.; Peng, X. G. *Journal of Physical Chemistry C* **2009**, *113*, 16645.

(37) Barbosa, S.; Agrawal, A.; Rodriguez-Lorenzo, L.; Pastoriza-Santos, I.; Alvarez-Puebla, R. A.; Kornowski, A.; Weller, H.; Liz-Marzan, L. M. *Langmuir* **2010**, *26*, 14943.

(38) Li, L. M.; Weng, J. *Nanotechnology* **2010**, *21*.

(39) Senapati, D.; Singh, A. K.; Ray, P. C. *Chemical Physics Letters* **2010**, *487*, 88.

(40) Wang, Z. D.; Zhang, J. Q.; Ekman, J. M.; Kenis, P. J. A.; Lu, Y. *Nano Letters* **2010**, *10*, 1886.

(41) Trigari, S.; Rindi, A.; Margheri, G.; Sottini, S.; Dellepiane, G.; Giorgetti, E. *Journal of Materials Chemistry* **2011**, *21*, 6531.

(42) Van de Broek, B.; Frederix, F.; Bonroy, K.; Jans, H.; Jans, K.; Borghs, G.; Maes, G. *Nanotechnology* **2011**, *22*.

(43) Lazarides, A. A.; Schatz, G. C. *Journal of Physical Chemistry B* **2000**, *104*, 460.

(44) Sokolov, K.; Follen, M.; Aaron, J.; Pavlova, I.; Malpica, A.; Lotan, R.; Richards-Kortum, R. *Cancer Res.* **2003**, *63*, 1999.

(45) Aaron, J.; Nitin, N.; Travis, K.; Kumar, S.; Collier, T.; Park, S. Y.; Jose-Yacaman, M.; Coghlan, L.; Follen, M.; Richards-Kortum, R.; Sokolov, K. *Journal of biomedical optics* **2007**, *12*.

(46) Ofir, Y.; Samanta, B.; Rotello, V. M. *Chemical Society Reviews* **2008**, *37*, 1814.

(47) Wilcoxon, J. P.; Martin, J. E.; Schaefer, D. W. *Phys. Rev. A* **1989**, *39*, 2675.

(48) Chow, M. K.; Zukoski, C. F. *Journal of Colloid and Interface Science* **1994**, *165*, 97.

(49) Lee, D.; Donkers, R. L.; Wang, G. L.; Harper, A. S.; Murray, R. W. *Journal of the American Chemical Society* **2004**, *126*, 6193.

(50) Jimenez, V. L.; Georganopoulou, D. G.; White, R. J.; Harper, A. S.; Mills, A. J.; Lee, D. I.; Murray, R. W. *Langmuir* **2004**, *20*, 6864.

(51) Jaffer, F. A.; Libby, P.; Weissleder, R. *Journal of the American College of Cardiology* **2006**, *47*, 1328.

(52) Larson, T. A.; Bankson, J.; Aaron, J.; Sokolov, K. *Nanotechnology* **2007**, *18*, 325101/1.

(53) Kim, J. W.; Galanzha, E. I.; Shashkov, E. V.; Moon, H. M.; Zharov, V. P. *Nature Nanotechnology* **2009**, *4*, 688.

(54) Shah, J.; Park, S.; Aglyamov, S.; Larson, T.; Ma, L.; Sokolov, K.; Johnston, K.; Milner, T.; Emelianov Stanislav, Y. *Journal of biomedical optics* **2008**, *13*, 034024.

(55) Xu, M. H.; Wang, L. H. V. *Rev. Sci. Instrum.* **2006**, *77*.

(56) Ryoo, W.; Webber, S. E.; Johnston, K. P. *Industrial & Engineering Chemistry Research* **2003**, *42*, 6348.

(57) Jana, N. R.; Gearheart, L.; Murphy, C. J. *Chemistry of Materials* **2001**, *13*, 2313.

(58) Yin, Y.; Alivisatos, A. P. *Nature* **2005**, *437*, 664.

(59) Watzky, M. A.; Finke, R. G. *Journal of the American Chemical Society* **1997**, *119*, 10382.

(60) Finney, E. E.; Finke, R. G. *Journal of Colloid and Interface Science* **2008**, *317*, 351.

(61) Ji, X. H.; Song, X. N.; Li, J.; Bai, Y. B.; Yang, W. S.; Peng, X. G. *Journal of the American Chemical Society* **2007**, *129*, 13939.

(62) Grabar, K. C.; Allison, K. J.; Baker, B. E.; Bright, R. M.; Brown, K. R.; Freeman, R. G.; Fox, A. P.; Keating, C. D.; Musick, M. D.; Natan, M. J. *Langmuir* **1996**, *12*, 2353.

(63) Brust, M.; Walker, M.; Bethell, D.; Schiffrin, D. J.; Whyman, R. *Journal of the Chemical Society, Chemical Communications* **1994**, 801.

(64) Han, M. Y.; Quek, C. H.; Huang, W.; Chew, C. H.; Gan, L. M. *Chem. Mat.* **1999**, *11*, 1144.

(65) Hiemenz, P. C.; Rajagopalan, R. *Principles of Colloid and Surface Chemistry*; 3rd ed. ed.; Marcel Dekker, Inc.: New York, 1997.

(66) Goia, D. V.; Matijevic, E. *Colloids and Surfaces a-Physicochemical and Engineering Aspects* **1999**, *146*, 139.

(67) Matijevic, E. *Colloid Journal* **2007**, *69*, 29.

(68) Park, J.; Privman, V.; Matijevic, E. *Journal of Physical Chemistry B* **2001**, *105*, 11630.

(69) Talapin, D. V.; Rogach, A. L.; Haase, M.; Weller, H. *Journal of Physical Chemistry B* **2001**, *105*, 12278.

(70) Yin, Y.; Alivisatos, A. P. *Nature* **2005**, *437*, 664.

Appendix A: Selective Targeting of Antibody Conjugated Multifunctional Nanoclusters (Nanoroses) to Epidermal Growth Factor Receptors in Cancer Cells

The ability of smaller than 100 nm antibody nanoparticle conjugates to target and modulate the biology of specific cell types may enable major advancements in cellular imaging and therapy in cancer. A key challenge is to load an extremely high degree of targeting, imaging, and therapeutic functionality into small, yet stable particles. A versatile method called thin autocatalytic growth on substrate (TAGs) has been developed in our previous study to separate the nucleation of gold seeds onto iron oxide nanoparticles followed by limited growth to form ultra-thin and asymmetric gold coatings. The 35 nm asymmetric thin gold coated iron oxide nanoclusters produce exceptional near infrared (NIR) absorbance and superparamagnetism for an enhanced r_2 spin-spin relaxivity. Herein, a novel conjugation technique further allows covalent binding of anti-epidermal growth factor receptor (EGFR) monoclonal antibody (Ab) clone 225 to the nanoclusters to realize highly selective targeting to EGFR over expressing cancer cells. AlexaFluor 488 tagged clone 225 nanocluster conjugates were prepared to correlate the number of conjugated antibodies with the hydrodynamic size of the naoclusters. For 1 to 74 Abs on a nanorose surface, the correlated hydrodynamic diameters varied from 35 to 78 nm, as measured by dynamic light scattering (DLS). A transition from sub-monolayer to multilayer aggregates of Abs on the nanoparticle surface was observed for 54 Abs and an overall particle diameter of 63 nm.

The targeting efficacy of the conjugated nanoclusters was evaluated by the A431 cancer cell uptake characterized by dark field reflectance imaging and atomic absorbance spectrometry (AAS) essay analysis on Au element. Dual mode *in-vitro* imaging studies with dark field reflectance microscopy and fluorescence microscopy demonstrate that these multifunctional nanoclusters may be used as NIR and fluorescent contrast agents for ‘theranostisc’ of EGFR expressing cancer cells.

A.1 INTRODUCTION

Development of multifunctional nanoparticles to monitor targeted drug delivery non-invasively and to determine the therapeutic response rapidly will provide a new paradigm for cancer treatment in the clinic. Whereas, nanoparticles are typically used either for molecular imaging or therapy,[2,28,30,44,71-73] recent efforts are underway to do both simultaneously. For example, magnetic resonance imaging (MRI) and ultrasound imaging have been utilized to monitor temperature changes during photothermal therapy.[2,54,74] However, nanoparticles possessing multifunctional properties for achieving both molecular imaging and real time feedback on therapeutic efficacy for cancer treatment are not yet utilized in the clinic. Thus, a key challenge in nanomedicine is to synthesize therapeutic nanoparticles coated with biomarkers for high targeting efficiency and with strong near infrared (NIR) absorbance and/or magnetic properties for imaging and therapy.[75]

In passive delivery of polyethylene glycol (PEG) coated gold nanoparticles, the particles permeate leaky vasculatures and accumulate in tumor interstitial space.[76,77] An antibody (Ab) or small antibody fragment may be coated on the particle surface to target biomarker receptors and greatly enhance accumulation at the tumor site.[75,78] There are two key conjugation protocols available for attachment of peptides or proteins on the surface of nanoparticles. In the first or indirect method, functional groups, for example, COOH, on the polymer coatings of the nanoparticle surfaces are conjugated to primary amine groups, which may be on either the Fc (nonbinding region) or Fab region (binding region).[79] For example, EDC/Sulfo-NHS chemistry has been widely adopted for nanospheres,[78,79] nanoshells[30] and nanorods.[80] In a recent study of gold nanorods with this method, the total gold accumulation in xenograft tumor models was only marginally improved in comparison with nontargeted controls.[80] In the direct method, the Fc region of an Ab is first coupled with a low molecular weight heterobifunctional linker such as dithiol-PEG-hydrazide(MW 708.97), whereby the dithol group is conjugated directly to the Au surface. The coupling is achieved with a selective reaction between the hydrazide end group and an aldehyde, formed by mild oxidation of a carbohydrate side chain on the Fc region.[52,81-85] Selective binding to the Fc region of an Ab is beneficial for maximizing the biological activity of the Fab binding regions.[83,84,86-88] This conjugation strategy allows for the multiplexing of various glycosylated antibodies on a single nanoparticle for monitoring therapeutic agents in vivo.[89,90] Thus, the high surface density of gold atom conjugation sites serves as a high versatile substrate for binding of these multiple types of functional biomolecules with relatively simple conjugation chemistry.

In cancer nanomedicine, an extremely high degree of targeting, NIR absorbance, magnetization and therapeutic functionality must be loaded into small, yet stable particles. Particles in the range of 35 to 65 nm are highly effective in bypassing the reticuloendothelial system (RES) (liver and spleen).[91-93] Gold coated iron oxide particles are of interest for both magnetic and optical functionality, and may exhibit relatively low toxicity.[2,75,94] To drive nucleation of Au seeds on unfavorable low energy iron oxide surfaces, high supersaturation values are often utilized, with Au^{3+}/Fe mass ratios in the order of 10.[94-96] Excessive autocatalytic growth often produces shells on the order of 10 nm.[26,97-100] The surface plasmon resonance (SPR) for the thick shells is typically in the visible, rather than the NIR region. Furthermore, the thick shells take up space needed for the Abs, and other functional components such as iron oxide, given the limitation of the small overall particle size. To address these severe space requirements, 35 nm multifunctional iron oxide nanoparticles were designed with very thin Au shells (< 5 nm), yet strong NIR absorbance (cross section of ~10^{-14} m^2 at 755 nm).[2] For cancer imaging/therapy, it would be desirable to conjugate Abs onto this type of small multifunctional nanoparticle, while achieving colloidal stability. Very recently, it has been found that the particle curvature and shape impact cellular targeting as seen for nanocages,[101] ellipsoids, rods, cylinders and disks, in addition to spheres.[102-104] The design of multifunctional nanoparticles with various surface curvatures and control of the density and orientation of Abs on the surface has the potential to have a large impact on cellular uptake and therapy in nanomedicine.

Herein, we have conjugated monoclonal anti-EGFR antibodies to multifunctional nanoparticles (nanorose) composed of thin knobby Au coatings on magnetic iron oxide cores, with a tunable number, from 1 to 74, of conjugated Abs. As the number of Abs increased, the hydrodynamic diameter measured by dynamic light scattering (DLS), increased from 35-78 nm. High surface coverage of Abs is favored by the high density of conjugation sites supplied by Au atoms on the surface and the low cross sectional area of the heterobifunctional dithiol-PEG-hydrazide (MW 708.97) linker. The thin Au shells and the low MW linker take up relatively little space, leaving substantial room for other functional components (iron oxide) and Abs, despite the small overall particle size. Furthermore, because the Au shells are so thin, the amount of steric stabilizer (mPEG-SH, MW 5,000) needed to counteract VDW forces may be expected to be unusually low relative to more common particles with thicker Au shells.[97] The number of clone 225 Abs conjugated to the nanorose was tuned from sub-monolayer to multilayer coverage as characterized by labeling the Abs with AlexaFluor 488 fluorophore. For 54 Abs, the hydrodynamic diameter indicated coverage of a monolayer for Abs, in agreement with the prediction of a geometric model, by assuming a circular area for the Fab region.

Highly uptake of conjugated nanorose for A431 skin cancer cells was observed with dark field and fluorescence microscopy, as quantified by flame atomic absorption spectroscopy (AAS). The intensive orange color under dark field indicates high NIR scattering by the thin Au shells on nanorose in agreement with previous hyperspectral images in macrophage cells for nanorose without Ab conjugation.[2] Fluorescence images show strong green emission from AlexaFluor 488 tagged clone 225 Abs inside cancer cells indicating the Abs stayed attached to the Au surfaces. The uptake of nanorose conjugated with an Ab monolayer reached 7000 particles/cell, more than previously reported for 50 nm Au spheres[105] with the same Ab and cell type. The high uptake is discussed in terms of the small hydrodynamic diameter, high degree of Ab conjugation, and the influence of the highly curved surfaces on the Ab orientations. These particles with NIR imaging, magnetic and therapeutic multifunctionality in a small overall particle size would be of interest in advancing molecular specific imaging combined with therapy.

A.2 EXPERIMENTAL SECTION

A.2.1 Materials

Monoclonal anti-EGF receptor antibody clone 225 (Sigma: E2156) and monoclonal anti-rabbit immunoglobulin clone RG-16 (Sigma: I0138) were obtained from Sigma-Aldrich Co. The antibody stock solutions were first purified by using a 100,000 molecular weight cutoff (MWCO) centrifugal filter (Amicon Ultra-4, Millipore Co.). Briefly, 200 µL (1.5 mg/mL) clone 225 stock solution was transferred into one filter device with 3 mL HEPES (pH 7.4, 40 mM) addition. The filter device was centrifuged for 14 mins at 3,220 xg. 300 µL HEPES was used to form a solution of the antibody at a final concentration of 1 mg/ml. Dithiol-alkane aromatic PEG_6-$NHNH_2$ ($C_{33}H_{60}N_2O_{10}S_2$, MW 708.97, SensoPath Technologies Inc., Bozeman, MT, USA), mPEG-SH (MW 5,000) from Nanocs Inc. (New York, NY, USA), PEG (MW 14,000) and $NaIO_4$ (213.89 MW) from Sigma-Aldrich Co. were used.

A.2.2 Antibody conjugation to nanorose

The 35 nm diameter thin gold coated iron oxide "nanorose" particles were assembled by using dextran as a stabilizer as reported in our previous paper.[2] Nanorose particles (2.4 mg Au) were then redispersed after centrifugation at 4,629 xg for 6 mins by using a 50 µL of 0.05 mg/ml (10^{-5} M) mPEG-SH water solution and 2 ml DI water to reach a concentration of ~ 1 mg Au/ml. The heterogeneous linker (dithiol-PEG-hydrazide) was used to covalently attach monoclonal antibodies to gold surfaces.[83,106] Briefly, the linker (MW 709 Da) consists of a short polyethylene glycol chain terminated at one end by a hydrazide group and at the other end by di-thiol groups. 300 µg clone 225 antibodies at a concentration of 1 mg/mL were first mixed with 300 µL of 10 mM $NaIO_4$ for 45 minutes at room temperature under mild agitation and protection from light. Here, the hydroxyl moieties on the antibodies' Fc region were oxidized to aldehyde groups. Then, one aliquot of dithiol-PEG-hydrazide linkers (5 µL, 50mM in ethanol) was added to the oxidized antibodies for 30 minutes. The hydrazide portion of the heterogeneous linker readily reacted with aldehydes on antibodies' Fc region to form a stable linkage. The unreacted linker and salts were removed with a 100,000 MWCO centrifugal filter (Millipore Co.) at 3,220 xg for 14 mins. The antibodies (clone 225-PEG-dithiol) remained on the filter and were resuspended in 300 µL HEPES (pH 7.4, 40 mM). After purification, the modified antibodies were mixed with nanoroses and dispersed in 30 mL of HEPES for 8 hours at 4 ^{o}C on a shaker. Stable covalent bonds were formed between the gold surfaces and the linker's dithiol groups during mixing. Subsequently, mPEG-SH (MW 5,000) molecules were added to passivate the gold surface on the nanoparticles unoccupied by antibodies. Nanorose conjugates were centrifuged at 4,629 xg for 6 mins and re-suspended in 2 mL HEPES (pH 7.4, 40mM). The concentrated nanorose-clone 225 conjugates were stored at 4^{o}C for further characterization and cell targeting. To measure non-specific binding of nanoparticles to cancer cells, anti-rabbit IgG (clone RG-16) antibodies that do not specifically bind to cancer cells were also conjugated to nanoroses by following the same procedure as for the clone 225.

A.2.3 Cell culture and nanoparticle targeting

EGFR (+) human epithelial carcinoma cells (A431 keratinocyte) were cultured in petri dishes using a 50/50 (v/v) mixture of phenol/serum free DMEM medium at 37 ^{o}C in a 5% CO_2 incubator till 80% confluence. Cells were harvested from plate by using trypsin and incubated for 5 mins. They were harvested and resuspended in 1 mL culture medium for cell counting. 10^6 cells/ml suspensions were typically harvested for nanoparticle labeling. Then, a designated number of cells were mixed with a known number of nanoparticles dispersed in 2 mL culture medium and allowed to interact for 60 mins on a shaker at room temperature. After labeling, the cells were centrifuged at 201xg for 3 mins to remove unbound particles in supernatant and re-suspended in 1×PBS. After a second round centrifugation at the same conditions to minimize impurities, the particle labeled cells were dissolved in 0.5 ml 1 mM HNO_3 for AAS elemental analysis. The labeled cells were also re-dispersed in 1×PBS for optical microscope imaging. EGFR (-)

MDA-MB-435 breast cancer cells were cultured and labeled under the same conditions as the control cell line.

A.2.4 Au elemental analysis in the labeled cells

After redispersing the nanoparticle labeled cells, the Au concentrations in the cell was obtained by flame atomic absorption spectroscopy (GBC Scientific Equipment Pty Ltd, 908AA, Melbourne, Australia). The apparatus was equipped with an air-acetylene flame furnace. The absorption of Au was recorded at 242.8 nm. The instrument was calibrated using Au^{3+} standard solutions before every set of measurements. All measurements were carried in diluted samples so that the concentration of Au was between 1 and 5 µg/ml.

A.2.5 Hydrodynamic diameter measurement of Abs conjugated nanoparticles

Dynamic light scattering (DLS) measurements were performed in triplicate on a custom made Brookhaven Instruments dynamic light scattering apparatus at a scattering angle of 90° and temperature of 25°C. [56] Abs conjugated nanoparticle dispersion concentrations were adjusted with 1×PBS to give a scattering signal counting rate between 300-400 kcps. Prior to DLS measurements, the samples were bath sonicated for 2 minutes. The autocorrelation functions were analyzed with a non-negative least-squares (NNLS) method to determine distributions by volume.[56]

A.2.6 Fluorescent labeling and UV-Vis spectrometry

Alexa Fluor 488 monoclonal antibody labeling kit (Invitrogen Co.) was used to label modified antibodies (clone 225-PEG-dithiol) by following the provided procedure. The fluorophore has a tetrafluorophenyl ester moiety that reacts efficiently with primary amines on the Abs to form stable dye-protein conjugates. The excitation and emission measurements were performed at the absorption peak (494 nm) of the Alexa Fluor 488 dye by using a BioTek Synergy HT multi-mode microplate reader (BioTek Instruments, Inc.). To precisely determine the absorbance or emission of the Abs on the nanorose, freshly prepared background solutions for baseline subtraction were analyzed simultaneously with samples in a 96-well plate. The concentrations of the fluorescent clone 225 were measured from the absorbance at wavelengths of 280 nm and 494 nm in a 1 cm optical path length cuvette according to the formula suggested by the guide in the fluorescent labeling kit:

$$\text{clone 225 concentration (mg/ml)} = \frac{(A_{280} - A_{494} \times 0.11) \times 160000}{203000} \tag{1}$$

The molecular weight of the clone 225 antibody was 160,000 g/mole, and the absorbance cross section was 203,000 cm^{-1} M^{-1}. A linear correlation between the emission intensity at 519 nm of the Alexa Fluor 488 labeled clone 225-PEG-dithiol versus concentration with a correlation coefficient r = 0.9986 was determined as shown in Figure A.1.

After mixing of the fluorescently labeled clone 225-PEG-dithiol to nanoroses as described in the antibody conjugation procedure, centrifugation at 4,629 xg for 6 mins was used to separate the conjugated nanoroses in the pellet from unbound antibodies in the supernatant. The fluorescence emission intensity of the supernatant for an excitation and emission wavelength of 494 nm and 519 nm, respectively, was measured to determine the concentration unbound antibodies by comparing with the correlation curve. The average amount of attached antibodies to nanorose was determined by subtracting the unbound antibodies from total.

A.2.7 Dark field reflectance imaging and fluorescent imaging

Dark field reflection images were captured with a Leica DM 6000 upright microscope using Xenon illumination along with a 20× dark-field objective (0.5 NA) and a Retiga EXi camera with 12-bit ultra-sensitive CCD camera detector, for imaging in a RGB mode (Q-imaging, Inc.). In dark-field microscopy, a sample is illuminated by a cone of light outside of the imaging angular acceptance aperture. The large scattering angle allows detection of highly scattering objects (such as nanoroses) with very little background signal. Fluorescence images were captured from the same microscope under fluorescence mode by collecting 520 nm emission signals (emission peak at 519 nm of Alexa Fluor 488) with an excitation wavelength at 490 nm (absorption peak at 494 nm of Alexa Fluor 488).

Scheme A.1 Geometric properties of antibody layers on model spherical particle surfaces (approximately to scale).

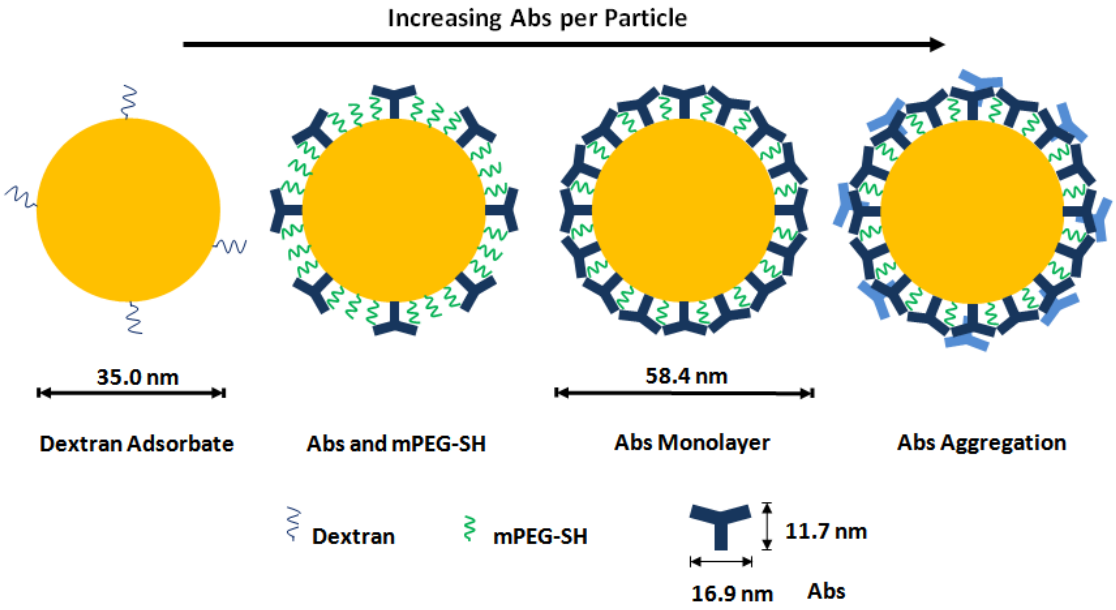

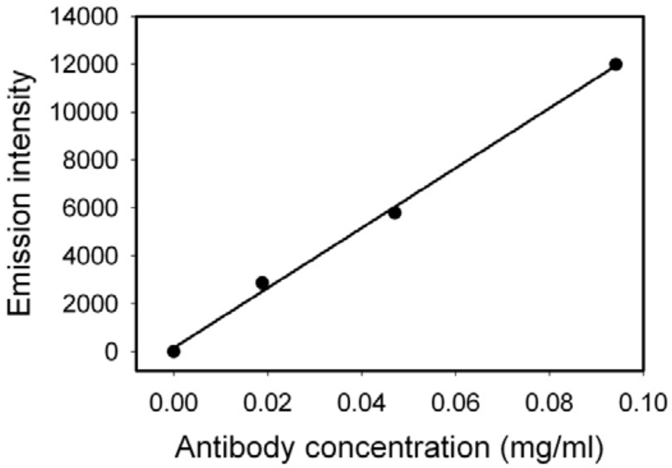

Figure A.1 Calibration curve for emission intensity (arbitrary units) at 519 nm of AlexaFluor 488 labeled clone 225 antibody versus concentration. The excitation was performed at the ABS peak maximum of 494nm of the AlexaFluor 488. A correlation coefficient r = 0.9986 was determined.

A.3 RESULTS

A.3.1 Number of clone 225 Abs conjugated to nanorose and hydrodynamic diameter

The average number of conjugated clone 225 antibodies on one nanorose was determined from fluorescence for the Alexa Fluor 488 labeled clone 225 antibody based on the calibration curve in Figure A.1 between emission intensity and . A predetermined amount (Table A.1) of Alexa Fluor 488 labeled clone 225-PEG-dithiol from a concentrated stock solution (0.565 mg/ml) was mixed with 6.2×10^{11} nanorose particles dispersed in 10 ml HEPES for the conjugation reaction. The number of nanorose particles was determined from elemental analysis by AAS.[2] As shown in Table A.1, the number of covalently attached clone 225 molecules per nanorose particle increased monotonically with the initially mixed antibody amount. When 303 clone 225-PEG-dithiol molecules were mixed with one nanorose particle, 54 were attached as determined by the calibration curve (Figure A.1). This number is on the order of a monolayer as will be quantified in detail in the discussion section.

The hydrodynamic diameter of the nanorose particles with different numbers of conjugated antibodies were measured in 1×PBS dispersion, before and after filtration with a 0.22 µm filter, by DLS (Figure A.2). As shown in Table A.1, the hydrodynamic diameters increased monotonically from 33 nm to 80 nm as the attached number of clone 225 molecules increased from 1 to 74. The vast majority of the particle hydrodynamic diameter distribution by volume was in the primary peak. A small secondary peak (~ 10 % by volume) was observed with a larger size, indicating a small population of particle aggregates (Figure A.2A and Table A.1). After filtration with a 0.22 µm pore size syringe filter, the second peak from particle aggregates was fully removed as shown by DLS (Figure A.2B and Table A.1). The hydrodynamic sizes of the non-aggregated particles (smaller peak) did not change significantly in the filtration process. This stability of the particles suggests that the antibody molecules and mPEG-SH were effective in providing steric stabilization.

The absorbance spectra of nanoroses (TEM image in Figure A.3B) were obtained before and after antibody conjugation (Figure A.3A). The very small change in spectra indicated high colloidal stability and stability in the Au shells for the particles. In addition, the Abs contributed little to the absorbance as expected, given the extremely strong cross section for the SPR of Au. In each case, a large shift to the NIR, relative to the spectra for Au spheres, is cause by asymmetry in the thin Au shells[2] as described below. We also determined the absorbance spectra for more well-known[94] spherical control particles with a 50 nm diameter and thick gold shells (TEM image in Figure A.3B) on the same iron oxide core as for the nanorose in Figure A.3A. At 755 nm, the extinction coefficients for the nanorose particles with thin asymmetric shells (0.0537-0.0563 cm^2/µg Au) were over five times those of the control particles with thick smooth gold shells (0.0085-0.0106 cm^2/µg Au) as shown in Table A.2. For similar particles, ~ 20 nm thick smooth gold shells on ~10 nm iron oxide cores are often too thick to shift the SPR peak of pure gold at 530 nm to the preferred NIR region.[52,81,94] The 6 order of magnitude larger extinction cross section of the antibody conjugated nanorose particles (10^{-14} m^2)[2] compared with antibody conjugated fluorophore, like indocyanine green dye or Cy5.5,[90,107,108] is highly desirable for NIR optical imaging and therapy in cancer.

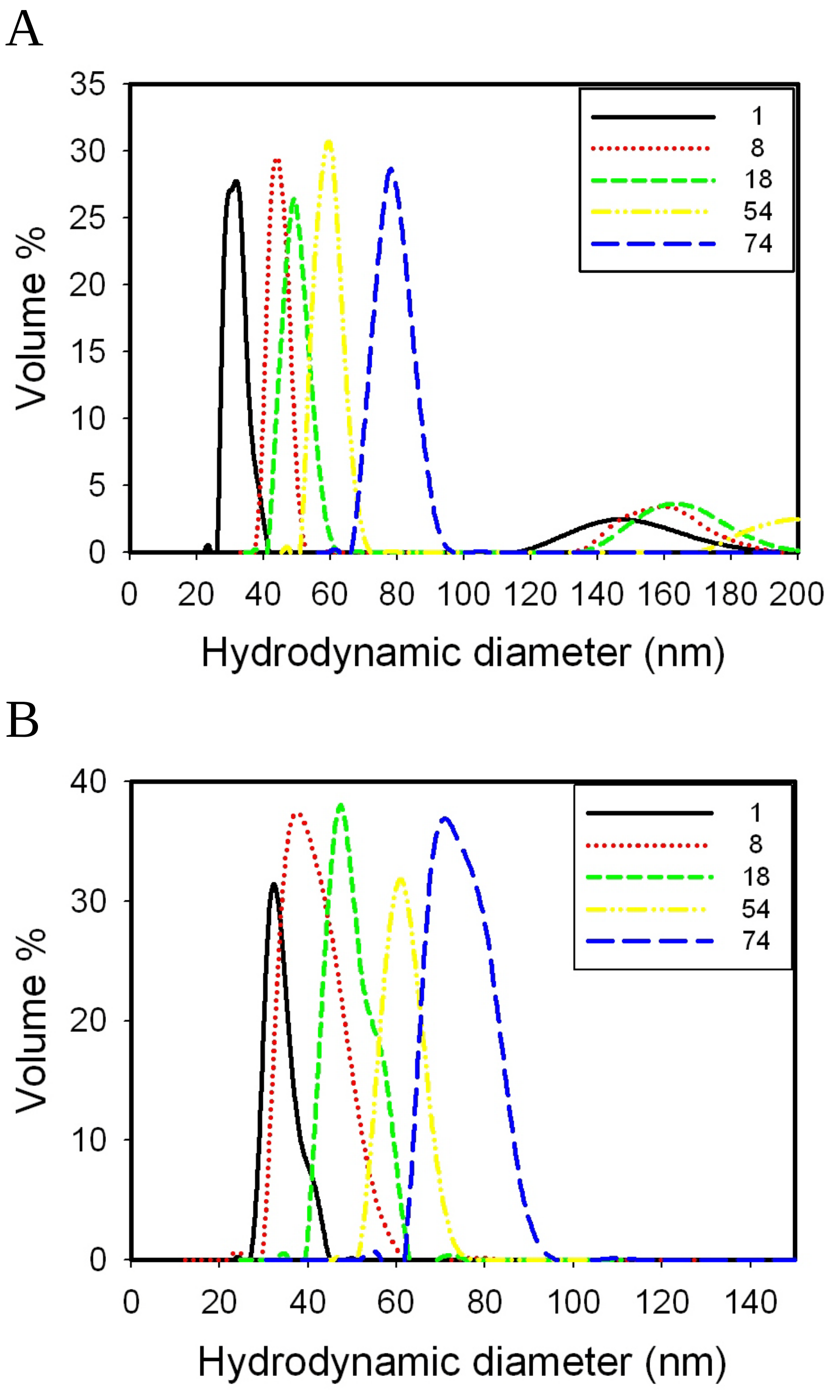

Figure A.2 Hydrodynamic diameter of clone 225 conjugated nanoroses. A. before filtration B. after passing a 0.22 µL filter. Insert gives numbers of Abs per particle.

Feed Ab mass (µg)	Feed Ab molecules/ nanorose	Conjugated Ab mass (µg)	Conjugated Ab molecules/ nanorose	Diameter volume %	Diameter after filtration
2.00	12	0.1800	1	33±3 nm, 92%	35±4 nm
9.98	60	1.2570	8	45±3 nm, 89%	44±6 nm
20.02	121	3.0030	18	51±4 nm, 87%	50±5 nm
50.18	303	8.9674	54	61±4 nm, 92%	63±5 nm
99.80	604	12.1990	74	80±5 nm, 91%	78±7nm

Table A.1. Clone 225 conjugation to 6.2×10^{11} nanorose particles and hydrodynamic diameter by dynamic light scattering.

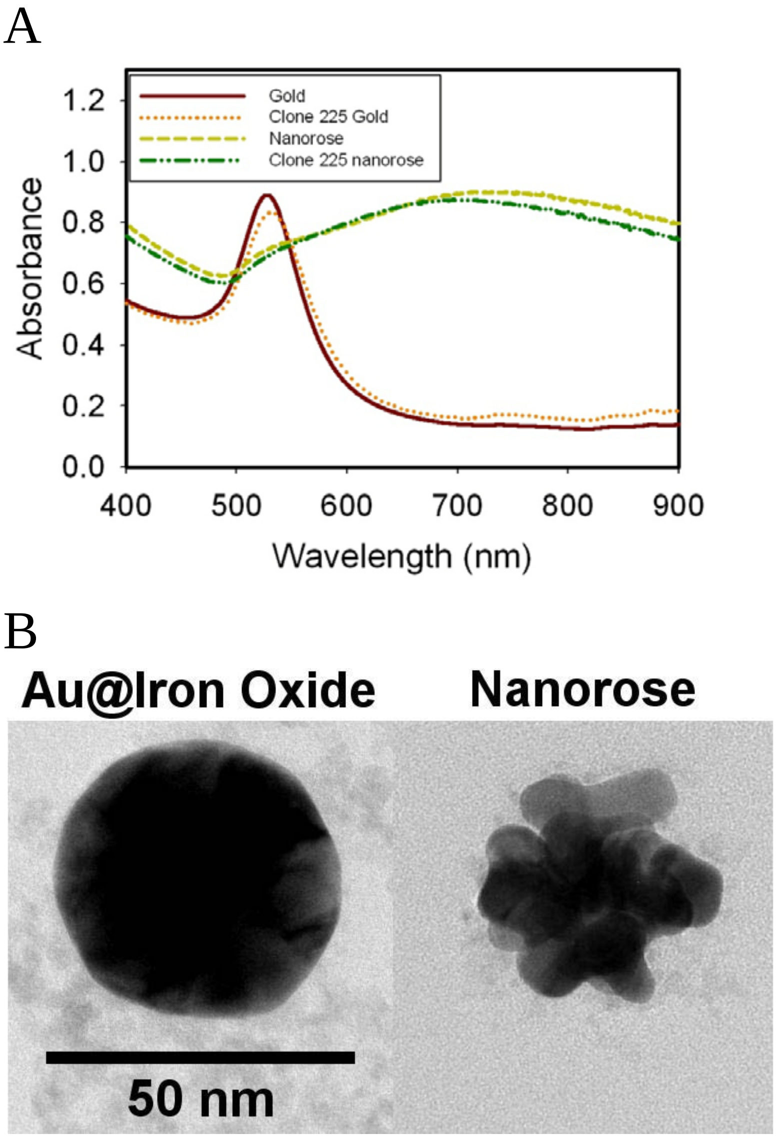

Figure A.3 Extinction spectra (A) and TEM images (B) of thick gold shell coated iron oxide nanoparticle (Au@Iron Oxide) and nanorose. All spectra were normalized for 16 µg Au/ml dispersion as quantified by AAS with 1 cm optical path length. TEM images were acquired before conjugation.

	Thick Au w/o Ab	Thick Au with Ab	Nanorose w/o Ab	Nanorose with Ab
Extinction coefficient ($cm^2/\mu g$ Au)	0.0085	0.0106	0.0563	0.0537

Table A.2. Measured Extinction Coefficient at 755 nm of Thick Gold Coated Iron Oxide Nanoparticles and Nanorose particles.

A.3.2 Selective cellular uptake with dosage response

Dark field microscopy images were used to compare the targeting selectivity of A431 cancer cells for the specific clone 225 conjugated nanoroses versus the non-specific anti-rabbit IgG (RG-16) conjugated nanoroses (Control). In each case, the experiments were performed with the sample containing 54 antibody molecules per nanorose, in which the coverage was on the order of a monolayer. Since empty cells scatter light much more weakly in the visible and NIR regions (400-900 nm) (Figure A.4A) relative to metal nanoparticles, the reflected light from the nanoparticles was much brighter than for the cells under dark field. The A431 cells harvested from one petri dish were divided equally and cultured with different dosage of nanorose particles. The images were acquired under the same microscope and camera settings. As shown in Figures 4A-C the non-specific anti-rabbit IgG conjugated nanoroses accumulate very little in the A431 cells, even with the highest dosage (4.0×10^5 RG-16 nanoroses/cell). On the contrary, an orange signal intensity appeared in the A431 cells treated with the specific clone 225 conjugated nanoparticles, even with a dosage of 1.0×10^4 clone 225 nanoroses/cell (Figure A.4D. Similar orange colors have been observed in macrophage cells incubated with non-specific dextran-coated nanorose without Abs.[2] The orange intensity increased monotonically with dosage. At the highest level tested (4.0×10^5 clone 225 nanoroses/cell), the intense reflectance signal was at the limit of detector.

The nanorose particle cell uptake was quantified by AAS elemental analysis by averaging over 10^5 to 10^6 A431 cells treated with different particle dosages. Figure A.5 shows the cell uptake increased from 10 to 609 particles per cell with increased dosage from 1.0×10^4 to 4.0×10^5 of anti-rabbit IgG conjugated nanoroses. The cell uptake for clone 225 conjugated nanoroses increased from 543 to 7175 particles per cell under the same dosage range. A factor of 54× higher cell uptake was achieved for clone 225 conjugated nanoroses versus control under lowest dosage and a factor of 12× higher versus control under highest dosage. The cell uptake reached a maximum value of ~7000 particles per cell at the dosage of 4.0×10^5 nanoroses/cell for clone 225 conjugated nanoroses.

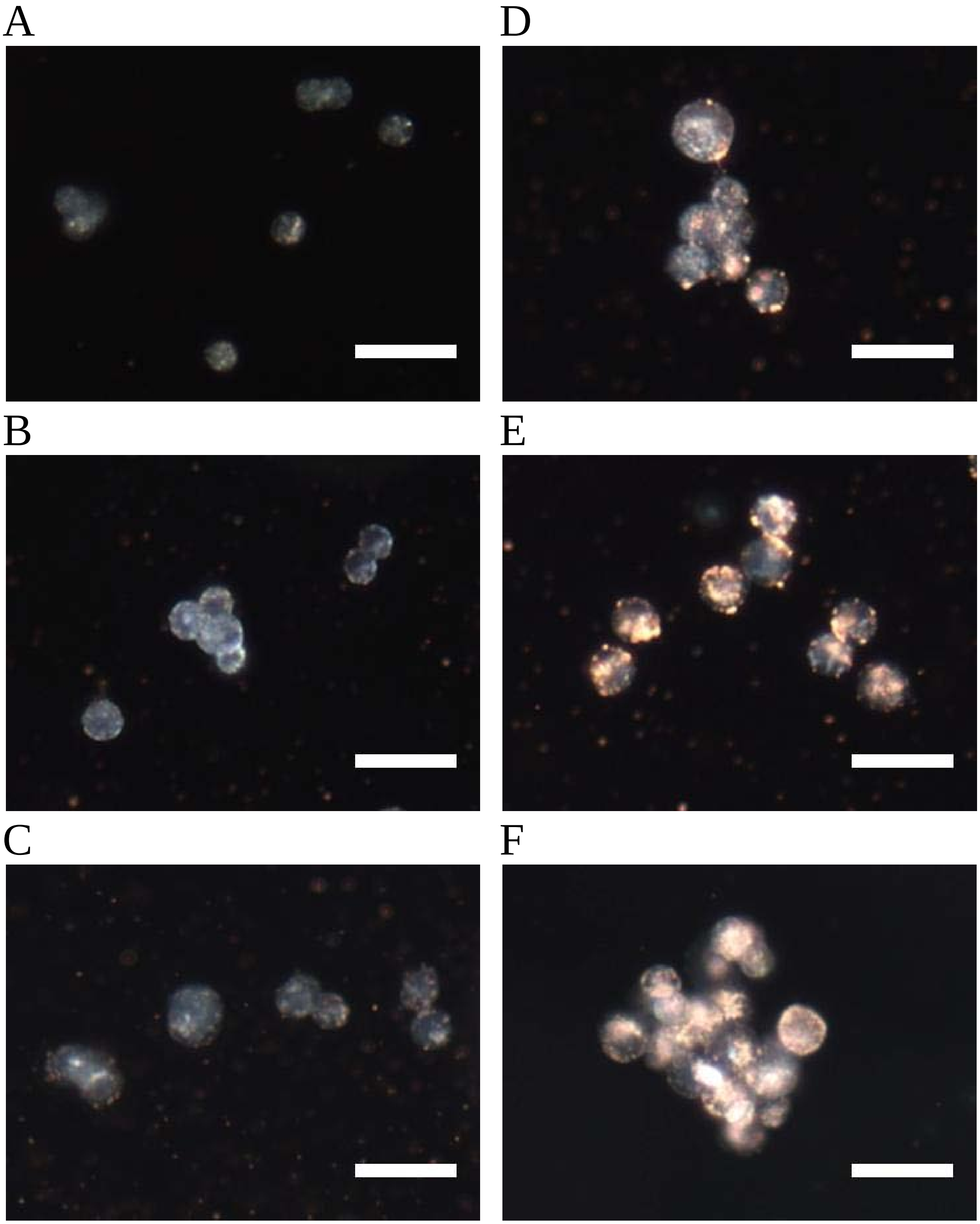
A
D
B
E
C
F

Figure A.4 Dark field microscopy images of A431 cells treated with different dosages of clone 225 conjugated nanoroses (right column) relative to control experiments using anti-rabbit IgG (clone RG-16) conjugated nanoroses (left column) under the same experimental conditions. A, B and C represent typical images with dosages of 0, 5.0×10^4 and 4.0×10^5 RG-16 nanoroses/cell. D, E and F represent typical images with dosage of 1.0×10^4, 5.0×10^4, 4.0×10^5 nanoroses/cell. Scale bar is 25 μm.

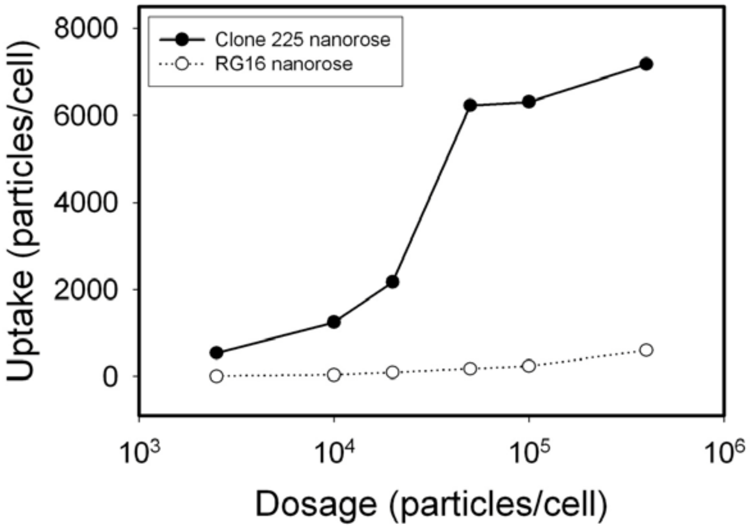

Figure A.5 Cell uptake of clone 225 and RG-16 conjugated nanoroses. 10^5 to 10^6 A431 cells were incubated with 2.5×10^3, 1.0×10^4, 2.0×10^4, 5.0×10^4, 1.0×10^5, 4.0×10^5 nanoroses/cell for 1 hr.

A.3.3 Low cell uptake in EGFR(-) control cancer cells

To demonstrate the EGFR targeting specificity of clone 225 conjugated nanorose particles to EGFR (+) A431 cancer cells, negative control EGFR (-) MDA-MB-435 breast cancer cells were cultured and labeled under the same conditions. For both dextran coated nanoroses (2.0×10^4 nanoroses/cell) without Abs and clone 225 conjugated nanoroses (2.0×10^4 or 4.0×10^5 nanoroses/cell), dark field microscopy images show very little orange reflective intensity in these EGFR (-) MDA-MB-435 cells (Figure A.6) compared with the as EGFR (+) A431 cells (Figure A.4 DEF). Thus, nonspecific endocytosis of the clone 225 conjugated nanorose particles to non-EGFR over-expressing cells was very limited. Therefore, the specific interactions of these nanoparticles with the receptors on the EGFR (+) A431 cancer cells were required for the large uptake.

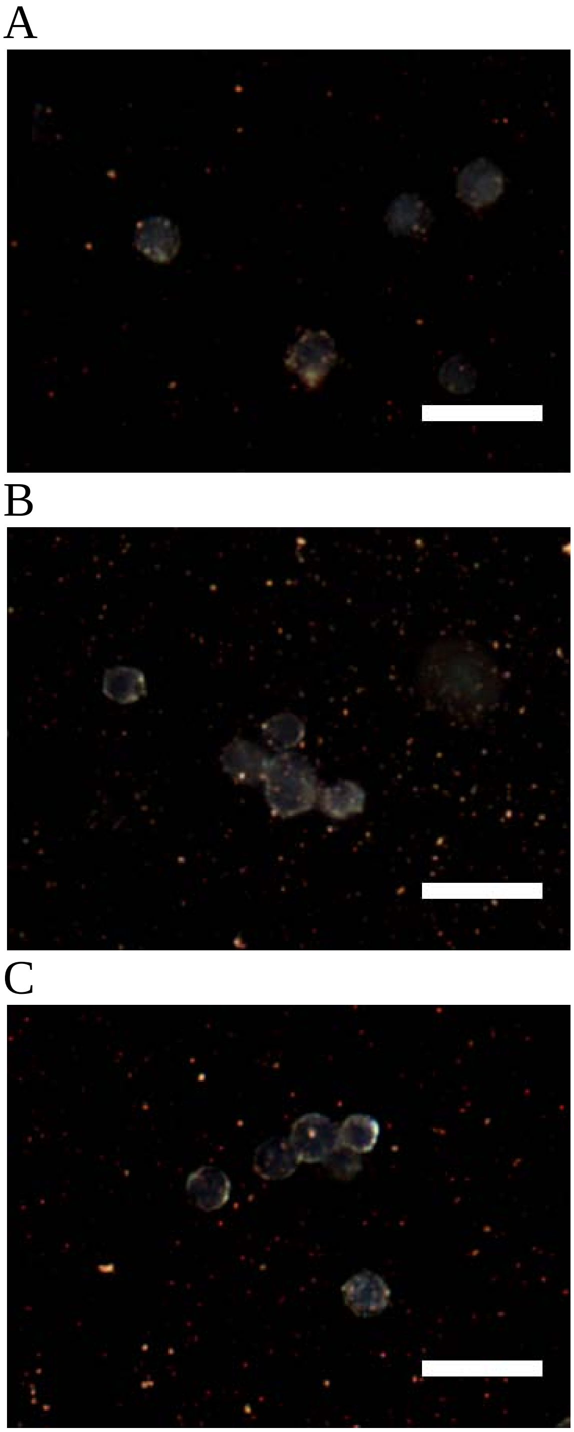
A
B
C

Figure A.6 Dark field microscopy images of EGFR negative control MDA-MB-435 cells treated with clone 225 conjugated nanoroses for 1 hr. A, 2.0×10^4 unconjugated nanoroses/cell (control); B, 2.0×10^4 particles/cell; C, 4.0×10^5 particles/cell. Scale bar is 25 μm.

A.3.4 NIR and fluorescent dual mode imaging of clone 225 conjugated nanorose targeted to A431 cancer cells

Not only was the Alexa Fluor 488 label used to quantify the average number of conjugated antibodies per nanorose particle, but it was also be used for simultaneous fluorescence imaging (right column in Figure A.7) with dark field reflectance imaging (left column). Image D0 shows very weak auto-reflectance signal without nanoparticles under dark field mode as has been shown in Figure A.4A. Upon viewing under fluorescence mode simultaneously (F0, Figure A.7) with an excitation light source at 490 nm, a signal was not present at the detection wavelength (520 nm), indicating lack of autofluorescence of the cells. With 5.0×10^4 nanoroses/cell, image D1 shows a strong reflectance signal in NIR region (as seen in Figure A.4E). The fluorescence image F1 shows no signal indicating no fluorescence emission without Alexa Fluor 488 labels. Image D2 and F2 were acquired with Alexa Fluor 488 labeled clone 225 nanorose at the same dosage. D2 shows a similar imaging contrast and orange signal intensity as D1, suggesting the reflectance intensity under dark field mode is not affected by changing particle surface coating with fluorophore. A green fluorescent signal emitted from Alexa Fluor 488 was observed in image F2, localizing the cell profiles in the same location as shown in D2. Upon observing the images more carefully, a wide range of intensities is present in D2 showing high contrast for various degrees of aggregation of nanoparticles. Less contrast in intensity is evident in the fluorescence images. Dual mode Images were also obtained for nanoparticles with only 18 antibodies per nanorose at the same dosage

(5.0×10^4 nanoroses/cell) in D3 and F3. Similar signal intensities were observed as in D2 and F2, indicating the targeting efficacy did not drop off significantly with a reduction in the number of Abs per particle. Again, higher contrast in intensity was in dark field imaging than by fluorescence (D3).

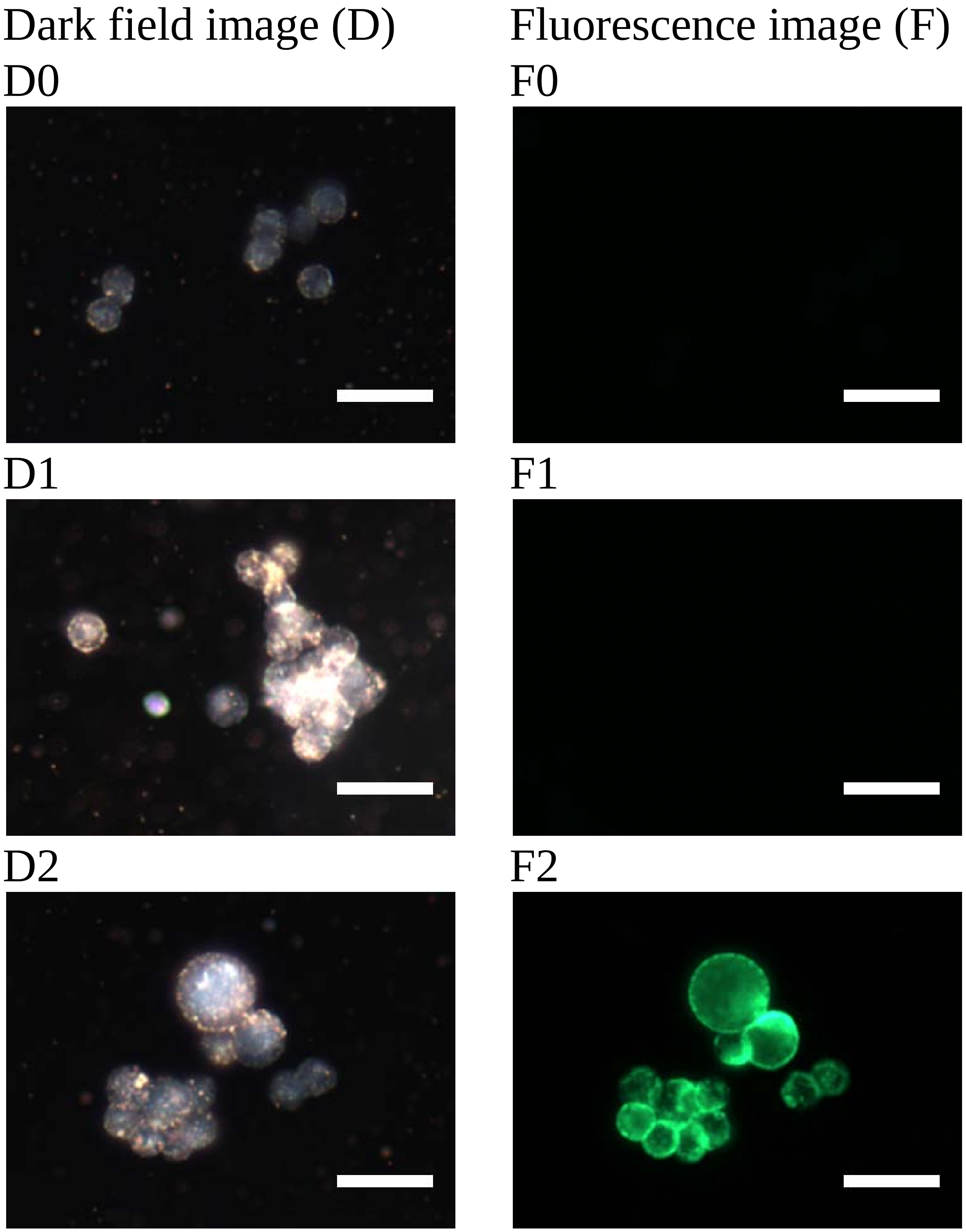
Dark field image (D)
Fluorescence image (F)
D0
F0
D1
F1
D2
F2

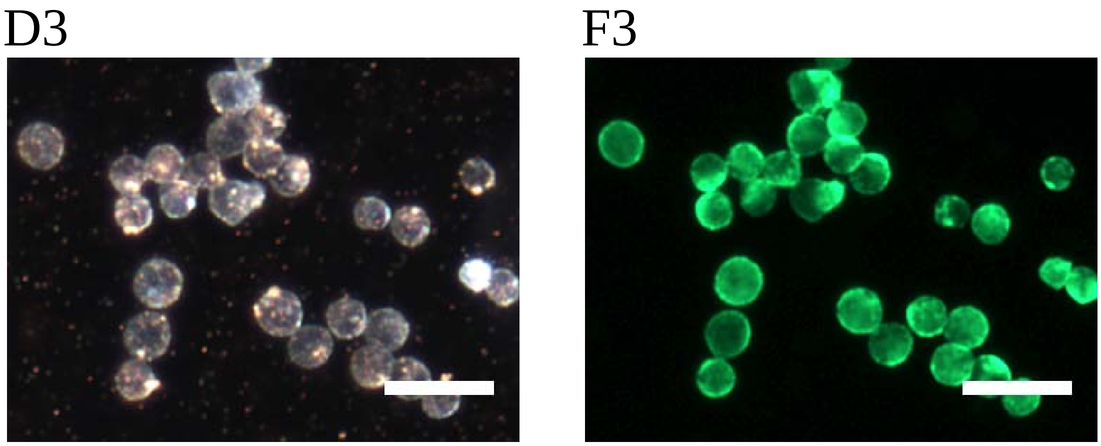

Figure A.7 Dark field (D) and fluorescent (F) microscopic images of A431 cells incubated with clone 225 conjugated nanoroses for 1 hour. 0, cells without nanoparticles as control; 1, 54 antibodies per nanorose without fluorescent label; 2, Same as (1) with AlexaFluor 488 label; 3, same as (2) with 18 antibodies per nanorose. A particle dosage of 5.0×10^4 nanoroses/cell applied to 1-3 experiments. Scale bar is 25 µm.

A.4 DISCUSSION

A.4.1 Packing of optical and magnetic functionality, along with antibody linker and antibody in a small overall particle size

The design of a nanoparticle with a high degree of functionality and antibodies conjugated to the surface requires highly efficient use of space. This challenge can become severe as the particle diameter becomes smaller than 100 nm. The mass ratio of the various components in conjugated nanoparticles was estimated from AAS and the number of conjugated Ab, as shown in Table A.S1 (Supporting Information). Typical mass ratios were 3.20 % for an Ab monolayer, 27.69 % for Fe cores and 69.21 % for the Au coating. For nanorose with thin Au coatings, the final Au/Fe mass ratio of 2.5 was much smaller than values of 10 for previously reported particles with spherical thick Au shells (~20 nm shell thickness).[94] Au was still the predominant component in the particle by volume, illustrating the importance of designing very thin Au shells (< 5 nm) to reserve a large amount of space for additional functionality and Abs.

For nanorose particles, the unusually thin Au shells were synthesized by tuning the separation of the nucleation of the Au seeds on the iron oxide surface from the autocatalytic growth on the seeds.[109] To drive nucleation of Au seeds on unfavorable low energy iron oxide surfaces, high supersaturation values have often been generated by utilization of Au^{3+}/Fe mass ratios on the order of 10.[94-96] Consequently, as the seeds were nucleated, competitive autocatalytic growth of Au on Au often produced Au shells with thickness larger than 10 nm. Recently[109] and in the current study, extremely low Au^{3+} supersaturation values were applied to prevent excessive autocatalytic growth. The Au^{3+} addition profiles were varied during the reaction via a number of successive iterations to control the fraction of iron oxide substrate particles that were seeded.

In optical imaging and phototherapy applications, the Au shells on magnetic cores are often too thick to shift the surface plasmon resonance (SPR) peak to the preferred NIR region (Figure A.3A).[52,81,94] For nanorose particles, the thin Au shells with high degrees of asymmetry shifted the SPR to the NIR, with an extinction coefficient at 755 nm five times higher than for 50 nm spherical thick Au shells on iron oxide (Figure A.3 and Table A.2), despite the overall small diameter of 35 nm. Related types of asymmetry have been demonstrated for Au nanorod,[28] nanocage,[110] nanorice,[111] nanoegg (asymmetric egg white shell),[112] and smooth Au shell with faceted or tetracubic core.[26] These asymmetries alter the interactions between plasmon modes and shift the SPR peak of gold nanospheres from 530 nm for symmetric systems to the NIR.[24,26,111,112] In addition to nanorose, Au nanocages are also extremely small and exhibit strong NIR absorbance as a result of the morphology.[101]

Gold has a high Hamaker constant, and thus polymer steric stabilizers are often required to prevent van der Waals attraction between Au coated nanoparticles. For example, a 10 nm polymer (HS-PEG-COOH, MW 5kDa) shell was necessary to prevent colloid aggregation for 60 nm Au nanoparticles in buffered saline, prior to conjugation of targeting agents.[78] For indirect conjugation of Abs to functional groups on polymeric coatings on Au surfaces, a sufficient amount of polymer is needed to provide the required number of conjugation sites. For the low MW bifunctional linker on Abs in the present study, the length of linker is negligible, and the density of conjugation sites (Au atoms) is extremely high. For nanorose, only thin polymer coatings are needed for steric stabilization given weaker attraction for the thin Au shells, with a polymer loading of only 12 wt%, as shown recently.[2] The weak van der Waals forces for nanorose particles with thin Au shells and high porosity reduce the attraction forces between particles, and thus allow for very thin layers of steric stabilizers. Thus, a total thickness of only ~14 nm (Table A.1) for a monolayer of Abs with low MW polymer stabilizers (mPEG-SH, MW 5kDa) was achieved on the 35 nm thin Au coated iron oxide nanoparticles. The unusually small volume of the thin Au shells in nanorose is highly beneficial for providing space for other types of functionality, in this case, magnetic functionality and an Ab monolayer.

Table A.3. Occupied surface area per Ab on nanorose and Au sphere

	Nanorose	Au sphere
Diameter (nm)	35	18
Conjugated Abs/particle	54	9
Occupied surface area/Ab (nm^2)	71.2	113.0

A.4.2 Packing of antibodies on the highly curved nanorose surface

The number of antibodies for formation of a monolayer was calculated from two simple geometric models to evaluate the measured surface coverage. The Fc region binds to the Au surface, while the Fab chains extend outward and occupy more surface area, as shown in Figure A.8. Thus we choose to define an effective radius R from the center of the nanoparticle to the Fab region. In our case, a nanoparticle diameter of 35 nm and an antibody length of 11.7 nm give R = 29.2 nm.[113] In the first model, the area of the Fab region was assumed to be circular with a diameter of 16.9 nm (Figure A.8). For an individual antibody, half of the end-to-end length 16.9 nm for the two Fab chains gives a radius of r=8.45 nm.[113] Therefore, one Ab will occupy a circular area of 224 nm^2 on the surface of the particle at R. For a 2D monolayer of circles on a flat surface, where is the hexagonal close packed density (0.9069), the number of Abs

$$N_{\text{Abs}} = \frac{\text{Surface Area of Effective Sphere}}{\text{Area Occupied by Individual Antibody}} = \frac{4\pi R^2}{\pi r^2/\varepsilon}$$

Thus, a total of 43 antibodies per particle is calculated for a monolayer of close packed antibodies, assuming the native structure is maintained in the non-aggregated state.

In the second geometric model, the area of the Fab region is assumed to be a rectangle with length L=16.9 nm and width W= 4 nm[113]. In this case, the surface area per antibody (W·L) is 67.6 nm^2, such that $N_{\text{Abs}} = 4\pi R^2/(W\cdot L) = 144$. As is expected, the number of Abs is larger for rectangles that pack more efficiently on the surface. On the basis of the circular cross-section geometric model, the particle (Table A.1) was covered by approximately one monolayer with 54 Abs. The effective experimental area was 71.2 nm^2/Ab. The hydrodynamic diameter of 63 nm was close to the value of 58.4 nm predicted from R for a monolayer. The change of total hydrodynamic diameter with N_{Abs} may be attributed to a hybridization between the longer Ab chain length of 11.7 nm[113] and the shorter mPEG-SH (M_W 5,000) end-to-end chain length of 3.3 nm[114] (Scheme A.1). Thus for N_{Abs} values of 8 and 18, the hydrodynamic diameter fell between 35 nm and 63 nm for a monolayer. For the case with 74 Abs, N_{Abs} is above the monolayer value. The additional Abs beyond a monolayer is more likely to cause denaturation and aggregation from intermolecular interactions.[115,116] The aggregation may even trigger an immune response and decrease the targeting efficacy.[113]

In a recent study using clone 225, the same conjugation protocol and characterization methods were used for 18 nm spherical Au substrate particles. [83,84] In this case, 9 Abs were conjugated to each Au sphere. This corresponding area/Ab was 113.0 nm^2, somewhat larger than the value of 71.2 nm^2 for nanorose. Compared with the Au spheres with a radius of 9 nm, the radius of the protuberances (~ 5 nm, Figure A.3B) on the surface of nanorose led to a higher actual surface area, than the surface area of a sphere with an equivalent radius of 17.5 nm. The surface roughness raised the Ab packing capacity by ~ 1.6 times. Furthermore, the varying orientations of the Abs as a result of surface roughness may further allow for higher Ab densities.

High surface coverage of Abs is also favored by the high density of conjugation sites supplied by Au atoms on the nanorose surface and the low cross sectional area of the linker. In our case, the area of the short bifunctional linker with a MW 708.97 is very small. Only the steric repulsion from Abs appeared to limit the binding capacity as shown in our monolayer calculation. In contrast, an intermediate MW linker (HS-PEG-COOH, MW 5kDa) has been used for conjugation on Au nanospheres.[78] In this study N_{Abs} was not reported. For the indirect conjugation method, intermediate or high MW polymers are first used to stabilize the nanoparticle. Here the fraction of conjugation sites on the polymer coating can be well below unity, unlike the case for pure Au atoms in the direct method. The resulting decrease in the number of binding sites, as well as increase of the steric repulsion between the coating polymer chains, may lower the N_{Abs}/particle. Therefore, the high density of atomic Au binding sites on nanorose for low MW linkers were beneficial for achieving a full monolayer coverage in the present study.

Another direct conjugation method is to adsorb the antibody to Au, but without the formation of covalent bonds, as has been demonstrated with Herceptin (MW 145 kDa). For 40 nm Au spheres, up to 200 protein molecules can be absorbed , which would correspond to 33 nm^2 per protein.[92] This high Ab density suggests multilayer absorption. Without covalent bonding of the Ab, it may be more difficult to control the Ab orientation than for conjugation with thiol-based bifunctional linkers.

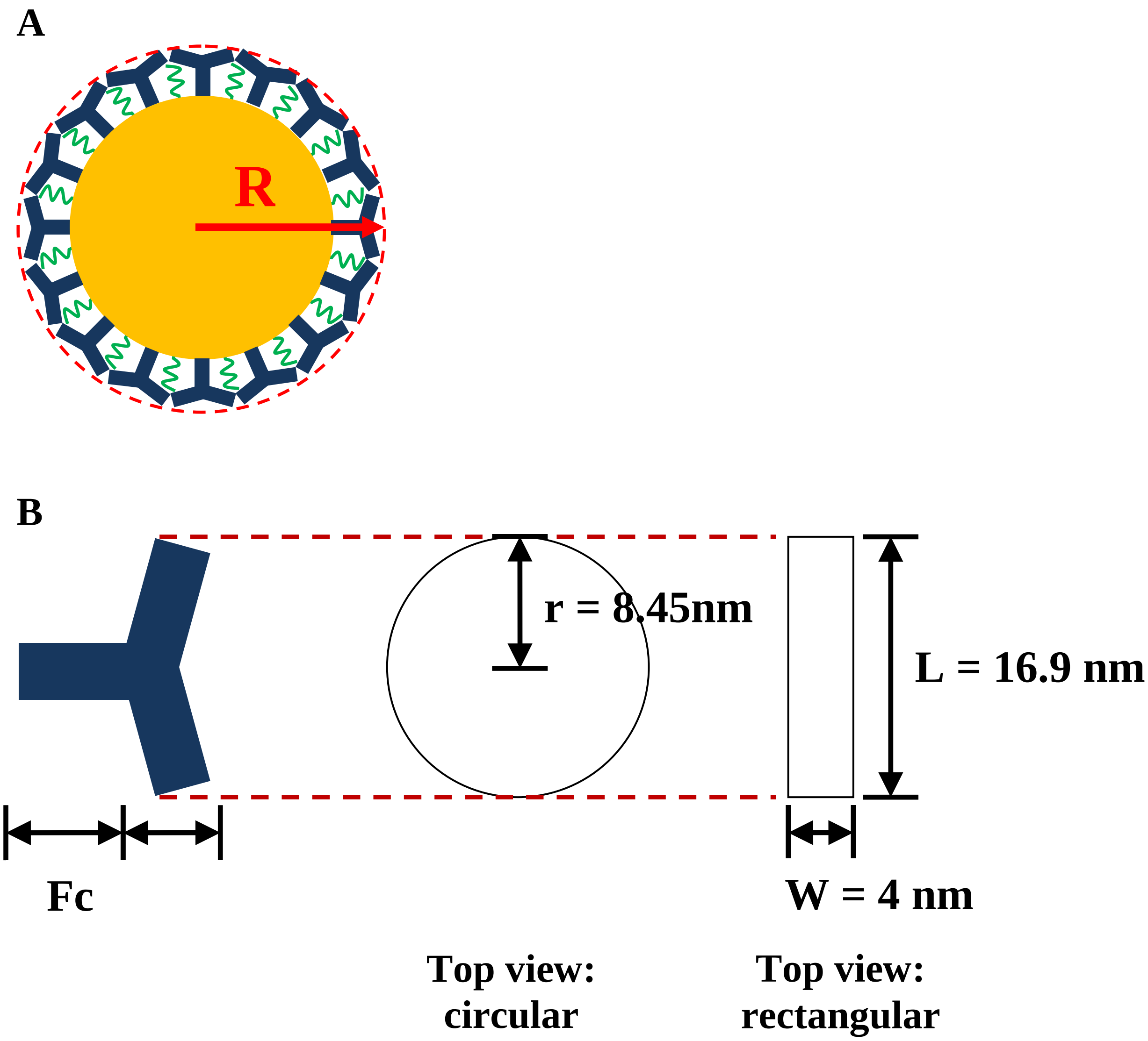

Figure A.8 **A,** The surface area of the particle is determined based on the nanoparticle and antibody assembly, having R = 29.2 nm. **B,** The area occupied per antibody is calculated using a circular, unaggregated model as well as a rectangular, close packed aggregated model. The radius of the circular model, r, is the length of a Fab chain, 8.45 nm. The length of the rectangular model, L, is the length of two Fab chains, 16.9 nm. The width of the rectangular model, W, is the width of a Fab chain, 4 nm.

A.4.3 Effects of particle size, curvature and shape on selective targeting

Studies have shown EGFR is over-expressed in human cancer cells and play a role in promoting tumor cell proliferation, invasion and metastasis.[117] Therefore, EGFR has been identified as molecular target for cancers.[90,118] Clone 225 (Cetuximab, Erbitux)[89,119] is a human-mouse chimeric anti-EGFR antibody that binds to the extracellular domain of EGFR with high affinity, and prevents activation of the receptor-mediated cellular survival signal. Therefore, clone 225 conjugated nanoparticles may be used to monitor the targeted delivery of the inhibitors and supply real time therapeutic effects during the treatment of tumor.

For nanorose conjugated with a monolayer of clone 225, a sigmoidal curve of cell uptake versus dosage was observed in Figure A.5. A high value of ~7,000 nanorose particles per cell was achieved at a dosage of 4.0×10^5 nanoroses/cell, producing a saturated signal for NIR reflectance. For a cell approximated as a 10 μm diameter sphere, this cell uptake corresponds to a 0.030 % packing fraction by volume. For clone 225 coated 50 nm Au nanospheres conjugated by the same protocol, a maximum uptake of 1,160 particle per cell (A431) was obtained at a much higher dosage level of 1.0×10^6 nanospheres/cell.[105] The resulting 0.015 % packing fraction was only half of the value for the nanorose. The higher cancer cell uptake by Ab conjugated nanorose at a lower dosage may be influenced by the smaller overall hydrodynamic diameter, the higher Ab density on the surface, and by the orientation of the Abs with respect to each other, which is influenced by high local surface curvature.

When hydrodynamic diameters of Ab coated Au nanospheres are reduced to less than 70 nm, the biological pathways in targeted cells can undergo profound changes.[92,120-123] The nanoparticles serve not merely as substrates for the Abs but strongly influence the effect of the Abs on the biological signaling processes. The fact that the curvature of the Au nanospheres influence binding capacities by nearly 3 orders of magnitude[92] suggests that interactions between multiple Abs on the surface and cell receptors play a key role. However, studies of the effect of curvature are relatively new, and it is not yet known how these effects will vary for different particle shapes, Abs, polymer stabilizers and cell types. For example, shape effects were much smaller for targeting of breast cancer cells (SK-BR-3) in a recent study of nanocages and nanospheres with anti-HER2 on the surface.[101] Anti-HER2 indirect conjugation to 33 nm nanocages through relatively low MW succinimidyl propionyl PEG disulfide (MW 5kDa) gave an uptake of 500 per cell. In this study, N_{Abs} was not reported. However, the small size of the particles and the shape of the nanocage are beneficial for controlling the degree of conjugation and Ab orientation for high uptake. A related example is the highly effective cell targeting of the tyrosine kinase receptors on Jurkat T cells for DNA aptamer conjugated to viral capsid nanoclusters.[124]

The knobby shape of the Au shells on the nanorose particles offers a rich domain of local surface curvatures that would be difficult to achieve for simpler shapes. The curvature of the protuberances (~ 5 nm, Figure A.3B) on the surface of nanorose particle is similar to that of the protein spheres that make up viral capsids[124]. The multiple number of gold domains of varying curvature for nanoclusters with convex surfaces (Fig. 3) will offer widespread opportunity for varying spacings and orientations of Abs with respect to the receptors on cell surfaces, and thus, ultimately, the therapeutic efficiency. In the current study, only a single nanocluster morphology is considered. However, a homologous series in the sizes and shapes of the Au shells has been accomplished by the mechanism of thin autocatalytic growth on nanoparticles substrates.[109] The thickness of the shells and the local surface curvatures may be adjusted independently.

Not only do the nanorose offer control over surface curvature, but also strong NIR absorbance, despite their small size. In a previous approach, NIR absorbance of Au nanoparticles is achieved upon EGFR-mediated aggregation inside cells.[12,52,105] The individual nanoparticles do not absorb in the NIR. Thus, the change in absorbance may be used to identify cancer markers. For the colloidally stable nanorose, the individual particles absorb strongly in the NIR, and provide vivid orange color under dark field microscopy (Figure A.4). This could be an advantage in cases where cellular uptake of Au nanoparticles doesn't bring the particles closely enough together for NIR absorbance.

A.5 CONCLUSIONS

Multifunctional nanoparticles composed of thin Au coatings on magnetic iron oxide cores, were conjugated with a monolayer of anti-EGFR monoclonal antibodies (clone 225). The number of Abs, as determined from the fluorophore tag, was tuned from 1 to 74 by varying the feed Ab/particle ratio. The respective hydrodynamic diameters, from 35 to 78 nm, were extremely small given the high degree of functionality. The highly asymmetric thin Au shells, synthesized by seeded growth on iron oxide nanoclusters at ultralow supersaturations of Au precursor, produce the strong NIR absorbance. The final Au/Fe mass ratio of 2.5 is smaller than previously reported values on the order of 10.[94] The unusually small volume of the Au is highly beneficial for providing space for other types of functionality, such as targeting and therapeutic Abs, and if desired, magnetic functionality. High surface coverage of Abs is favored by the high density of conjugation sites supplied by Au atoms on the surface and the low cross sectional area of the heterobifunctional dithiol-PEG-hydrazide (MW 708.97) linker. In contrast with this direct conjugation method, in the indirect method the MW of polymeric linkers is often higher and with a lower density of binding sites, resulting in lower Ab coverage. For 54 Abs, the hydrodynamic diameter indicated coverage of a monolayer for Abs, in agreement with the prediction of a geometric model, by assuming a circular area for the Fab region. Steric stabilization was provided with a combination of Ab as well as mPEG-SH in physiological media, to overcome the VDW attraction.

For the 63 nm particles with 54 Abs in a monolayer, targeting of EGFR overexpressive cancer cells was highly selective, relative to EGFR negative cancer cells. In dark field microscopy, high uptake of the conjugated nanoparticles produced an intense orange signal, resulting from strong NIR scattering. The cellular uptake of nanoparticles/cell of ~7,000, as characterized by AAS, was ~6 fold higher than previously reported for 50 nm Au spheres with the same Ab and cell type.[105] Intense NIR scattering was achieved from both high uptake of nanoparticles in cells and high NIR absorbance/mass Au, as observed in a previous study of the non-conjugated nanoparticles in macrophage cells by hyperspectral microscopy.[2] Colocalization of the NIR scattering and fluorescence indicates the Abs remained attached to the Au surfaces inside the cancer cells. The extremely high curvature of the Au shells with features below 5 nm influence the spacing and orientations of the Abs on the surface, resulting in the high cell uptake. Ultimately, tuning of surface curvature has the potential to have a marked effect on biological pathways within cells.[92,102-104] The ability to load intense multifunctionality, specifically strong NIR absorbance, conjugation of an Ab monolayer and strong r2 MRI contrast (from previous study[2]) in a total particle size only 63 nm, is an important step forward in achieving both molecular specific imaging and real time feedback on therapeutic efficacy for treatment of cancer.

A.6 SUPPORTING INFORMATION

Table A.S1. Component of Abs conjugated nanorose particles

Conjugated Ab molecules/ nanorose	Au w/w %	Fe w/w %	Ab w/w %
1	71.38268	28.55307	0.064286
8	71.10934	28.44374	0.448929
18	70.67063	28.26825	1.0725
54	69.21196	27.68478	3.202643
74	68.4465	27.3786	4.356786

A.7 REFERENCES

(1) Sokolov, K.; Follen, M.; Aaron, J.; Pavlova, I.; Malpica, A.; Lotan, R.; Richards-Kortum, R. *Cancer Research* **2003**, *63*, 1999.

(2) Gopalan, B.; Ito, I.; Branch, C. D.; Stephens, C.; Roth, J. A.; Ramesh, R. *Technol Cancer Res T* **2004**, *3*, 647.

(3) Loo, C.; Lowery, A.; Halas, N. J.; West, J.; Drezek, R. *Nano Letters* **2005**, *5*, 709.

(4) Huang, X.; El-Sayed, I. H.; Qian, W.; El-Sayed, M. A. *Journal of the American Chemical Society* **2006**, *128*, 2115.

(5) Dames, P.; Gleich, B.; Flemmer, A.; Hajek, K.; Seidl, N.; Wiekhorst, F.; Eberbeck, D.; Bittmann, I.; Bergemann, C.; Weyh, T.; Trahms, L.; Rosenecker, J.; Rudolph, C. *Nature Nanotechnology* **2007**, *2*, 495.

(6) Bagalkot, V.; Zhang, L.; Levy-Nissenbaum, E.; Jon, S.; Kantoff, P. W.; Langer, R.; Farokhzad, O. C. *Nano Letters* **2007**, *7*, 3065.

(7) Ma, L. L.; Feldman, M. D.; Tam, J. M.; Paranjape, A. S.; Cheruku, K. K.; Larson, T. A.; Tam, J. O.; Ingram, D. R.; Paramita, V.; Villard, J. W.; Jenkins, J. T.; Wang, T.; Clarke, G. D.; Asmis, R.; Sokolov, K.; Chandrasekar, B.; Milner, T. E.; Johnston, K. P. *Acs Nano* **2009**, *3*, 2686.

(8) Hirsch, L. R.; Stafford, R. J.; Bankson, J. A.; Sershen, S. R.; Rivera, B.; Price, R. E.; Hazle, J. D.; Halas, N. J.; West, J. L. *Proc. Natl. Acad. Sci. U. S. A.* **2003**, *100*, 13549.

(9) Shah, J.; Park, S.; Aglyamov, S.; Larson, T.; Ma, L.; Sokolov, K.; Johnston, K.; Milner, T.; Emelianov Stanislav, Y. *Journal of biomedical optics* **2008**, *13*, 034024.

(10) Ferrari, M. *Nat Rev Cancer* **2005**, *5*, 161.

(11) Maeda, H.; Fang, J.; Inutsuka, T.; Kitamoto, Y. *Int Immunopharmacol* **2003**, *3*, 319.

(12) Matsumura, Y.; Maeda, H. *Cancer Res.* **1986**, *46*, 6387.

(13) Qian, X. M.; Peng, X. H.; Ansari, D. O.; Yin-Goen, Q.; Chen, G. Z.; Shin, D. M.; Yang, L.; Young, A. N.; Wang, M. D.; Nie, S. M. *Nat. Biotechnol.* **2008**, *26*, 83.

(14) Wang, S. P.; Mamedova, N.; Kotov, N. A.; Chen, W.; Studer, J. *Nano Letters* **2002**, *2*, 817.

(15) Huang, X.; Peng, X.; Wang, Y.; Shin, D. M.; El-Sayed, M. A.; Nie, S. *Acs Nano* **2010**.

(16) Larson, T. A.; Bankson, J.; Aaron, J.; Sokolov, K. *Nanotechnology* **2007**, *18*, 325101/1.

(17) Aaron, J. S.; Oh, J.; Larson, T. A.; Kumar, S.; Milner, T. E.; Sokolov, K. V. *Optics Express* **2006**, *14*, 12930.

(18) Aaron, J.; Nitin, N.; Travis, K.; Kumar, S.; Collier, T.; Park, S. Y.; Jose-Yacaman, M.; Coghlan, L.; Follen, M.; Richards-Kortum, R.; Sokolov, K. *Journal of Biomedical Optics* **2007**, *12*, 034007/1.

(19) Kumar, S.; Harrison, N.; Richards-Kortum, R.; Sokolov, K. *Nano Letters* **2007**, *7*, 1338.

(20) Kumar, S.; Aaron, J.; Sokolov, K. *Nat Protoc* **2008**, *3*, 314.

(21) Aaron, J.; Travis, K.; Harrison, N.; Sokolov, K. *Nano Letters* **2009**, *9*, 3612.

(22) Brillhart, K. L.; Ngo, T. T. *J Immunol Methods* **1991**, *144*, 19.

(23) Oshannessy, D. J.; Dobersen, M. J.; Quarles, R. H. *Immunol Lett* **1984**, *8*, 273.

(24) Ghose, T. I.; Blair, A. H.; Kulkarni, P. N. *Method Enzymol* **1983**, *93*, 280.

(25) Goldstein, N. I.; Prewett, M.; Zuklys, K.; Rockwell, P.; Mendelsohn, J. *Clin. Cancer Res.* **1995**, *1*, 1311.

(26) Ke, S.; Wen, X. X.; Gurfinkel, M.; Charnsangavej, C.; Wallace, S.; Sevick-Muraca, E. M.; Li, C. *Cancer Res.* **2003**, *63*, 7870.

(27) Farokhzad, O. C.; Langer, R. *Advanced Drug Delivery Reviews* **2006**, *58*, 1456.

(28) Jiang, W.; Kim, B. Y. S.; Rutka, J. T.; Chan, W. C. W. *Nature Nanotechnology* **2008**, *3*, 145.

(29) Nie, S. M. *Nanomedicine* **2010**, *5*, 523.

(30) Lyon, J. L.; Fleming, D. A.; Stone, M. B.; Schiffer, P.; Williams, M. E. *Nano Letters* **2004**, *4*, 719.

(31) Park, H.-Y.; Schadt, M. J.; Wang, L.; Lim, I. I. S.; Njoki, P. N.; Kim, S. H.; Jang, M.-Y.; Luo, J.; Zhong, C.-J. *Langmuir* **2007**, *23*, 9050.

(32) Xu, Z.; Hou, Y.; Sun, S. *Journal of the American Chemical Society* **2007**, *129*, 8698.

(33) Levin, C. S.; Hofmann, C.; Ali, T. A.; Kelly, A. T.; Morosan, E.; Nordlander, P.; Whitmire, K. H.; Halas, N. J. *ACS Nano* **2009**, *3*, 1379.

(34) Rasch, M. R.; Sokolov, K. V.; Korgel, B. A. *Langmuir* **2009**, *25*, 11777.

(35) Goon, I. Y.; Lai, L. M. H.; Lim, M.; Munroe, P.; Gooding, J. J.; Amal, R. *Chemistry of Materials* **2009**, *21*, 673.

(36) Lim, J.; Tilton, R. D.; Eggeman, A.; Majetich, S. A. *Journal of Magnetism and Magnetic Materials* **2007**, *311*, 78.

(37) Lim, J. K.; Majetich, S. A.; Tilton, R. D. *Langmuir* **2009**, *25*, 13384.

(38) Cho, E. C.; Au, L.; Zhang, Q.; Xia, Y. *Small* **2010**, *6*, 517.

(39) Decuzzi, P.; Pasqualini, R.; Arap, W.; Ferrari, M. *Pharm. Res.* **2009**, *26*, 235.

(40) Gratton, S. E. A.; Ropp, P. A.; Pohlhaus, P. D.; Luft, J. C.; Madden, V. J.; Napier, M. E.; DeSimone, J. M. *Proceedings of the National Academy of Sciences of the United States of America* **2008**, *105*, 11613.

(41) Champion, J. A.; Katare, Y. K.; Mitragotri, S. *Proceedings of the National Academy of Sciences of the United States of America* **2007**, *104*, 11901.

(42) Mallidi, S.; Larson, T.; Tam, J.; Joshi, P. P.; Karpiouk, A.; Sokolov, K.; Emelianov, S. *Nano Letters* **2009**, *9*, 2825.

(43) Kumar, S.; Aaron, J.; Sokolov, K. V. *Nature Protocols* **2008**, *3*, 314.

(44) Ryoo, W.; Webber, S. E.; Johnston, K. P. *Industrial & Engineering Chemistry Research* **2003**, *42*, 6348.

(45) Urbanska, K.; Romanowska-Dixon, B.; Matuszak, Z.; Oszajca, J.; Nowak-Sliwinska, P.; Stochel, G. *Acta Biochimica Polonica* **2002**, *49*, 387.

(46) Josephson, L.; Kircher, M. F.; Mahmood, U.; Tang, Y.; Weissleder, R. *Bioconjugate Chemistry* **2002**, *13*, 554.

(47) Ma, L. L.; Borwankar, A.; Willsey, B.; Yoon, K. Y.; Tam, J. O.; Sokolov, K.; Feldman, M. D.; Milner, T. E.; Johnston, K. P. *Prepare for Submitting* **2011**.

(48) Xia, Y.; Xiong, Y. J.; Lim, B.; Skrabalak, S. E. *Angew Chem Int Edit* **2009**, *48*, 60.

(49) Wang, H.; Brandl, D. W.; Le, F.; Nordlander, P.; Halas, N. J. *Nano Letters* **2006**, *6*, 827.

(50) Knight, M. W.; Halas, N. J. *New Journal of Physics* **2008**, *10*.

(51) Hu, Y.; Noelck, S. J.; Drezek, R. A. *Acs Nano* **2010**, *4*, 1521.

(52) Pease, L. F.; Elliott, J. T.; Tsai, D. H.; Zachariah, M. R.; Tarlov, M. J. *Biotechnol Bioeng* **2008**, *101*, 1214.

(53) Fetters, L. J.; Lohse, D. J.; Richter, D.; Witten, T. A.; Zirkel, A. *Macromolecules* **1994**, *27*, 4639.

(54) Wang, W. *Int J Pharm* **2005**, *289*, 1.

(55) Gupta, P.; Hall, C. K.; Voegler, A. C. *Protein Sci* **1998**, *7*, 2642.

(56) Onn, A.; Correa, A. M.; Gilcrease, M.; Isobe, T.; Massarelli, E.; Bucana, C. D.; O'Reilly, M. S.; Hong, W. K.; Fidler, I. J.; Putnam, J. B.; Herbst, R. S. *Clin. Cancer Res.* **2004**, *10*, 136.

(57) Baselga, J.; Arteaga, C. L. *J Clin Oncol* **2005**, *23*, 2445.

(58) Robinson, D. R.; Wu, Y. M.; Lin, S. F. *Oncogene* **2000**, *19*, 5548.

(59) Ferrari, M. *Nature Nanotechnology* **2008**, *3*, 131.

(60) Reddy, S. T.; Swartz, M. A.; Hubbell, J. A. *Trends in Immunology* **2006**, *27*, 573.

(61) Wang, A. Z.; Bagalkot, V.; Vasilliou, C. C.; Gu, F.; Alexis, F.; Zhang, L.; Shaikh, M.; Yuet, K.; Cima, M. J.; Langer, R.; Kantoff, P. W.; Bander, N. H.; Jon, S.; Farokhzad, O. C. *ChemMedChem* **2008**, *3*, 1311.

(62) Weissleder, R. *Science* **2006**, *312*, 1168.

(63) Tong, G. J.; Hsiao, S. C.; Carrico, Z. M.; Francis, M. B. *Journal of the American Chemical Society* **2009**, *131*, 11174.

(64) Tam, J. M.; Tam, J. O.; Murthy, A.; Ingram, D. R.; Ma, L. L.; Travis, K.; Johnston, K. P.; Sokolov, K. V. *ACS Nano* **2010**, *4*, 2178.

Appendix B: Growth of Textured Thin Au Shells on Iron Oxide Nanoparticles

A general mechanism is presented for thin autocatalytic growth on nanoparticle substrates (TAGS) as demonstrated for a homologous series of < 5 nm textured Au coatings on 42 nm iron oxide cores. Very low Au precursor supersaturation levels are utilized to prevent commonly encountered thick shells due to excessive autocatalytic growth. This approach extends the mechanism of seeded autocatalytic growth for the formation of pure metal nanoparticles to heterogeneous growth on a low energy substrate. The degree of separation of nucleation to form the seeds from growth is utilized to control the morphology and uniformity of the unusually thin Au coatings. The thin shells with high degrees of asymmetry shift the surface plasmon resonance (SPR) to the NIR, with large extinction coefficients, even for particles with total hydrodynamic diameters less than 60 nm. TAGS may be generalized to a wide variety of substrates and high energy coatings to form core-shell nanoparticles of interest in a broad range of applications including catalysis and bionanotechnology.

B.1 INTRODUCTION

Small nanoparticles (<100 nm) with a thin metal coating on a low surface energy metal oxide core are of interest in numerous applications including imaging contrast agents in nanomedicine,[1,2] catalysis and electrocatalyis[3,125] and sensors.[4,5] For optical imaging and therapy in nanomedicine, the Au shells on magnetic cores are often too thick to shift the absorbance to the preferred near infrared (NIR) region.[52,81,94] Pure Au nanparticles (and other metals) are commonly synthesized by autocatalytic growth on Au seeds nucleated from soluble precursors[59,126] or on pre-existing seeds.[57,127,128] Fine control of the size as well as low polydispersities may often be achieved by separating the nucleation from the growth stages.[60,69,110,129,130] In contrast, controlled growth of high surface energy Au shells on lower energy metal oxide cores is much less favorable; furthermore the lattice spacings are mismatched.[99,110,131-134] To drive nucleation of Au seeds on unfavorable low energy iron oxide surfaces, high supersaturation values are often generated by utilization of Au^{3+}/Fe mass ratios on the order of 10.[94-96] Consequently, as the seeds are being nucleated, competitive autocatalytic growth of Au on Au often produces Au shells with thickness often larger than 10 nm.

The growth of a Au shell on an iron oxide core may be partially passivated with dynamic low molecular weight ligands, for example, citrate or thiols.[94-96,135,136] The ligands must not inhibit too strongly the nucleation of the Au seeds, and simultaneously, must provide steric or electrostatic stabilization. A judicious balance of these factors has been accomplished to produce thin Au coatings on small iron oxide cores (<10 nm).[95,96,137] However, this approach has received little attention for larger cores (20-60 nm) where polymer steric stabilizers are required to counteract attractive VDW forces between the particles.[2,97] For a uniform shell on a 45 nm Fe_3O_4 spherical core, a shell thickness of 2.5 nm would require a Au/Fe ratio of 5:1 assuming 100% yield. Here, autocatalytic growth has been found to produce much thicker shells on a fraction of the iron oxide cores,[94] as further examined in this study. To date, reported Au coatings by direct growth of precursors on an iron oxide nanoparticle substrate range from 10 to 30 nm thick.[52,81,94,138]

An alternative is to deposit pre-made Au seeds as small as 2 nm on a nanoparticle substrate, and to fill in spaces between the seeds by reduction of Au precursors to form Au shells,[26,98,100,111,139] as first demonstrated on silica.[140] Whereas in principle, the shells could be only slightly larger than the seeds, excessive autocatalytic growth produces shells on the order of 10 nm.[26,97-100] Novel concepts would be beneficial for synthesizing thin metal shells, and designing the shell texture, given these complexities of poor wetting by Au and excessive autocatalytic growth.

Herein, a general mechanism is presented for thin autocatalytic growth of metals on nanoparticle substrates (TAGS), and utilized to grow thin Au coatings on 42 nm iron oxide cores. The TAGS mechanism is shown to be a general extension of the seeded autocatalytic growth mechanism for pure nanoparticles[57,127] to heterogeneous coatings on low energy substrate cores. The thickness and texture of the thin (< 5 nm) Au coatings are controlled by tuning the separation of the nucleation of the Au seeds on the iron oxide surface from the autocatalytic growth of the seeds. The Au coatings are either smooth (and relatively spherical) or characterized by knobby protrusions as shown for a series of morphologies in Scheme B.1. Extremely low Au^{3+}/Fe ratios of 0.125-0.50 are investigated to attempt to prevent excessive autocatalytic growth. These low supersaturation levels will also inhibit undesired nucleation of Au seeds in the bulk solution. The Au^{3+}/Fe profile is varied during the reaction via a number of successive iterations or continuous addition of Au^{3+} precursor. This profile is designed to control the fraction of iron oxide substrate particles that are seeded with Au. After reaction, the Au coated particles are separated by centrifugation from relatively naked (uncoated) iron oxide nanoclusters. Thiol terminated methoxy-polyethylene glycol (mPEG-SH, M_w = 20,000) is used for steric stabilization on the Au surfaces,[141] while simultaneously providing sufficient passivation of Au growth without too strongly inhibiting nucleation of Au seeds. The thiol group does not bind to iron oxide, which could otherwise interfere with the nucleation of Au seeds on its surface. The nanoparticles are characterized by TEM and DLS to determine the morphology and hydrodynamic diameter, and by atomic absorbance spectrometry to determine the Au/Fe mass ratio. Based on these results, it appears that the TAGS mechanism may be generalized in the future to form thin coatings on a wide range of low energy nanoparticle substrates with low precursor/substrate feed ratio, well controlled supersaturation profile and a polymeric stabilizer.

A secondary objective is to relate the surface plasmon resonance (SPR) of the nanoparticles to the asymmetries in the shell geometry. These asymmetries alter the interactions between plasmon modes and red-shift the SPR peak from 530 nm for symmetric systems, such as very thick uniform shells, to the NIR.[24,26,111,112] For a peak maximum of 700 nm, according to Mie theory, $R_{total}/ R_{core} < 1.25$ is required for a Au shell on a spherical Fe_3O_4 core with a permittivity of ~ 6.[142-144] Thus, for cores on the order of 40 nm, the shells would have to be thinner than 5 nm, as reported in this study. Such thin shells have rarely been achieved previously.[2] Further asymmetry in geometry results from the non-spherical shape of the nanocluster core for the coated nanoparticles with either smooth (non-knobby) or knobby surfaces (Scheme B.1). Related types of asymmetry have been demonstrated for Au rods,[28] nanocages,[110] nanorice,[111] nanoeggs (asymmetric egg white shells),[112] and smooth particles with faceted or tetracubic cores.[26] The high degree of magnetic and functionality and thin metal shell on relatively small nanoparticles would be desirable for optical,[54,145] magnetic or multimodal imaging and therapy[146,147] with effective permeation of biological barriers.[2,92,120]

B.2 EXPERIMENTAL SECTION

B.2.1 Materials

All reagents used were analytical grade. Ferrous chloride, ammonium hydroxide, hydroxylamine hydrochloride and sodium hydroxide were purchased from Fisher Chemicals (Fairlawn, NJ), ferric chloride from Acros Organics (Morris Plains, NJ), and citric acid from EM Science (Gibbstown, NJ). Tetrachloroauric acid trihydrate ($HAuCl_4$

·$3H_2O$) was purchased from MP Biomedicals LLC. (Solon, OH) and mPEG-SH (MW 20,000) from Nanocs Inc. (New York, NY).

B.2.2 Kinetics of Nucleation and Growth of Au on Iron Oxide

Iron oxide nanoclusters coated with citrate were synthesized by hydrolysis of iron chlorides by modification of the method of Sahoo et al[148] as described in the supplementary section. The iron oxide nanoclusters were dispersed in 100 ml of deionized (DI) water at a concentration of 0.1 mg Fe/ml with rigorous stirring. 300 µL ammonium hydroxide (7 %) was added to adjust the pH to 9.3. 2.0 ml of 1 % (w/v) hydroxylamine hydrochloride was added as the reducing agent for the Au precursor along with 10 ml of 4 mg/ml mPEG-SH (PEG MW 20,000). 1 ml of the solution was transferred to a cuvette with a 1 cm path length, which was inserted into a Cary Varian 3E UV-Vis spectrophotometer. To start the reaction, the desired amount of Au chloride solution (2.5 mg Au/ml) was injected into the cuvette, and the absorbance of the solution at 755 nm was measured at intervals of 0.0016 seconds for 5 minutes. After the absorbance reached a plateau, the absorbance spectrum was measured between 400 and 850 nm.

B.2.3 Coating Au on Iron Oxide Nanoclusters with Addition of Precursor in Iterations or Continuously

The exact above procedure was carried out in a 200 ml beaker with rigorous stirring. The $HAuCl_4$ solution (2.5 mg Au/ml) was divided equally into multiple aliquots for sequential iterations. Each iteration was separated by a 5 minute interval. After the last iteration, the stirred solution was allowed to stand for 30 min for mPEG-SH reaction with the Au surfaces. The reaction products were centrifuged at 6,000 rpm for 6 min. The supernatant was decanted and the precipitate were re-dispersed in a dilute mPEG-SH solution (0.2 mg/ml) and bath sonicated for 5 minutes to produce a stable colloidal suspension. For the continuous addition experiments, $HAuCl_4$ at a concentration of 0.5 mg Au/ml was added into the reaction mixture with a syringe pump at a rate of 0.1 ml/s.

B.2.4 Materials Characterization

Dynamic light scattering (DLS) measurements were performed in triplicate on a custom made Brookhaven Instruments ZetaPlus apparatus at a scattering angle of 90° and temperature of 25°C.[56] The concentrations of nanoparticle dispersions were adjusted with DI water to give a signal counting rate between 300-400 kcps. Prior to DLS measurements, the samples were bath sonicated for 2 minutes. The autocorrelation functions were analyzed with a non-negative least-squares (NNLS) method to determine distributions by volume.

Low resolution TEM was performed on a FEI Tecnai Spirit BioTwin at 80 kV accelerating voltage. High resolution TEM was performed on a field emission JEOL2010F at 200 kV accelerating voltage. A drop of the dispersion of particles after diluting it 40 times was put on a 400 mesh ultrathin carbon-coated copper TEM grid. Excess liquid was siphoned off using a tissue and the grid was allowed to dry in air.

The Au and iron oxide concentrations in the nanoparticle dispersions were obtained with a GBC 908AA flame atomic absorption spectrometer (GBC Scientific Equipment Pty Ltd) equipped with an air-acetylene flame furnace. The absorption of Au was recorded at 242.8 nm and iron at 248.3 nm. The instrument was calibrated using Au^{3+} or Fe^{3+} standard solutions before every set of measurements. All the measurements were carried on diluted samples so that the concentration of iron or Au in the diluted sample was between 1 and 5 µg/ml.

Thermogravimetric analysis (TGA) was performed using a Perkin–Elmer TGA 7 under nitrogen atmosphere at a gas flow rate of 20 ml/min. Nanoparticle samples were dried to powder in an oven at 100°C. Then samples were heated up to and held at 100°C in the TGA instrument for 20 minutes to remove any moisture. The samples were heated continuously from 100°C to 800 °C at a constant rate of 20 °C/min, and then held at 800°C for 30 minutes. Magnetization at 300 K was measured using a superconducting quantum interference device (SQUID) magnetometer (Quantum Design MPMS). The loss in mass due to adsorbed ligand from TGA was taken into account for normalization to the mass of iron oxide.

Scheme B.1 Gold coatings on iron oxide nanoclusters

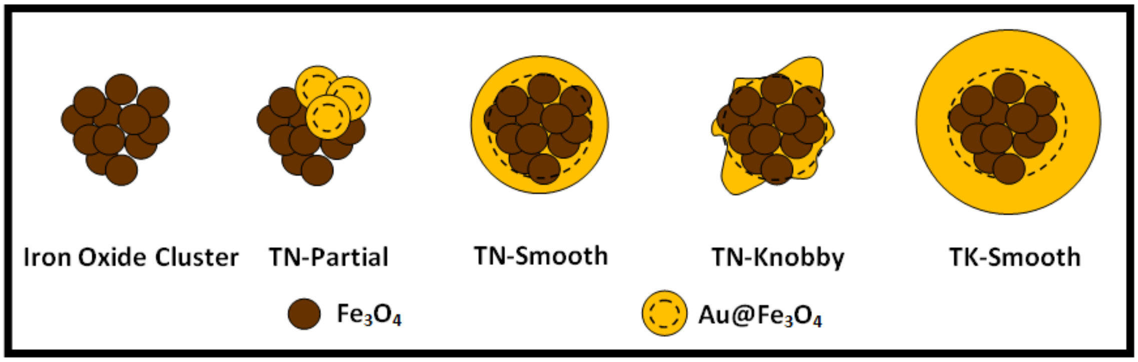

Scheme B.2 Nucleation and growth of Au shells on iron oxide substrates by adding precursor with different profiles

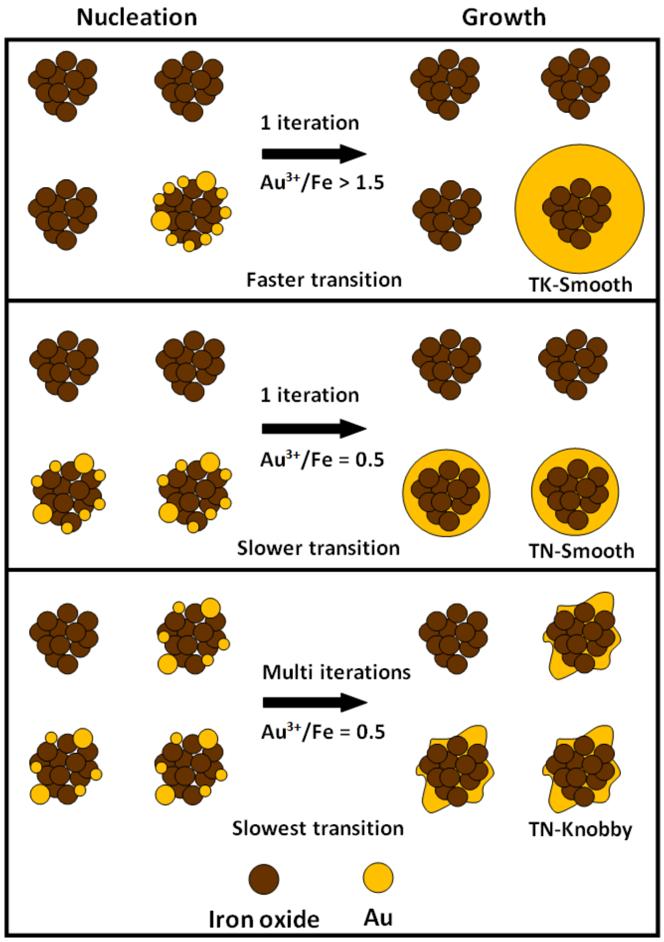

B.3 RESULTS

B.3.1 Au Nucleation and Growth Kinetics on Iron Oxide Substrates with a Single Iteration

The diameter of the starting citrate stabilized iron oxide nanoclusters without any added Au^{3+} was ~40 nm as shown by TEM in Figure B.1A and more definitively by the DLS in Figure B.2A. To coat the iron oxide cores, the feed Au^{3+}/Fe ratio was varied as shown in Figure B.1. The mPEG-SH was present in initial mixture for bonding to the growing Au surfaces. For a complete monolayer of mPEG-SH on a 50 nm diameter Au nanoparticle surface, the estimated mPEG-SH/Au mole ratio would be 0.006 (Supporting Information). Thus, a higher mPEG-SH/Au^{3+} feed mole ratio of 0.08 was chosen for all experiments. At the lowest Au^{3+}/Fe ratio, a few darker 10-15 nm domains of Au were present, as shown in Figure B.1B and Scheme B.1 for a thin partial coating (TN-Partial) on the lighter iron oxide substrate, a consequence of the higher electron density for Au. As the Au^{3+}/Fe ratio increased progressively to 1.5, the size of the particles with thick relatively smooth (with very small knobby protrusions) Au coatings increased reaching 80 nm (TK-Smooth, Scheme B.1).

The hydrodynamic diameters for the Au coated nanoclusters in the dispersion without centrifugation are shown in Figure B.2 and Table B.S1. For control experiments performed with iron oxide nanoparticles at the same mass concentration, low count rates of 5-20 kcps were observed, indicating very weak scattering of light from the 633 nm laser. After reaction, count rates were 400-500 kcps. Thus, the measured size distribution for a mixture of Au coated iron oxide nanoclusters in the presence of uncoated nanoclusters after reaction will be highly biased to the coated clusters, a beneficial result. The variance values for the hydrodynamic diameters were quite small (Figure B.2 and Table B.S1). The hydrodynamic diameters are in the same range as the diameters in the TEM images, although the numbers of particles in the TEM images were too small for statistically significant determination of particle size. According to both the TEM images and DLS, the shell thickness increases monotonically with the Au^{3+}/Fe ratio. At Au^{3+}/Fe of 0.125 (TN-Partial), the hydrodynamic diameter is only 2 nm larger than for the initial naked iron oxide clusters. This value of 2 nm is well below the 12 nm end-to-end chain length of mPEG-SH (MW 20,000).[114] Only a small fraction of the surface is covered with Au and thiol groups on the polymer bound to Au. As Au^{3+}/Fe ratio increased to 0.5 (TN-Smooth), the measured mean hydrodynamic diameter was 57 nm, indicating a 7.5 nm shell thickness composed of a thin Au shell bound with flexible mPEG-SH molecules. Here the Au covered a much larger fraction of the surface as also seen by TEM, and thus a much larger amount of polymer was adsorbed. Much larger particles were formed at higher Au^{3+}/Fe ratios, and the hydrodynamic diameter reached 159 at a Au^{3+}/Fe ratio of 6 (TK-Smooth). At this high ratio, 30 nm pure Au nanoparticles were also present, as shown in Figure B.2B by DLS.

The absorbance spectra of the Au coated nanoparticles were obtained by subtraction of the initial iron oxide specta given in Figure B.2C. At a Au^{3+}/Fe ratio of 0.125 (TN-Partial), a relatively broad absorbance is present in the visible and NIR regions from 500 to 850 nm, despite the extremely low amount of Au. For Au^{3+}/Fe ratios of 0.25-0.5 in Figure B.2C (TN-Smooth), the absorbance peak in the visible region increased to a greater extent than absorbance above a wavelength of 700 nm. For Au^{3+}/Fe ratios from 1 to 6, the SPR peaks were blue shifted as the shells became much thicker (TK-Smooth). SPR peak maxima on the order of 600 nm have been observed often for thick Au shells on iron oxide.[15,28,36,38,40,41]

To better understand the mechanism, the kinetics of Au nucleation and growth were monitored *in situ* by UV-Vis spectrometry at 755 nm. In Figure B.3A, the absorbance of Au on substrate for Au^{3+}/Fe mass ratio 0.125 -0.5 reached a plateau within the first 30 s. The height of the plateau increased with the Au^{3+}/Fe ratio suggesting a greater degree of nucleation and growth, consistent with thicker shells in Figure B.1. When Au^{3+}/Fe ratio was raised higher to 1.0 or 1.5, the kinetics became even faster and the plateau height further increased as shown in Figure B.3B. These results suggest that the large heterogeneous surface area of iron oxide was sufficient to achieve rapid nucleation. However, for Au^{3+}/Fe ratios of 3.0 and 6.0, the absorbance increased continuously for 5 min without reaching a plateau.

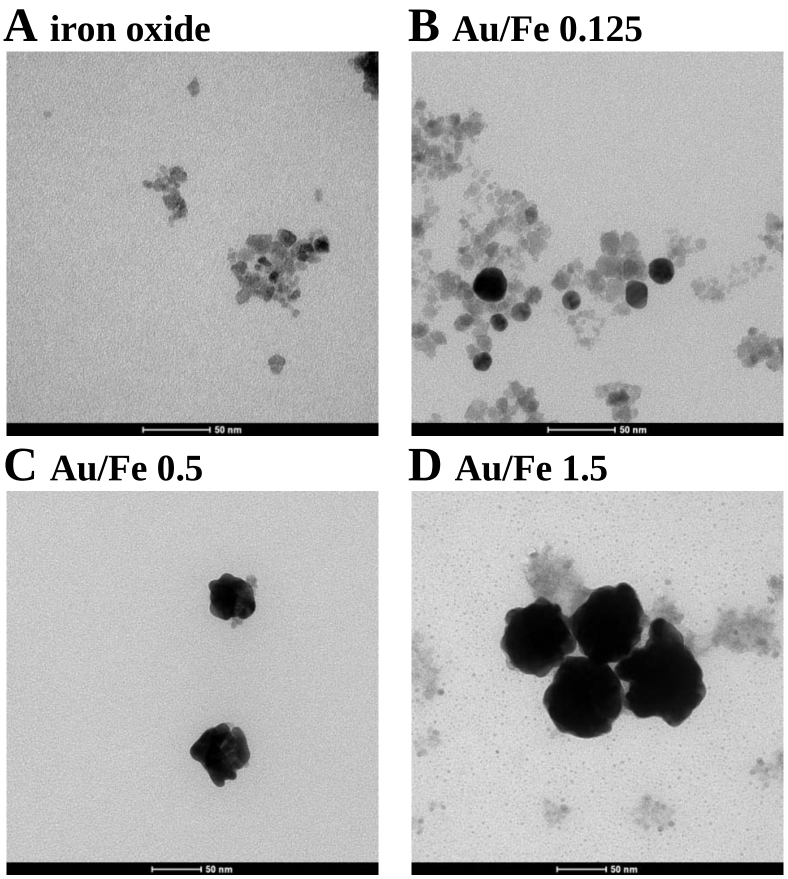
A iron oxide

B Au/Fe 0.125

C Au/Fe 0.5

D Au/Fe 1.5

Figure B.1 TEM images of gold on iron oxide made from Au/Fe mass ratio 0, 0.125, 0.5 and 1.5 with a single iteration.

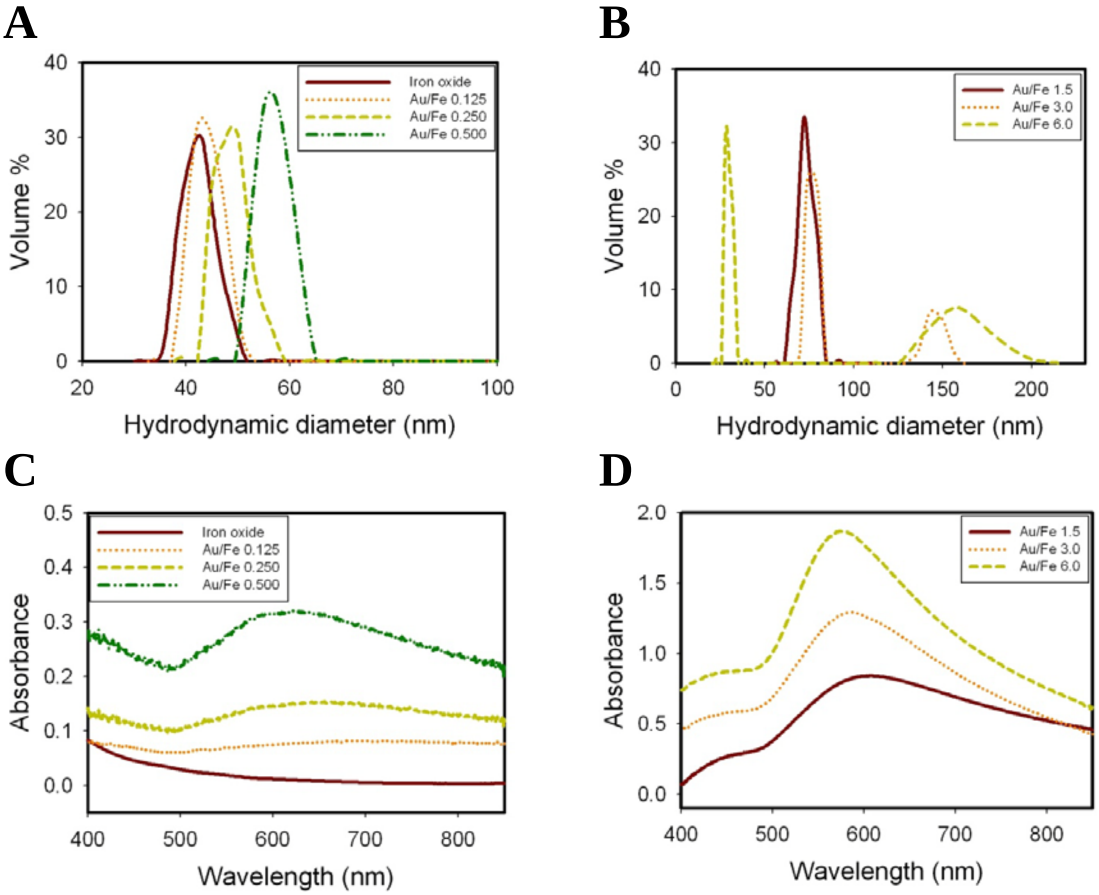

Figure B.2 Hydrodynamic diameters A, B and Equilibrium absorbance spectra C, D of synthesized gold coated iron oxide nanoparticle dispersion with a single iteration after iron oxide base line deduction without centrifugation.

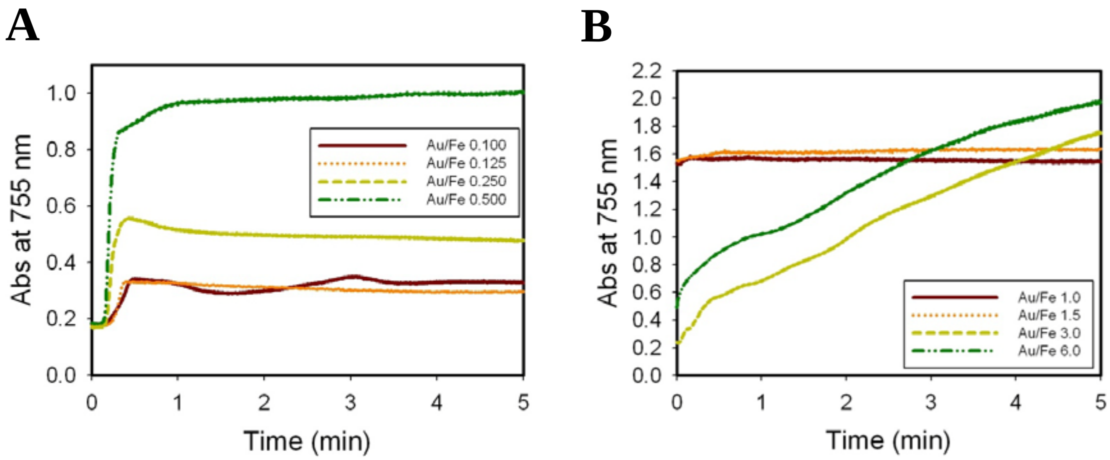

Figure B.3 Au nucleation and growth kinetics monitored by real absorbance of gold on iron oxide at 755 nm in situ for a single iteration. A, Low Au/Fe mass ratio 0.1 - 0.5; B, high Au/Fe 1.0 - 6.0.

B.3.2 Au Nucleation and Growth Kinetics on Iron Oxide Substrates with Multiple Iterations

The number of iterations of Au^{3+} precursor addition was varied for a total Au^{3+}/Fe ratio of 0.5 to control the morphology. A smooth, relatively round (TN-Smooth), Au coated particle texture is shown in Figure B.4A for a single iteration, similar to the TEM image in Figure B.1C. For 3 equal iterations, the coatings were thinner and with knobby protuberances on the surface of the clusters (Figure B.4B, TN-Knobby). This trend continued as the number of iterations increased from 3 to 5. According to DLS, the mean hydrodynamic diameters of Au coated iron oxide nanoparticles decreased from 61 nm to 57 nm as the number of iterations increased from 1 to 5 as shown in Figure B.5A and Table B.2. This decrease in size was also evident in the TEM images (Figure B.4). Furthermore, the Au/Fe ratio from AAS decreased by a factor of ~3 with this decrease in hydrodynamic diameter, and consequently, shell thickness (Table B.1).

To provide insight, a simple geometric model was used to estimate the thickness of a uniform shell on a 42 nm spherical iron oxide core (despite the actual nonspherical nanocluster geometry) from the mass values obtained by AAS (Supplemental information). The calculated Au shell thicknesses ranging from 0.75-2.0 nm (Table B.1) were below the thicknesses obtained by subtracting the core value of 42 nm from the hydrodynamic diameter (Table B.2), which ranged from 7.5-9.5 nm (Table B.2). This difference indicates an approximate thickness of the mPEG-SH layer, as well as uncertainty from the presence of uncoated iron oxide particles and the complex geometry.

The behavior of the SPR for the samples after centrifugation are shown in Figure B.5B. For one iteration, the absorbance spectrum was similar to that in Figure B.2C (which was not centrifuged), for the thin relatively round and smooth coating (TN-Smooth). However, for 3 or 5 iterations, the absorbance shifted progressively into the NIR region and became broader and flatter as the shell became thinner and the knobby protrusions became larger (TN-Knobby, Scheme B.1). To our knowledge, this type of morphology and spectra has been reported only once previously for so called nanoroses, however, only one type of reaction condition and particle was investigated.[2] The extinction coefficients per weight of gold at 755 nm were higher for these particles as we can see in Table B.1 and their value increased with an increase in the number of iterations.

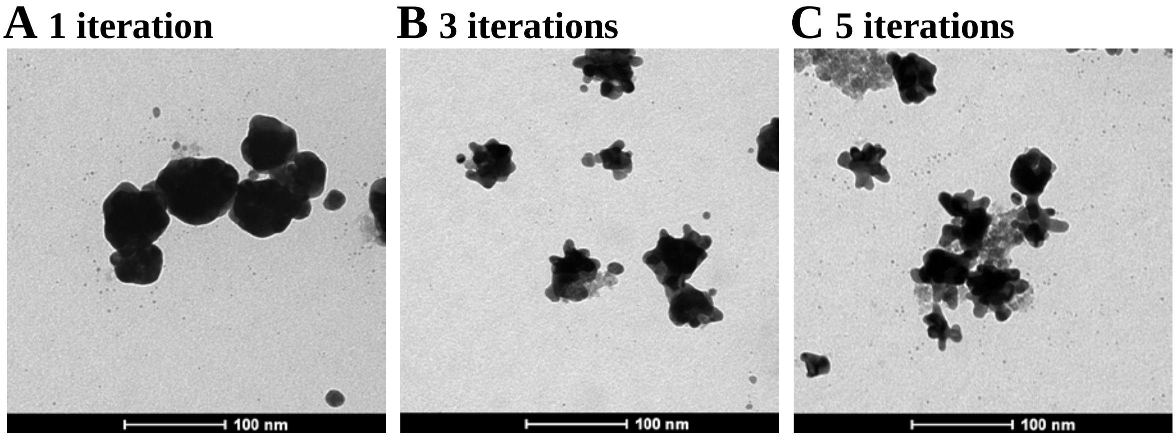
A 1 iteration **B** 3 iterations **C** 5 iterations

Figure B.4 TEM images of gold coated iron oxide nanoparticles made from a total Au/Fe mass ratio of 0.50 with varying numbers of iterations. All samples were prepared from reactant mixture after centrifugation separation at 6000 rpm for 6 mins.

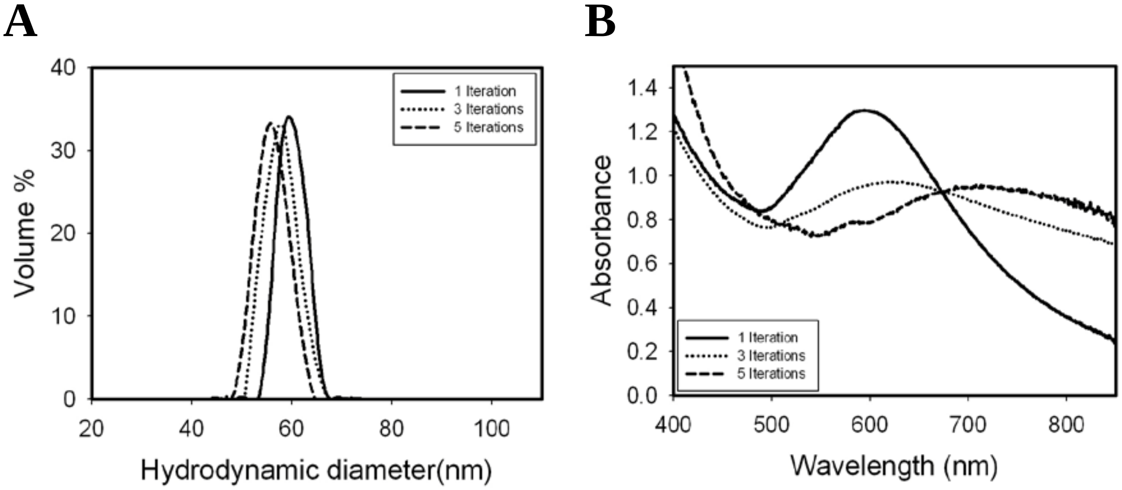

Figure B.5 The hydrodynamic diameters A and absorbance spectra B of gold coated iron oxide nanoparticles made from a total Au/Fe mass ratio of 0.50 with varying numbers of iterations.

Table B.1 Elemental analysis of gold coated iron oxide nanoparticles made from a total Au/Fe mass ratio of 0.50 with different iterations.

	Au/Fe	Au %	Fe %	Estimated total diameter (nm)	Extinction Coefficient ($cm^2/\mu g$ Au)
1 iteration	2.40	17.20	3.70	46.0	0.040
3 iteration	1.30	9.90	3.60	44.3	0.043
5 iteration	0.84	5.20	3.00	43.5	0.050

Table B.2 Mean Size and Standard Deviation of Textured Thin Gold Coated Iron Oxide Nanoparticles
Au/Fe=0.5, reached with different iterations

Au/Fe ratio	Mean (nm)	Variance (nm)	% Standard deviation
1 iteration	61	2.6	4.3
3 iterations	59	3.0	5.1
5 iterations	57	3.2	5.6

B.3.3 Au Nucleation and Growth Kinetics on Iron Oxide Substrates with Continuous Precursor Addition

The number of iterations was raised to infinity by adding the Au^{3+} precursor continuously to an iron oxide dispersion. Here Au chloride (0.5 mg Au^{3+}/ml) was injected with a syringe pump at a rate of 0.1 ml/s for 2 mins. For the uncoated iron oxide nanoclusters on the order of 40 nm, the primary particle size was 8 nm (Figure B.6A). For a total Au^{3+}/Fe ratio 0.5, high resolution TEM images (Figure B.6B and 6C) after centrifugation reveal lattice fringes from Au and Fe_3O_4 crystalline domains. The lattice spacing of 0.244 nm in the interior of the cluster from an 8 nm primary spherical particle indicated the (3 1 1) plane of Fe_3O_4 in Figure B.6C, which is quite different from any other Fe_3O_4 or Au lattice planes. Two Au crystalline facets for the (1 1 1) and (2 0 0) orientations correspond to 0.236 nm and 0.204 nm d-spacings, respectively for Au. These

Au shells on the exterior of the cluster are only a few nm thick and are highly curved, as a consequence of the curvature of the surfaces of the iron oxide primary particles in the core.

The total feed Au^{3+}/Fe ratio was varied to attempt to manipulate the thickness and shape of the Au shells, as shown in the TEM images in Figure B.7. At an Au^{3+}/Fe ratio of 0.125, a few spherical 12-15 nm darker spots are evident on the lighter iron oxide nanoclusters in Figure B.7A and 7D (TN-Partial), indicating an extremely thin Au coating. In addition, extremely small 1 nm Au particles, which may be considered Au embryos or seeds may be observed on the surface of the iron oxide clusters (Figure B.7D). The mean hydrodynamic diameter by DLS of these Au coated iron oxide nanoclusters was 51 nm DLS (Table B.4). At a higher Au^{3+}/Fe ratio of 0.25, the number of Au-coated domains on the iron clusters increased as observed by TEM in Figure B.7B and 7E. Consistent with these thicker coatings, the hydrodynamic diameter increased to 54 nm (Table B.4). At the highest Au^{3+}/Fe ratio of 0.5, the shells became progressively thicker and the mean hydrodynamic diameter increased to 61 nm (Table B.4, TN-Knobby). According to AAS, the final Au/Fe ratio increased monotonically as expected with the initial Au^{3+}/Fe ratio, consistent with the TEM and DLS results.

Based on the final Au/Fe ratio from AAS, the theoretical (assuming a simple spherical core and uniform shell) shell thickness ranged from 0.2 to 0.6 nm, as the Au^{3+}/Fe ratio varied from 0.125 to 0.5. The observed thicknesses by TEM were uneven on the partially coated iron oxide cores. Thus the thicknesses in the coated patches of the surface, on the order of a few nm, were higher than the theoretical mean thickness for a simple core-spherical shell model. The thicker shells determined from DLS include the thickness of the adsorbed polymer on Au coated regions of the nanocluster surface, with an end-to-end distance of 12 nm, and also complications from the non-spherical nanocluster geometry.

The absorbance spectra may be correlated with the morphologies observed by TEM and the diameters by DLS. In Figure B.8B, the absorbance intensity increased in the entire spectral range as the feed Au^{3+}/Fe ratio increased. In addition, the SPR peak shifted to the NIR region as the Au shell thickness was increased. At an Au^{3+}/Fe ratio of 0.5 the maximum in SPR was above 700 nm for the particles with knobby surfaces according to the TEM images in Figure B.7(TN-Knobby, Scheme B.1). The shells were still thin according to the DLS sizes in Figure B.8A. Similar spectral changes with size were found for Au^{3+} precursor added by 5 iterations (Figure B.S1, Table B.S2). The extinction coefficient per weight of gold at 755 nm was observed to decrease as the added Au^{3+}/Fe ratio increased as can be seen in Table B.3.

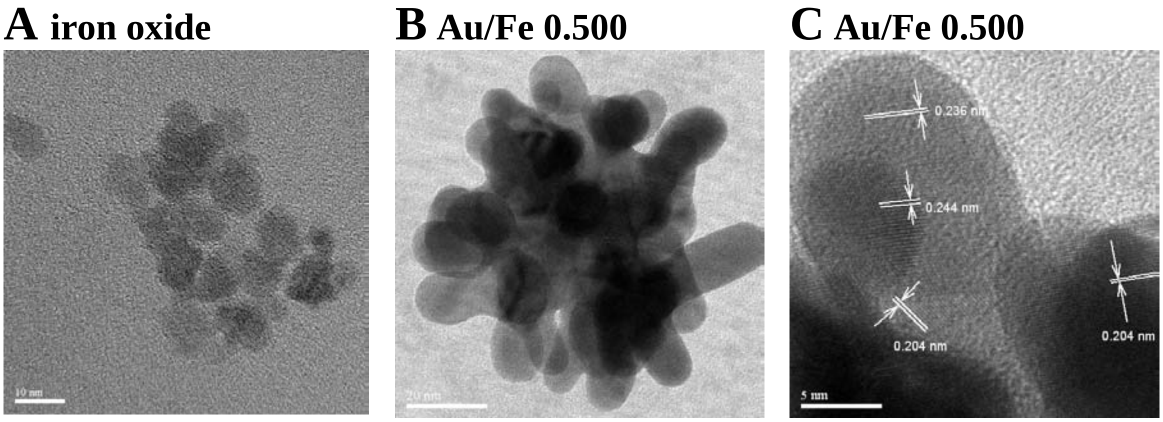

Figure B.6 HRTEM images of iron oxide nanocluster A and gold coated iron oxide nanoparticle B. A magnified image of the upper tip from B indicating thin gold coating on Fe_3O_4 nanoparticles C.

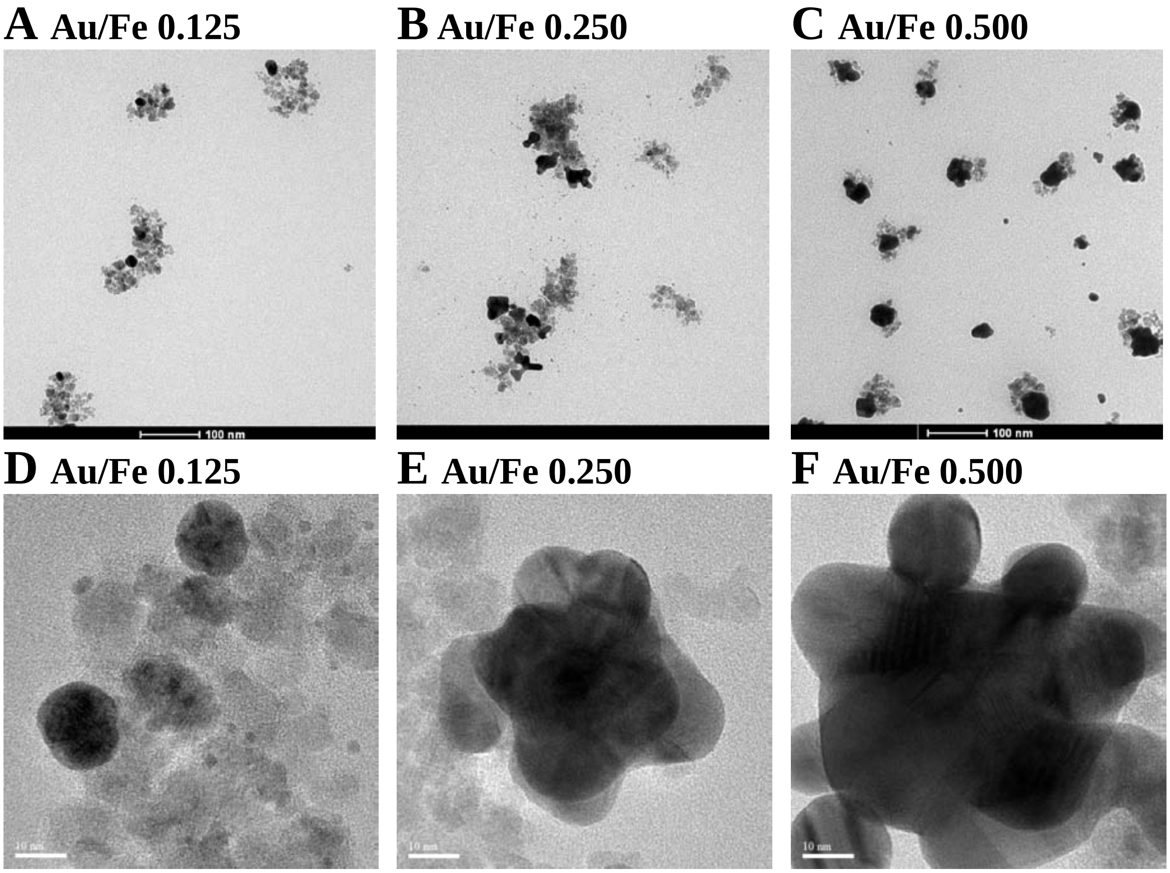
A Au/Fe 0.125 **B** Au/Fe 0.250 **C** Au/Fe 0.500

D Au/Fe 0.125 **E** Au/Fe 0.250 **F** Au/Fe 0.500

Figure B.7 TEM images of the morphology evolution of thin gold shells on iron oxide substrates. Specimens were prepared by taking samples at Au/Fe mass ratio 0.125 (A, D), 0.25 (B, E) and 0.50 (C, F) from the continuous addition of gold precursor experiment and then being separated by centrifugation.

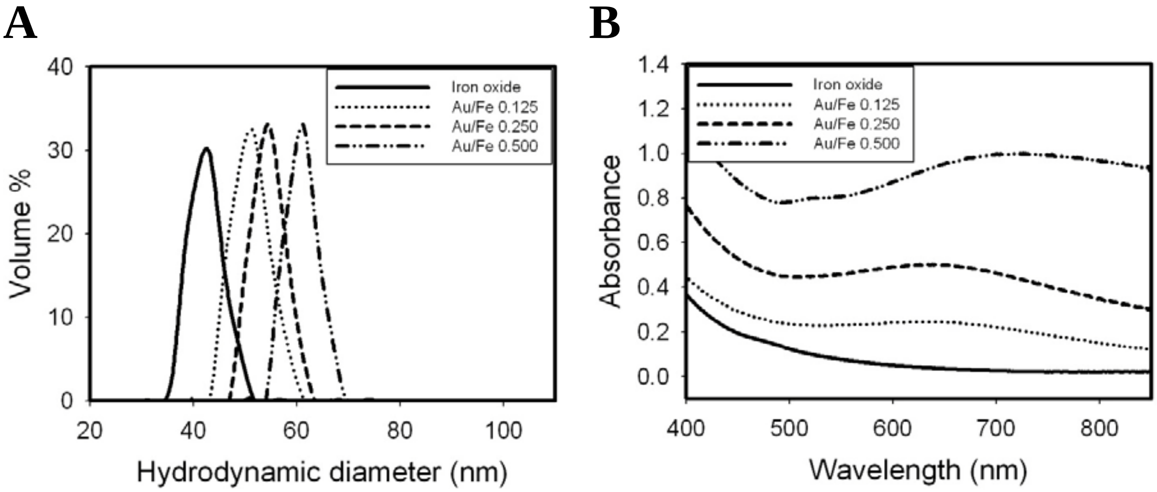

Figure B.8 The evolution of hydrodynamic diameters A with the addition of gold precursor continuously and absorbance spectra B for increased gold to iron ratios accordingly. mPEG-SH/Au mole ratio was fixed at 0.08 for all experiments.

Table B.3 Elemental Analysis of Textured Thin Gold Coated Iron Oxide Nanoparticles by AAS

Au/Fe= 0.5 was reached with continuous addition of Au precursor.

Au/Fe ratio	Final Au/Fe ratio	% Fe yield	% Au yield	Estimated total diameter (nm)	Extinction Coefficient ($cm^2/\mu g$ Au)
0.125	0.145	3.8	4.6	42.3	0.061
0.250	0.281	4.0	5.3	42.5	0.051
0.500	0.691	4.6	7.2	43.2	0.050

Table B.4 Mean Size and Standard Deviation of Textured Thin Gold Coated Iron Oxide Nanoparticles

Au/Fe= 0.5 was reached with continuous addition of Au precursor.

Au/Fe ratio	Mean (nm)	Variance (nm)	% Standard deviation
Iron oxide	42	3.2	7.5
0.125	51	3.4	6.8
0.25	54	3.1	5.7
0.5	61	3.0	4.8

B.3.4 The Separation of Au Coated Iron Oxide Nanoparticles from Uncoated Ones by Centrifugation

The degree of separation of the Au coated and uncoated iron oxide particles may be estimated from the sedimentation coefficient, $S = (1-\rho_1/\rho_2)*m/f$, where ρ_1 is the density of the solvent, ρ_2 and m are the density and the mass of the particle, respectively, and f is the friction factor. The densities of Au coated versus uncoated iron oxide can be very different given the bulk densities of 19.3 and 5.2 g/cm^3 for Au and Fe_3O_4, respectively. The predictions of the model in Table B.S3 indicate that a centrifugation speed on the order of 5,000-6,000 rpm is sufficient to move the Au-coated particles to the bottom of the centrifuge tube in ~ 6 min. However, at this speed the sedimentation of the uncoated particles is relatively low, and thus it should be possible to concentrate the coated particles in the precipitate.

Based on the theoretical predictions, the centrifugation speed, for 6 min, was varied for the case of the particles produced in 5 iterations according to Figure B.9. For each Au^{3+}/Fe ratio, the Au yield in the precipitate increased significantly for an increase in speed from 2,000 to 10,000 rpm, and the yield decreased in the supernatant. The Au yields in the precipitate were higher for the higher initial Au^{3+}/Fe ratios, which produced thicker shells as expected. Thus, these changes in yields were observed in regions of centrifugation speeds as expected from the theoretical predictions of the sedimentation coefficient, based on the Au coatings. The detailed elemental analysis data for Au and Fe before and after centrifugation are shown in Table B.S4. After centrifugation under all conditions, the Fe yield in the precipitates was less than 10% of the total in the nanoclusters prior to separation. From a practical point of view, the uncoated iron oxide may be recycled.

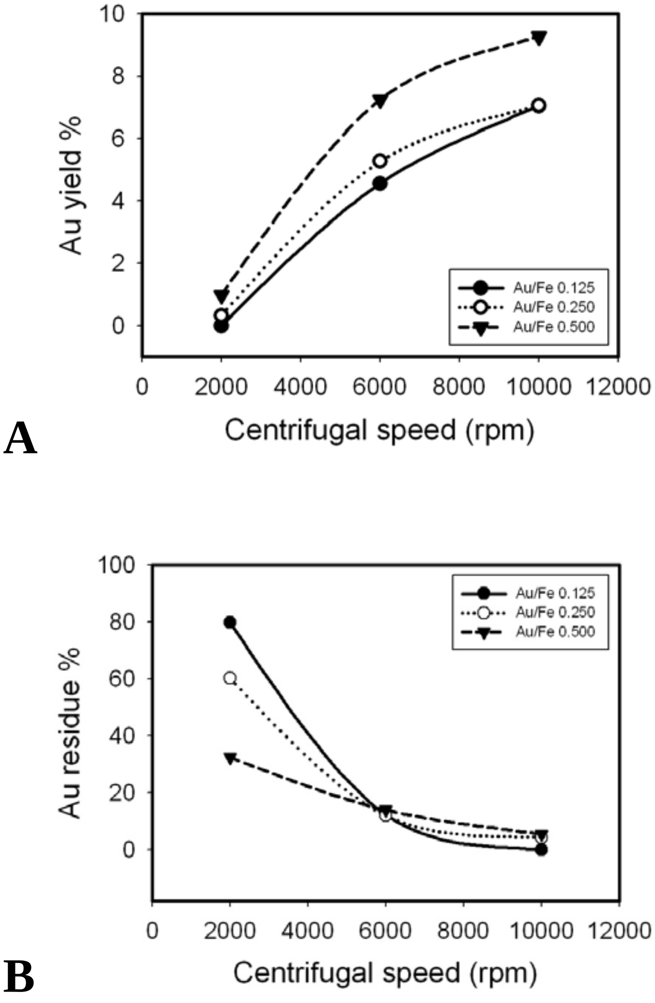

Figure B.9 Au yield in precipitate and Au residue in supernatant after centrifugation at different speed for 6 mins. The yield and residue were calculated as a percentage of initially added gold precursor. Au precursor was added by 5 iterations.

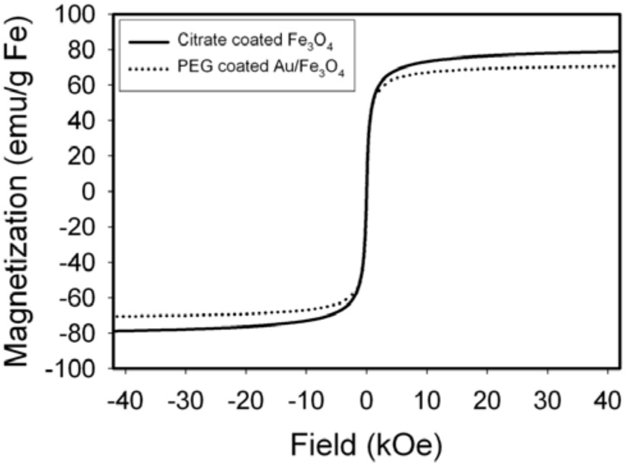

Figure B.10 Normalized magnetization of dried iron oxide nanoclusters and thin gold coated iron oxide nanoparticles at 300K.

B.3.5 Magnetic Properties of the Au Coated Iron Oxide Nanoparticles

The magnetization of dried powders prepared from uncoated iron oxide nanoclusters and Au coated iron oxide nanoclusters synthesized at a total Au^{3+}/Fe ratio 0.5 with 5 iterations (TN-Knobby) after centrifugation was measured by a SQUID at 300 K. The measured magnetization values were normalized by the mass of Fe based on citrate/Fe_3O_4 mass ratio, mPEG-SH/particle ratio determined by TGA analysis and Au/Fe ratio determined by AAS (Figure B.S3, Supporting Information). The magnetization increased rapidly for an applied magnetic field from 0 to ±5 kOe (0.5 Tesla) and reached saturation quickly below 10 kOe (1.0 Tesla) as shown in Figure B.10. The normalized saturation magnetization of Au coated iron oxide nanoparticles is 70 emu/g Fe compared with 78 emu/g Fe for citrate coated iron oxide nanoclusters. Thus, the influence of the thin Au coatings on the iron oxide surfaces produced limited surface defects that potentially may degrade the magnetization. Given the particle Au/Fe ratio of 0.84 from

AAS, the saturation magnetization of TN-Knobby nanoparticles is 32 emu/g particles. This high magnetization per particle weight reflects the unusually high mass fraction of magnetic iron oxide material given the exceptionally thin Au coating, compared to many previous particles with much thicker coatings.[26,98]

B.4 DISCUSSION

In order to explain the range of experimental morphologies shown in Scheme B.1, a general mechanism is presented to describe thin autocatalytic growth on substrates (TAGS). Briefly, the thermodynamic driving force for nucleation and growth is characterized for reduction of Au^{3+} on Au surfaces in contrast with homogeneous reduction in solution. Next, a brief summary of the seeded autocatalytic growth mechanism is presented for formation of pure Au nanoparticles, to serve as background. The primary focus is on the TAGS mechanism to describe the formation of the various thin Au coatings on iron oxide substrates. The discussion ends by relating the behavior of the SPR spectra for the Au coated nanocomposites to the particle morphologies.

B.4.1 Autocatalytic nucleation and growth of pure Au nanoparticles

Hydroxylamine has been used to selectively promote growth of Au on Au surfaces relative to homogeneous nucleation of Au from soluble precursors.[127,128] The cell potential for reduction of Au by hydroxylamine to Au^o on a Au metal surface in eq. (1)

$$2Au^{3+} + 6NH_2OH \Leftrightarrow 3N_2 + 6H_2O + 6H^+ + 2Au^0_{(metal)} \qquad (1)$$

$$2Au^{3+} + 6NH_2OH \Leftrightarrow 3N_2 + 6H_2O + 6H^+ + 2Au^0_{(atom)} \qquad (2)$$

is 1.936 V, based on eqns. (S1) to (S6) in the supplemental section. This potential is far more thermodynamically favorable than the value of -1.244 V to form a single Au^o atom homogeneously described in eq. (2). Thus, hydroxylamine adsorbed on an iron oxide surface may be expected to favor nucleation of Au seeds on the surface, relative to undesired homogeneous nucleation to form pure Au nanoparticles in bulk.

A mechanism of homogenous nucleation to produce Au seeds followed by growth on the seeds has been widely used to synthesize nanoparticles of controlled size with narrow polydispersity.[57] Homogenous nucleation to form Au seeds

$$nAu^{3+} \overset{k_1}{\rightarrow} nAu^0 \ (nucleation) \tag{3}$$

may compete with growth on the Au seeds

$$nAu^{3+} + nAu^0 \overset{k_2}{\rightarrow} 2nAu^0 \ (growth) \tag{4}$$

where n is chosen arbitrarily to define the number of Au atoms in one Au seed. The growth reaction is autocatalytic in that the Au surface in the product is also a reactant. The resulting rate expressions are[59,60]:

$$\frac{d[Au^0]}{dt} = k_1[Au^{3+}] + k_2[Au^{3+}][Au^0] \tag{5}$$

$$[Au^0] = [Au^{3+}]_0 - [Au^{3+}] \tag{6}$$

$$\frac{d[Au^0]}{dt} = k_1[Au^{3+}] + k_2[Au^{3+}]([Au^{3+}]_0 - [Au^{3+}]) \tag{7}$$

where k_1 and k_2 are rate constants for nucleation and growth, respectively, and $[Au^{3+}]_0$ is the initial concentration of precursor. The values if k_2 will be relatively large given the much greater thermodynamic driving force for reduction of Au^{3+} on a Au surface than for homogeneous nucleation. The initial rate of formation of Au^0 by homogeneous nucleation will be slow, given the growth (second term) in eq. (7) will be zero. As Au^0 increases, the contribution the second term in eq. (7) will become prevalent. Eventually when Au^{3+} is highly depleted, the rate slows down progressively, resulting in a well-known sigmoidal shape kinetics curve.[57,59] For a decrease in $[Au^{3+}]_o$, the relative contribution of the growth step becomes smaller in eq.(7) relative to nucleation. For example, after half of $[Au^{3+}]_o$ reacts, the rate is proportional to $k_1 + k_2[Au^{3+}]_o/2$. For a given nucleation rate, a decrease in the growth rate will lead to more nuclei, and thus a larger number of smaller final particles. Thus, a delay in autocatalytic growth provides more separation of nucleation and growth, leading to smaller particles and lower polydispersity in the seeded growth mechanism.[129]

B.4.2 Heterogeneous nucleation and growth of Au shells on substrates for a single iteration at a relatively low Au^{3+}/Fe ratio

The kinetics for formation of Au shells on iron oxide substrate particles exhibited a sigmoidal shape in Figure B.3, as seen in previous studies for pure Au nanoparticles.[57,59] Thus, we chose to extend the model for homogeneous nucleation and growth (eq. 3-4) to the heterogeneous case with substrate particles. An important additional degree of freedom must be considered, the fraction of the iron oxide substrates that become covered with seeds during the nucleation phase, and how this influences subsequent growth. Furthermore, the energy barrier for the formation of Au seeds is lowered by the heterogeneous iron oxide substrate. The barrier is further lowered by the adsorbed hydroxylamine on the iron oxide surfaces.[94]

A mechanism for thin autocatalytic growth on substrates (TAGS) is shown in Scheme B.2 for three levels of separation of nucleation and growth. The substrate (core) may be a nanocluster (brown), or another shape, for example, a sphere (not shown). In each case, the region to the left of the arrow depicts the end of the nucleation phase, prior to the rapid autocatalytic growth to the final product on the right.

The scenario for a Au^{3+}/Fe ratio of 1.5 added in one iteration is given in the top panel in Scheme B.2 and the first column in Table B.5. In the experiments in Figure B.1-3, a Au^{3+}/Fe ratio of 1.5 provided nucleation of Au seeds on a very limited number of iron oxide nanoparticles, as indicated by TEM. Given the high $[Au^{3+}]_0$, for an Au^{3+}/Fe ratio above 1.5[94], the autocatalytic growth rate is relatively high as given by the second term of eq. (7). Therefore, the time for nucleation to produce Au seeds is short before the autocatalytic growth on the seeds becomes dominant. Given the short nucleation time, Au seeds are deposited on a small fraction of the substrate particles as indicated schematically. Rapid growth on a small number of substrates, or equivalently, relatively small separation between nucleation and growth, results in relatively thick shells as shown in Figure B.1D and top panel of Scheme B.2. These TK-Smooth (Scheme B.1) Au shells (~ 10 nm) are commonly observed as Au^{3+}/Fe ratios are typically > 1.5.[26,94,97-100]

The middle panel in Scheme B.2 describes the behavior at a lower Au^{3+}/Fe ratio of 0.125-0.5 and a single iteration of precursor addition. The second column in Table B.5 describes this behavior relative to the higher Au^{3+}/Fe ratios in the top panel. For slower autocatalytic growth at a lower Au^{3+}/Fe ratio, Au seeds are nucleated on more iron oxide substrate particles. Here the transition time from nucleation to growth is longer. The longer nucleation time allows deposition of Au seeds on a larger fraction of substrate particles, and thus, a smaller number of seeds on each substrate. Upon spreading the Au seeds on more substrate particles, the amount of Au per substrate (shell thickness) decreases upon completion of growth. This mechanism is consistent with the thinner shells as shown experimentally in Figure B.1C, 4A and Scheme B.2, relative to the thicker shells in the top panel at higher Au^{3+}/Fe ratios. Thus, greater separation between nucleation to form Au seeds on the substrate and autocatalytic growth at a lower Au^{3+}/Fe ratios, and consequently lower supersaturation, is a novel strategy to form extremely thin shells. Although TN-Smooth (Scheme B.1) Au shells have been achieved on small iron oxide substrates (~10 nm diameter)[95,96,137,149-151] with low MW ligands, they have not been reported for substrates larger than 20 nm, where polymeric stabilizers are needed.

B.4.3 Heterogeneous nucleation and growth of Au shells on substrates with iterative or continuous Au^{3+} addition

Given the decrease in the shell thickness with a decrease in $[Au^{3+}]_0$ for the first two panels in Scheme B.2 and in Figure B.2, it would seem desirable to continue this trend further. However the total amount of final Au deposited would become too low. To overcome this stoichiometric limitation, Au^{3+} may be fed to the system in multiple iterations or continuously but at much higher Au^{3+}/Fe ratios.[94] Here we explain this strategy with the TAGS mechanism, as the very thin shells in Figure B.6 have rarely been reported for substrates > 20 nm. For this comparison, the middle panel is to the bottom panel as the first column is to the second column in Table B.5. The early $[Au^{3+}]$ values are extremely low such that Au seeds may be nucleated on iron oxide substrates with minimal growth, as shown in Figure B.7D, and the bottom panel in Scheme B.2. After each iteration Au^{3+} is depleted, the next iteration produces a very small increase of Au. If little Au^{o} surface is present, the new iteration will grow more seeds predominantly, still with limited transition to autocatalytic growth (eq. 7) as shown in the bottom panel of Scheme B.2 and in high resolution TEM in Figure B.7 for low Au^{3+}/Fe ratios. With delayed autocatalytic growth, the Au seeds are deposited on an even larger fraction of iron oxide nanoclusters than for a single iteration (middle panel), and with fewer Au seeds deposited per particle (Figure B.7A versus Figure B.4A). Thus, Au shells grew on more substrate particles for a constant overall Au^{3+}/Fe ratio of 0.5, resulting in thinner shells as shown in Figure B.4 and Table B.2. This sequence is shown experimentally in Figure B.7 with high resolution TEM for continuous addition.

In addition to tuning shell thickness with multiple iterations or continuous Au addition, the shape may also be manipulated, as shown experimentally in Figure B.4 and in the bottom panel of Scheme B.2. The shape is controlled by the spatial distribution of nuclei deposited on each substrate particle. The relatively large number of Au seeds nucleated on each seeded substrate particle in the middle panel (relative to the lower panel) led to round shells during growth (Figure B.4A). For the same total Au^{3+}/Fe of 0.5, under continuous Au^{3+} addition, the smaller number of seeds on each substrate (Figure B.7A), provided more asymmetric sites for Au growth. Subsequent asymmetric growth led to knobby protrusions on a thin shell, as shown schematically in the bottom panel of Scheme B.2 and the final particle morphology in Figure B.7C and F. The greater fraction of coated substrate particles with Au seeds for continuous addition also plays a significant role. With less growth of Au per particle, the tendency of knobby shapes to be filled in to minimize interfacial area is lower than in the case of one iteration, where autocatalytic growth is more prevalent. To our knowledge, the formation of TN-Knobby shells (Scheme B.1) by tuning the separation of nucleation and growth with low supersaturation values has not been reported previously.

In TAGS, a bimodal distribution of coated and uncoated particles is produced intentionally. The uncoated iron oxide substrate serve as a reservoir for nucleation of Au seeds at low Au^{3+}/Fe ratios to inhibit the autocatalytic growth of Au to form thick shells. After reaction, the coated particles are concentrated in the precipitate during centrifugation. The polydispersity in hydrodynamic diameter of these coated particles was very low (Table B.2 and 4), indicating good separation between nucleation and growth, and prevention of aggregation by the polymer coatings.

B.4.4 Passivation and steric stabilization with mPEG-thiol

The Au coated particles would not be stable against aggregation without steric stabilization, except for the case of the TN-partial particles with very small amounts of Au. The destabilizing attractive VDW forces between the iron oxide nanoclusters (without Au) are lowered in part by the porosity in the nanoclusters, and electrostatic repulsion from the citrate ions. Once the fraction of Au on the substrates becomes significant, the much stronger VDW forces for the Au versus iron oxide often cause aggregation.[97] In a recent study, 30 nm Au coated iron oxide nanoclusters with ~ 83% Au have been stabilized with physisorbed dextran (MW 10,000) on the surface.[2]

A chemically bound stabilizer such as mPEG-SH[141] with an end to end distance of 12 nm was found to be sufficient to provide particle stabilization. By assuming a complete monolayer of mPEG-SH (MW 20,000) on a 50 nm spherical Au nanoparticle surface, the estimated mPEG-SH/Au mole ratio would be 0.006 (Supporting Information). Thus, a higher mPEG-SH/Au^{3+} feed mole ratio of 0.08 was chosen for all Au coating experiments. mPEG-SH does not bind significantly to Fe_3O_4, which otherwise could inhibit nucleation of Au seeds on the surface. During TAGS, the polymer binds to the growing Au surfaces and provides passivation to prevent excessive growth. However the spaces between the anchored polymeric chains do not overinhibit growth, which is quite different from previous papers for heavily coated cores.[95,137] As these surfaces are partially passivated by polymer, nucleation to form Au seeds at new sites on Fe_3O_4 are favored. Another interesting effect is that the time for polymer diffusion to the Au surfaces increases as the autocatalytic growth rate decreases, by the variation of Au^{3+} concentrations in Table B.5. Thus passivation by polymer may further accentuate the formation of thinner coatings as a function of the transition time from nucleation to growth. Finally, these shifts may also influence particle shape by spreading the Au seeds on more substrate particles.

Table B.5 The effects of Au^{3+} precursor addition profiles

Property	Faster growth on Au seeds	Slower growth on Au seeds
Initial Au^{3+}/Fe ratio (supersaturation)	Higher	Lower
Autocatalytic growth rate in early stage	Faster (less time for seed nucleation)	Slower (more time for seed nucleation)
Transition from nucleation to growth	Sooner (less separation between nucleation and growth)	Later (more separation between nucleation and growth)
Shell thickness	Thicker (e.g. rounder shells)	Thinner (e.g. knobby shells)
Role of polymer	Less time to adsorb and less restriction on growth	More time to adsorb and more restriction on growth (favors new nucleation)
Au yield in precipitate after centrifugation	Larger	Smaller

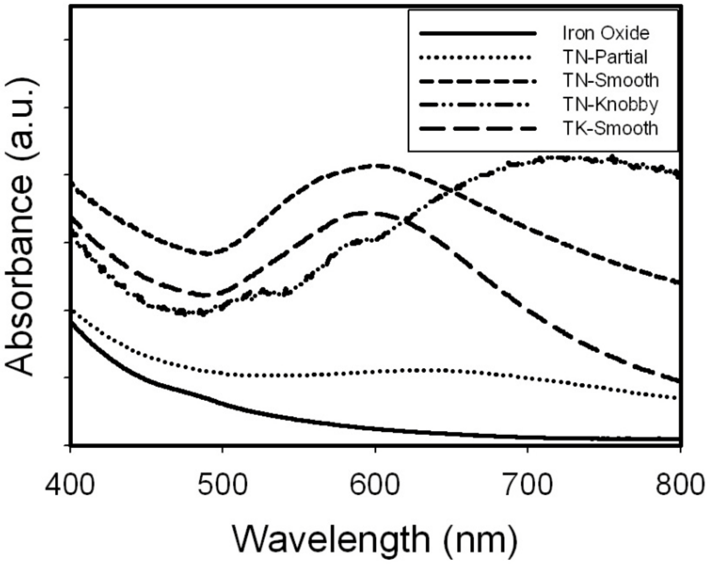

Figure B.11 SPR spectra evolution from uncoated iron oxide nanoclusters to Au coated particles with different shell thickness and geometry. The arbitrary absorbance units were chosen to illustrate the spectra changes of the 4 particle classes shown in Scheme B.1.

Table B.6 Particle properties for different classes

	TN-Partial Figure B.7A	TN-Knobby Figure B.4C	TN-Smooth Figure B.4A	TK-Smooth Figure B.1D
Initial Au^{3+}/Fe mass ratio	0.125	0.5	0.5	1.5
Au^{3+} iterations	1	5	1	1
Final Au/Fe mass ratio	0.15	0.84	2.40	5.09
Extinction Coefficient (cm^2/μg Au)	0.061	0.050	0.040	0.029
Cross-section (10^{-15} m^2)	0.298	1.421	3.202	5.047
Hydrodynamic diameter (nm)	51	57	61	73
Absorbance peak max (nm)	Flat	730	620	600

B.4.5 SPR Spectra for various particle morphologies

Mie theory may be used to predict shifts in the SPR of a uniform Au shell on a spherical core with a given permittivity as a function of R_{total}/ R_{core}. Asymmetry in geometry from spherical Au nanoparticles produces hybridization between dipoles, quadrupoles and higher modes that cause spectral shifts to the NIR region.[24,26] For a peak maximum of 700 nm, R_{total}/ R_{core} < 1.2 is required for a silica core with a permittivity of 2.0.[141] For an Fe_3O_4 core with a permittivity in the range of 5.5 - 6.1,[26] this value is R_{core} < 1.25 on the basis of calculations and experiments for an Au_2S core with a permittivity of 5.4.[142-144] For 2-3 nm Au shells on small iron oxide cores (< 10 nm diameter) R_{total}/ R_{core} is too large for NIR absorbance.[95,96,137,149-151] Likewise, for relatively thin 5 nm Au shells on 18 nm iron oxide cores, where R_{total}/ R_{core} = 1.56, the SPR peak maximum was 590 nm.[139] The SPR peak of TK-Smooth nanoparticles with thicker Au shells (>20 nm) on small 9 nm iron oxide spherical cores was below 580 nm (Figure B.11),[94] and approached that of pure Au spheres. In nearly all of these syntheses for cores in the range of 10 to 60 nm where autocatalytic growth led to shells such that $R_{total}/ R_{core}> 1.25$, the absorbance was limited in the NIR region.

Highly asymmetric cores may provide significant absorbance in the NIR for particles with smooth shells. Such behavior was observed for >8.5 nm thick Au shells on relatively large non-spherical iron oxide substrates (50-60 nm faceted or cubic).[26,98] For our 7 nm smooth Au shells on relatively large 42 nm iron oxide nanocluster cores ($R_{total}/ R_{core} = 1.33$) (TN-Smooth in Scheme B.1, Figure B.1 C and Figure B.4 A), the broad SPR peak shifted to 600 nm with significant absorbance in the NIR region (Figure B.11).

The extremely thin, knobby Au shells on the iron oxide nanocluster cores in Figure B.6B contributed to the strongest absorbance in the NIR region (Scheme B.1, Figure B.11). For spherical 42 nm cores the maximum predicted Au thickness would be 5 nm for $R_{total}/ R_{core} = 1.25$. The Au domains on the nanoclusters were thinner than 5 nm. The asymmetric shell thickness about the nanocluster core surface, as is evident in the knobby protrusions, encompasses attributes of high aspect ratios, as in the case of Au rods and nanorice[111] as well as nanoeggs[112] (asymmetric egg white shells). The combination of all of these asymmetries leads to the very broad NIR absorbance in contrast with sharper peaks for a single mode such as Au nanorods.[28] Related spectral behavior were observed for recently reported asymmetric Au coatings on iron oxide clusters,[2] however, only for a single morphology.

B.5 CONCLUSIONS

Autocatalytic growth of metal shells on metal oxide nanoparticle cores is often excessive as a result of the high metal/metal oxide ratios which are utilized to overcome poor wetting on the low energy substrate. To mitigate the growth, we have introduced a general alternative concept of thin autocatalytic growth on nanparticle substrates (TAGS). The TAGS mechanism may be considered a generalization of the well-known seeded growth mechanism for pure nanoparticles[57,59,127,128] to seeded growth of metals on heterogeneous low energy substrates. Low total metal precursor/metal oxide ratios (0.125-0.50 for Au^{3+}/Fe) are chosen to coat a small fraction of the substrate nanoparticles with unusually thin smooth or thin knobby Au shells (< 5 nm) on a 42 nm iron oxide cores. Multiple iterations or continuous addition of Au^{3+} precursor produce the smallest supersaturation values. During nucleation of Au seeds on a given substrate particle, the slow autocatalytic growth, at low supersaturation values, consumes a smaller amount of Au^{3+}. Consequently, new Au nuclei are seeded on a larger fraction of the iron oxide substrate particles, such that subsequent growth results in thinner shells. In essence, the lower supersaturation provides greater separation of nucleation of seeds and growth on them. Coated particles, with relatively monodisperse hydrodynamic diameters distributions, are separated efficiently from uncoated particles by centrifugation, given the large differences in the densities of Au and iron oxide. A covalently bonded polymer, mPEG-SH, provides steric stabilization against van der Waals attraction, while simultaneousy providing passivation of the growth of the Au coating. The less than 5 nm thin coatings along with asymmetry in shell geometries alter the interactions between plasmon modes and shift the SPR peak to the NIR region, with high cross sections, despite the small overall nanoparticle size. Additional asymmetry is introduced with the nanocluster cores, in contrast with spherical cores. Even further asymmetry and thus the largest red shifts are observed for the highly asymmetric thin knobby shells on nanocluster cores. The thin shells on small nanoparticles produce strong NIR cross sections, while maximizing available effectiveness of the magnetic component. The high degree of multifunctionality in a total particles smaller than 60 nm is desirable for optical, magnetic or multimodal imaging and therapy, with effective permeation of biological barriers.[1,2,52,54,81,108,123,138,145-147]

B.6 SUPPORTING INFORMATION

B.6.1 Iron Oxide Nanocluster Synthesis

0.86 g $FeCl_2$ and 2.35 g $FeCl_3$ were dissolved completely in 40 ml deionized (DI) water by sonication. 0.05 g citric acid was dissolved in 2 ml DI water. Both these solutions were injected into a 3-necked reaction flask that had been evacuated twice and nitrogen flow was maintained during the reaction to avoid oxygen. The reactant solution was stirred and heated up to 95°C, and 10 ml of ammonia (28-30%) was injected to initiate Fe_3O_4 nucleation. After one hour, the reactor was cooled down to room temperature slowly and the product was centrifuged at 6000 rpm for 6 minutes. The resulting completely clear supernatant was decanted and the precipitated particles were re-dispersed by probe sonication in 25 ml of buffer solution containing citric acid (20 mg/ml) with NaOH at a pH of 5.2. This centrifugation and re-dispersion procedure was repeated 2 more times until all the particles were well dispersed in the buffer solution. The dispersion was then dialyzed against DI water for 24 hours using a 25 kDa dialysis bag (Spectra/Pro 7, Spectrum Laboratories Inc.) to remove excess citrate.

Table B.S1 Mean Size and Standard Deviation of Gold Coated Iron Oxide Nanoparticles in Figure B.2.

Au^{3+}/Fe ratio	Mean (nm)	Variance (nm)	% Standard deviation
0.125	44	2.9	7.0
0.250	49	3.1	6.5
0.500	57	3.0	5.3
1.5	73	4.6	6.3
3.0	73 and 146	2.5 and 5.6	3.4 and 3.8
6.0	30 and 159	1.9 and 15.6	6.3 and 9.8

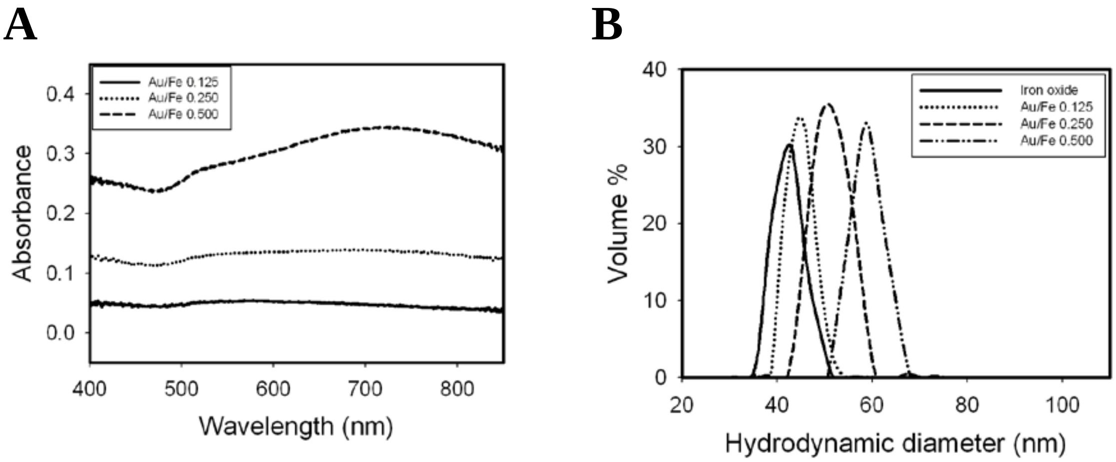

Figure B.S1 The evolution of absorbance spectra and hydrodynamic diameters at selected step of the 5 iteration addition of gold precursor at a total Au/Fe mass ratio of 0.50. Iteration sequence: Au/Fe mass ratio = 0.05, 0.10, 0.125, 0.25, 0.5.

Table B.S2 Mean Size and Standard Deviation of Textured Thin Gold Coated Iron Oxide Nanoparticles
Au/Fe= 0.5, reached with 5 Iterations

Au/Fe ratio	Mean (nm)	Variance (nm)	% Standard deviation
Iron oxide	42	3.2	7.5
0.125	45	2.8	6.1
0.25	51	3.6	7.0
0.5	58	3.3	5.7

B.6.2 The estimation of gold shell thickness on the iron oxide nanoclusters

The Fe_3O_4 nanocluster core was assumed to be a 42 nm diameter (R_{Fe3O4} = 21 nm) sphere with a porosity of $\phi = 0.3$ based on the morphology on TEM images and hydrodynamic diameters measured by DLS. 70 % of the entire volume of the spherical iron oxide cluster was assumed to be occupied by the Fe_3O_4 primary particles. $V_{Core} = (1-\phi)\ 4/3\ \pi R^3$. The mass of iron oxide cluster (M_{Fe3O4}) can be calculated as $M_{Fe3O4} = V_{Core} \cdot \rho_{Fe3O4}$ with the density of iron oxide $\rho_{Fe3O4} = 5.2 g \cdot cm^{-3}$. Based on Au/Fe mass ratio measured by AAS, the mass of gold coating the iron oxide was calculated M_{Au}= Au/Fe $\cdot V_{Core} \cdot \rho_{Fe3O4} \cdot 0.72$. Knowing the density of gold $\rho_{Au} = 19.8 g \cdot cm^{-3}$, the volume of gold V_{Au} was calculated. The total volume of the coated cluster was calculated $V = V_{Core} + V_{Au}$. By assuming the Au coated cluster to be a perfect sphere, $R_{Au+Fe3O4} = (3V/4\pi)^{1/3}$. The gold shell thickness was calculated as $R_{Au+Fe3O4} - R_{Fe3O4}$.

B.6.3 The estimation of centrifugation speed for particle sedimentation

For a spherical particle, the centrifugation process is governed by sedimentation coefficient without considering diffusion. Therefore, this estimation does not take into account steric or electrostatic interactions between particles.[152]

$S = (1-\rho_1/\rho_2)*m/f$ (1)

ρ_1 = density of the solvent ($g \cdot cm^{-3}$)
ρ_2 = density of the particle ($g \cdot cm^{-3}$)
m = mass of the particle (g)
f = friction factor ($g \cdot s^{-1}$)

The density of solvent was assumed to be close to water at 300K, ρ_1 = 1.0 (g·cm^{-3}). The density of gold coated iron oxide particles was calculated as $\rho_2 = (M_{Au} + M_{Fe3O4})/V$. Knowing the particle diameter (D) and the viscosity of the solvent (η), we can calculate the friction factor f. In this case, a viscosity η = 0.001 kg·m^{-1}s^{-1} from water at 300k was used for diluted particle reactant mixture.

$$f = \pi * \eta * D \qquad (2)$$

η = viscosity of the solvent (kg·m^{-1}s^{-1})

D = particle diameter (m)

$$S = \ln(l_1/l_2)/(\omega^2 * t) \qquad (3)$$

l_1 = initial distance of the particle from the axis of the centrifuge
l_2 = final distance of the particle from the axis of the centrifuge
ω = angular speed of rotation of the centrifuge (s^{-1})
t = time for which the centrifugation is carried out (s)

Assuming the centrifugation duration 360 s, we can calculate the centrifugation speed required to precipitate the particles from initial position to the bottom of the centrifuge tube (I1/I2=3.2/3.97).

B.6.4 The thermodynamic driving force for reduction of Au^{3+} on gold surfaces versus homogeneous reduction in solution

The thermodynamic driving forces of the autocatalytic growth of gold on Au^0 metal and homogeneous nucleation from Au^0 atom can be derived from reduction potentials.

$$Au^+ + e^- \Leftrightarrow Au^0_{(metal)} \tag{S1}$$

$$Au^+ + e^- \Leftrightarrow Au^0_{(atom)} \tag{S2}$$

$$Au^0_{(atom)} \Leftrightarrow Au^0_{(metal)} \tag{S3}$$

The reduction potential versus NHE for Au^0 $_{(metal)}$ /Au$^+$ is 1.68 V and for Au^0 $_{(atom)}$ /Au$^+$ is -1.5 V.[57,153] From eq. (S3) = (S1) - (S2), cell potential of Au^0 $_{(metal)}$/Au^0 $_{(atom)}$ is 3.18 V.

$$Au^{3+} + 3e^- \Leftrightarrow Au^0_{(metal)} \tag{S4}$$

$$Au^{3+} + 3e^- \Leftrightarrow Au^0_{(atom)} \tag{S5}$$

The reduction potential versus NHE for Au^0 $_{(metal)}$ /Au^{3+} is 1 V.[127,153] From eq. (S5) = (S4) – (S3), the reduction potential versus NHE for Au^0 $_{(atom)}$ /Au^{3+} is -2.18 V.

$$N_2 + 2H_2O + 2H^+ + 2e^- \Leftrightarrow 2NH_2OH \tag{S6}$$

The reduction potential versus NHE for NH_2OH/N_2 is -0.936 V.[154]

$$2Au^{3+} + 6NH_2OH \Leftrightarrow 3N_2 + 6H_2O + 6H^+ + 2Au^0_{(metal)} \tag{S7}$$

same as eq. (1)

From eq. (S7) = (S4) - (S6), E_{cell} = 1.936 V.

$$2Au^{3+} + 6NH_2OH \Leftrightarrow 3N_2 + 6H_2O + 6H^+ + 2Au^0_{(atom)} \tag{S8}$$

same as eq. (2)

From eq. (S8) = (S5) - (S6), E_{cell} = -1.244 V.

Table B.S3 Calculated centrifugation speed for sedimentation of gold coated iron oxide nanoparticles

	Au/Fe ratio	Diameter (nm)	Centrifugation (rpm)
Iron oxide	0.00	42.0	8303
Au coated iron oxide	0.84	43.5	6415
	1.30	44.3	5776
	2.40	46.0	4859
	3.80	48.0	4188

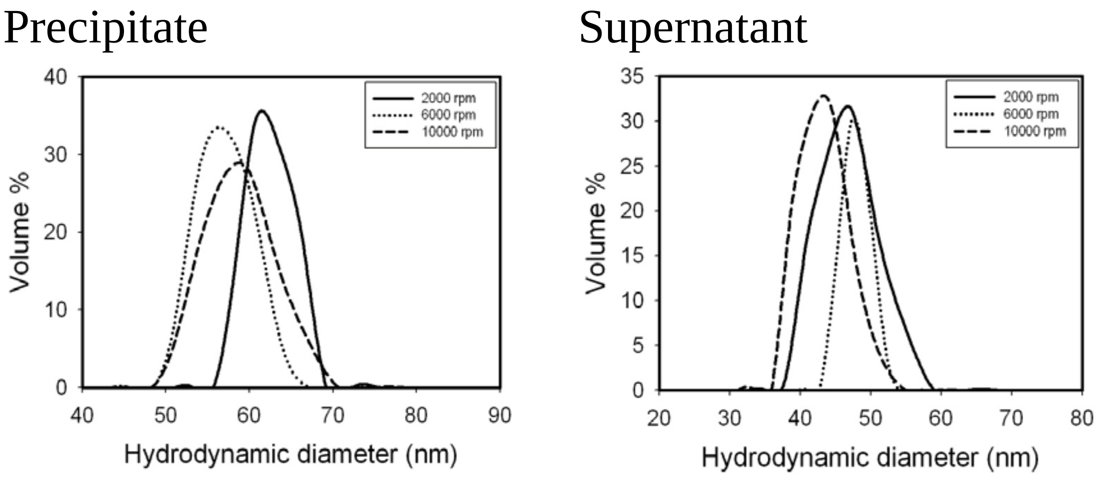
Precipitate

Supernatant

Figure B.S2 Hydrodynamic diameter distribution of nanoparticles in precipitate and supernatant after centrifugation under different speeds. Au precursor was added by 5 iterations at Au/Fe mass ratio 0.500.

The hydrodynamic diameters of nanoparticles in the precipitate and supernatant phases were measured after centrifugation for the case of Au^{3+}/Fe of 0.5. The size distribution of particles in the supernatant was almost identical to that of the uncoated iron oxide nanoclusters. The mean hydrodynamic diameter of Au coated particles in the precipitate at the lowest speed of 2000 rpm were larger than those at the higher speeds, indicating fewer of the smaller particles settled with the weakest centrifugal force.

Table B.S4 Detailed elemental analysis results of Fe and Au before and after centrifugation

Sample	Initial Au/Fe ratio	Final Au/Fe ratio	% Fe yield	% Au yield
0.125 R	0.125	0.094	100.3	88.8
0.25 R	0.250	0.264	100.8	108.6
0.5 R	0.500	0.445	100.4	100.9
0.125 2000 S	0.125	0.093	90.7	79.8
0.125 6000 S	0.125	0.014	92.5	12.2
0.125 10000 S	0.125	0	91.0	0
0.125 2000 P	0.125	0	0.82	0
0.125 6000 P	0.125	0.145	3.83	4.6
0.125 10000 P	0.125	0.095	7.84	7.0
0.25 2000 S	0.250	0.137	106.7	60.3
0.25 6000 S	0.250	0.030	98.2	12.0
0.25 10000 S	0.250	0.011	98.5	4.3
0.25 2000 P	0.250	0.073	1.1	0.3
0.25 6000 P	0.250	0.281	4.0	5.3
0.25 10000 P	0.250	0.176	9.7	7.1
0.5 2000 S	0.500	0.151	94.8	32.5
0.5 6000 S	0.500	0.068	90.8	14.0
0.5 10000 S	0.500	0.028	86.6	5.5
0.5 2000 P	0.500	0.396	1.1	1.0
0.5 6000 P	0.500	0.691	4.6	7.2
0.5 10000 P	0.500	0.465	8.8	9.3

* R indicated reactant before centrifugation
S indicated supernatant after centrifugation
P indicated precipitate after centrifugation

Table B.S5 Mass balance sheet of Fe and Au after centrifugation

		Au/Fe 0.125	Au/Fe 0.25	Au/Fe 0.5
Fe	2000 rpm	92 %	98 %	96 %
	6000 rpm	96 %	93 %	95 %
	10000 rpm	99 %	98 %	95 %
Au	2000 rpm	89.9 %	55.8 %	33.2 %
	6000 rpm	19.4 %	15.3 %	21.1 %
	10000 rpm	7.9 %	10.4 %	14.6 %

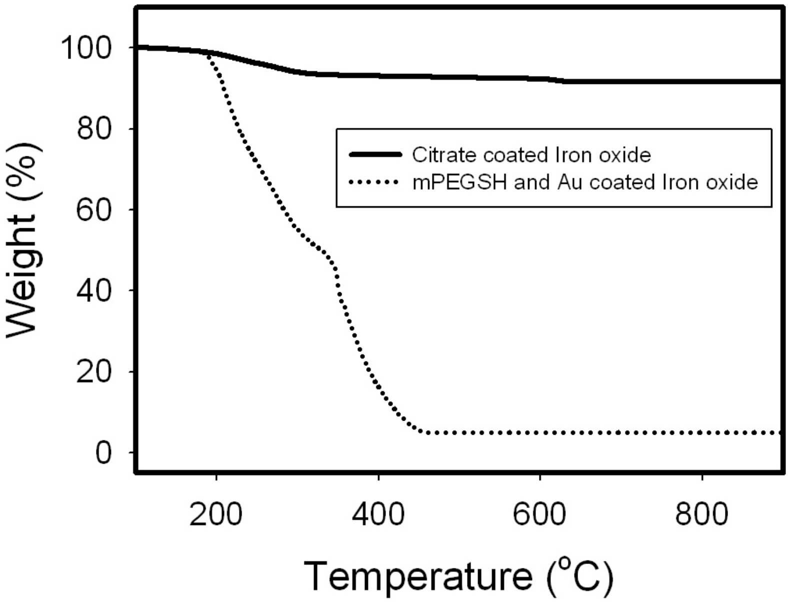

Figure B.S3 TGA measurements of citrate coated iron oxide nanoclusters, mPEG-SH and gold coated iron oxide nanoparticles. At 900 ^{o}C, 9.5 % weight loss occurred from citrate and 95.0 % weight loss occurred from mPEG-SH.

B.7 REFERENCES

(1) Hirsch, L. R.; Stafford, R. J.; Bankson, J. A.; Sershen, S. R.; Rivera, B.; Price, R. E.; Hazle, J. D.; Halas, N. J.; West, J. L. *Proc. Nat. Acad. Sci.* **2003**, *100*, 13549.

(2) Ma, L. L.; Feldman, M. D.; Tam, J. M.; Paranjape, A. S.; Cheruku, K. K.; Larson, T. A.; Tam, J. O.; Ingram, D. R.; Paramita, V.; Villard, J. W.; Jenkins, J. T.; Wang, T.; Clarke, G. D.; Asmis, R.; Sokolov, K.; Chandrasekar, B.; Milner, T. E.; Johnston, K. P. *Acs Nano* **2009**, *3*, 2686.

(3) Mazumder, V.; Chi, M. F.; More, K. L.; Sun, S. H. *Journal of the American Chemical Society* **2010**, *132*, 7848.

(4) Zhang, J.; Sasaki, K.; Sutter, E.; Adzic, R. R. *Science* **2007**, *315*, 220.

(5) Anker, J. N.; Hall, W. P.; Lyandres, O.; Shah, N. C.; Zhao, J.; Van Duyne, R. P. *Nat. Mater.* **2008**, *7*, 442.

(6) Stewart, M. E.; Anderton, C. R.; Thompson, L. B.; Maria, J.; Gray, S. K.; Rogers, J. A.; Nuzzo, R. G. *Chem. Rev.* **2008**, *108*, 494.

(7) Lyon, J. L.; Fleming, D. A.; Stone, M. B.; Schiffer, P.; Williams, M. E. *Nano Letters* **2004**, *4*, 719.

(8) Larson, T. A.; Bankson, J.; Aaron, J.; Sokolov, K. *Nanotechnology* **2007**, *18*, 325101/1.

(9) Aaron, J. S.; Oh, J.; Larson, T. A.; Kumar, S.; Milner, T. E.; Sokolov, K. V. *Optics Express* **2006**, *14*, 12930.

(10) Watzky, M. A.; Finke, R. G. *Journal of the American Chemical Society* **1997**, *119*, 10382.

(11) Ji, X.; Song, X.; Li, J.; Bai, Y.; Yang, W.; Peng, X. *Journal of the American Chemical Society* **2007**, *129*, 13939.

(12) Brown, K. R.; Natan, M. J. *Langmuir* **1998**, *14*, 726.

(13) Brown, K. R.; Walter, D. G.; Natan, M. J. *Chemistry of Materials* **2000**, *12*, 306.

(14) Jana, N. R.; Gearheart, L.; Murphy, C. J. *Chemistry of Materials* **2001**, *13*, 2313.

(15) Yin, Y.; Alivisatos, A. P. *Nature (London, United Kingdom)* **2005**, *437*, 664.

(16) Talapin, D. V.; Rogach, A. L.; Haase, M.; Weller, H. *Journal of Physical Chemistry B* **2001**, *105*, 12278.

(17) Park, J.; Joo, J.; Kwon, S. G.; Jang, Y.; Hyeon, T. *Angew Chem Int Edit* **2007**, *46*, 4630.

(18) Xia, Y.; Xiong, Y. J.; Lim, B.; Skrabalak, S. E. *Angew Chem Int Edit* **2009**, *48*, 60.

(19) Finney, E. E.; Finke, R. G. *Journal of Colloid and Interface Science* **2008**, *317*, 351.

(20) Jeong, U.; Teng, X.; Wang, Y.; Yang, H.; Xia, Y. *Advanced Materials (Weinheim, Germany)* **2007**, *19*, 33.

(21) Zeng, H.; Sun, S. *Advanced Functional Materials* **2008**, *18*, 391.

(22) Lim, J.; Tilton, R. D.; Eggeman, A.; Majetich, S. A. *Journal of Magnetism and Magnetic Materials* **2007**, *311*, 78.

(23) Yu, H.; Chen, M.; Rice, P. M.; Wang, S. X.; White, R. L.; Sun, S. H. *Nano Letters* **2005**, *5*, 379.

(24) Shevchenko, E. V.; Bodnarchuk, M. I.; Kovalenko, M. V.; Talapin, D. V.; Smith, R. K.; Aloni, S.; Heiss, W.; Alivisatos, A. P. *Advanced Materials (Weinheim, Germany)* **2008**, *20*, 4323.

(25) Park, H.-Y.; Schadt, M. J.; Wang, L.; Lim, I. I. S.; Njoki, P. N.; Kim, S. H.; Jang, M.-Y.; Luo, J.; Zhong, C.-J. *Langmuir* **2007**, *23*, 9050.

(26) Xu, Z.; Hou, Y.; Sun, S. *Journal of the American Chemical Society* **2007**, *129*, 8698.

(27) Hostetler, M. J.; Wingate, J. E.; Zhong, C. J.; Harris, J. E.; Vachet, R. W.; Clark, M. R.; Londono, J. D.; Green, S. J.; Stokes, J. J.; Wignall, G. D.; Glish, G. L.; Porter, M. D.; Evans, N. D.; Murray, R. W. *Langmuir* **1998**, *14*, 17.

(28) Leff, D. V.; Ohara, P. C.; Heath, J. R.; Gelbart, W. M. *J Phys Chem-Us* **1995**, *99*, 7036.

(29) Wang, L.; Luo, J.; Fan, Q.; Suzuki, M.; Suzuki, I. S.; Engelhard, M. H.; Lin, Y.; Kim, N.; Wang, J. Q.; Zhong, C.-J. *Journal of Physical Chemistry B* **2005**, *109*, 21593.

(30) Rasch, M. R.; Sokolov, K. V.; Korgel, B. A. *Langmuir* **2009**, *25*, 11777.

(31) Oh, J.; Feldman, M. D.; Kim, J.; Condit, C.; Emelianov, S.; Milner, T. E. *Nanotechnology* **2006**, *17*, 4183.

(32) Levin, C. S.; Hofmann, C.; Ali, T. A.; Kelly, A. T.; Morosan, E.; Nordlander, P.; Whitmire, K. H.; Halas, N. J. *Acs Nano* **2009**, *3*, 1379.

(33) Wang, H.; Brandl, D. W.; Le, F.; Nordlander, P.; Halas, N. J. *Nano Letters* **2006**, *6*, 827.

(34) Goon, I. Y.; Lai, L. M. H.; Lim, M.; Munroe, P.; Gooding, J. J.; Amal, R. *Chemistry of Materials* **2009**, *21*, 673.

(35) Lim, J. K.; Majetich, S. A.; Tilton, R. D. *Langmuir* **2009**, *25*, 13384.

(36) Lim, J.; Eggeman, A.; Lanni, F.; Tilton, R. D.; Majetich, S. A. *Adv Mater* **2008**, *20*, 1721.

(37) Oldenburg, S. J.; Averitt, R. D.; Westcott, S. L.; Halas, N. J. *Chemical Physics Letters* **1998**, *288*, 243.

(38) Kumar, S.; Aaron, J.; Sokolov, K. *Nat. Protocols* **2008**, *3*, 314.

(39) Knight, M. W.; Halas, N. J. *New Journal of Physics* **2008**, *10*.

(40) Hu, Y.; Noelck, S. J.; Drezek, R. A. *Acs Nano* **2010**, *4*, 1521.

(41) Averitt, R. D.; Westcott, S. L.; Halas, N. J. *J Opt Soc Am B* **1999**, *16*, 1824.

(42) Wu, D. J.; Xu, X. D.; Liu, X. J. *Solid State Commun* **2008**, *146*, 7.

(43) Prodan, E.; Nordlander, P.; Halas, N. J. *Nano Letters* **2003**, *3*, 1411.

(44) Huang, X.; El-Sayed, I. H.; Qian, W.; El-Sayed, M. A. *Journal of the American Chemical Society* **2006**, *128*, 2115.

(45) Shah, J.; Park, S.; Aglyamov, S.; Larson, T.; Ma, L.; Sokolov, K.; Johnston, K.; Milner, T.; Emelianov Stanislav, Y. *Journal of biomedical optics* **2008**, *13*, 034024.

(46) Paranjape, A. S.; Kuranov, R.; Baranov, S.; Ma, L. L.; Villard, J. W.; Wang, T.; Konstantin, S.; Feldman, M. D.; Johnston, K. P.; Milner, T. E. *Biomedical Optics Express* **2010**, *1*, 2.

(47) Mehrmohammadi, M.; Oh, J.; Ma, L.; Yantsen, E.; Larson, T.; Mallidi, S.; Park, S.; Johnston, K. P.; Sokolov, K.; Milner, T.; Emelianov, S.; Ieee In *2007 Ieee Ultrasonics Symposium Proceedings, Vols 1-6*; Ieee: New York, 2007, p 652.

(48) Qu, M.; Mallidi, S.; Mehrmohammadi, M.; Ma, L. L.; Johnston, K. P.; Sokolov, K.; Emelianov, S. *Conf Proc IEEE Eng Med Biol Soc* **2009**, *2009*, 4763.

(49) Ferrari, M. *Nature Nanotechnology* **2008**, *3*, 131.

(50) Jiang, W.; Kim, B. Y. S.; Rutka, J. T.; Chan, W. C. W. *Nature Nanotechnology* **2008**, *3*, 145.

(51) Sahoo, Y.; Goodarzi, A.; Swihart, M. T.; Ohulchanskyy, T. Y.; Kaur, N.; Furlani, E. P.; Prasad, P. N. *Journal of Physical Chemistry B* **2005**, *109*, 3879.

(52) Ryoo, W.; Webber, S. E.; Johnston, K. P. *Industrial & Engineering Chemistry Research* **2003**, *42*, 6348.

(53) Fetters, L. J.; Lohse, D. J.; Richter, D.; Witten, T. A.; Zirkel, A. *Macromolecules* **1994**, *27*, 4639.

(54) Caruntu, D.; Cushing, B. L.; Caruntu, G.; O'Connor, C. J. *Chemistry of Materials* **2005**, *17*, 3398.

(55) Lo, C. K.; Xiao, D.; Choi, M. M. F. *Journal of Materials Chemistry* **2007**, *17*, 2418.

(56) Mandal, M.; Kundu, S.; Ghosh, S. K.; Panigrahi, S.; Sau, T. K.; Yusuf, S. M.; Pal, T. *Journal of Colloid and Interface Science* **2005**, *286*, 187.

(57) Weissleder, R. *Science* **2006**, *312*, 1168.

(58) Josephson, L.; Kircher, M. F.; Mahmood, U.; Tang, Y.; Weissleder, R. *Bioconjugate Chemistry* **2002**, *13*, 554.

(59) Hiemenz, P. C.; Rajagopalan, R.; Editors *Principles of Colloid and Surface Chemistry, Third Edition, Revised and Expanded*, 1997.

(60) Gachard, E.; Remita, H.; Khatouri, J.; Keita, B.; Nadjo, L.; Belloni, J. *New J Chem* **1998**, *22*, 1257.

(61) Huang, W.; Tamilmani, S.; Raghavan, S.; Small, R. *Int J Miner Process* **2003**, *72*, 365.

Bibliography

Aaron, J., N. Nitin, et al. (2007). "Plasmon resonance coupling of metal nanoparticles for molecular imaging of carcinogenesis in vivo." Journal of biomedical optics **12**(3).

Aaron, J., K. Travis, et al. (2009). "Dynamic Imaging of Molecular Assemblies in Live Cells Based on Nanoparticle Plasmon Resonance Coupling." Nano Letters **9**(10): 3612-3618.

Aaron, J. S., J. Oh, et al. (2006). "Increased optical contrast in imaging of epidermal growth factor receptor using magnetically actuated hybrid gold/iron oxide nanoparticles." Optics Express **14**(26): 12930-12943.

Adler, D. C., S. W. Huang, et al. (2008). "Photothermal detection of gold nanoparticles using phase-sensitive optical coherence tomography." Optics Express **16**(7): 4376-4393.

Anker, J. N., W. P. Hall, et al. (2008). "Biosensing with plasmonic nanosensors." Nature Materials **7**(6): 442-453.

Arruebo, M., R. Fernandez-Pacheco, et al. (2007). "Magnetic nanoparticles for drug delivery." Nano Today **2**(3): 22-32.

Averitt, R. D., S. L. Westcott, et al. (1999). "Linear optical properties of gold nanoshells." Journal of the Optical Society of America B-Optical Physics **16**(10): 1824-1832.

Bagalkot, V., L. Zhang, et al. (2007). "Quantum dot - Aptamer conjugates for synchronous cancer imaging, therapy, and sensing of drug delivery based on Bi-fluorescence resonance energy transfer." Nano Letters **7**(10): 3065-3070.

Barbosa, S., A. Agrawal, et al. (2010). "Tuning Size and Sensing Properties in Colloidal Gold Nanostars." Langmuir **26**(18): 14943-14950.

Baselga, J. and C. L. Arteaga (2005). "Critical update and emerging trends in epidermal growth factor receptor targeting in cancer." Journal of Clinical Oncology **23**(11): 2445-2459.

Betancourt, T., B. Brown, et al. (2007). "Doxorubicin-loaded PLGA nanoparticles by nanoprecipitation: preparation, characterization and in vitro evaluation." Nanomedicine **2**(2): 219-232.

Boal, A. K., F. Ilhan, et al. (2000). "Self-assembly of nanoparticles into structured spherical and network aggregates." Nature **404**(6779): 746-748.

Brillhart, K. L. and T. T. Ngo (1991). "Use of Microwell Plates Carrying Hydrazide Groups to Enhance Antibody Immobilization in Enzyme Immunoassays." Journal of Immunological Methods **144**(1): 19-25.

Brown, K. R. and M. J. Natan (1998). "Hydroxylamine Seeding of Colloidal Au Nanoparticles in Solution and on Surfaces." Langmuir **14**(4): 726-728.

Brown, K. R., D. G. Walter, et al. (2000). "Seeding of colloidal Au nanoparticle solutions. 2. Improved control of particle size and shape." Chemistry of Materials **12**(2): 306-313.

Brust, M., M. Walker, et al. (1994). "Synthesis of thiol-derivatised gold nanoparticles in a two-phase Liquid?Liquid system." Journal of the Chemical Society, Chemical Communications(7): 801.

Caruntu, D., B. L. Cushing, et al. (2005). "Attachment of Gold Nanograins onto Colloidal Magnetite Nanocrystals." Chemistry of Materials **17**(13): 3398-3402.

Champion, J. A., Y. K. Katare, et al. (2007). "Making polymeric micro- and nanoparticles of complex shapes." Proceedings of the National Academy of Sciences of the United States of America **104**(29): 11901-11904.

Cho, E. C., L. Au, et al. (2010). "The Effects of Size, Shape, and Surface Functional Group of Gold Nanostructures on Their Adsorption and Internalization by Cells." Small **6**(4): 517-522.

Chow, M. K. and C. F. Zukoski (1994). "GOLD SOL FORMATION MECHANISMS - ROLE OF COLLOIDAL STABILITY." Journal of Colloid and Interface Science **165**(1): 97-109.

Dames, P., B. Gleich, et al. (2007). "Targeted delivery of magnetic aerosol droplets to the lung." Nature Nanotechnology **2**(8): 495-499.

Daniel, M. C. and D. Astruc (2004). "Gold nanoparticles: Assembly, supramolecular chemistry, quantum-size-related properties, and applications toward biology, catalysis, and nanotechnology." Chemical Reviews **104**(1): 293-346.

Davis, M. E., Z. Chen, et al. (2008). "Nanoparticle therapeutics: an emerging treatment modality for cancer." Nature Reviews Drug Discovery **7**(9): 771-782.

Decuzzi, P., R. Pasqualini, et al. (2009). "Intravascular Delivery of Particulate Systems: Does Geometry Really Matter?" Pharmaceutical Research **26**(1): 235-243.

Douma, K., L. Prinzen, et al. (2009). "Nanoparticles for Optical Molecular Imaging of Atherosclerosis." Small **5**(5): 544-557.

Durr, N. J., T. Larson, et al. (2007). "Two-photon luminescence imaging of cancer cells using molecularly targeted gold nanorods." Nano Letters **7**(4): 941-945.

Farokhzad, O. C. and R. Langer (2006). "Nanomedicine: Developing smarter therapeutic and diagnostic modalities." Advanced Drug Delivery Reviews **58**(14): 1456-1459.

Ferrari, M. (2005). "Cancer nanotechnology: Opportunities and challenges." Nature Reviews Cancer **5**(3): 161-171.

Ferrari, M. (2008). "Beyond drug delivery." Nature Nanotechnology **3**(3): 131-132.

Fetters, L. J., D. J. Lohse, et al. (1994). "Connection between Polymer Molecular-Weight, Density, Chain Dimensions, and Melt Viscoelastic Properties." Macromolecules **27**(17): 4639-4647.

Finney, E. E. and R. G. Finke (2008). "Nanocluster nucleation and growth kinetic and mechanistic studies: A review emphasizing transition-metal nanoclusters." Journal of Colloid and Interface Science **317**(2): 351-374.

Gachard, E., H. Remita, et al. (1998). "Radiation-induced and chemical formation of gold clusters." New Journal of Chemistry **22**(11): 1257-1265.

Ghose, T. I., A. H. Blair, et al. (1983). "Preparation of Antibody-Linked Cyto-Toxic Agents." Methods in Enzymology **93**: 280-333.

Goia, D. V. and E. Matijevic (1999). "Tailoring the particle size of monodispersed colloidal gold." Colloids and Surfaces a-Physicochemical and Engineering Aspects **146**(1-3): 139-152.

Goldstein, N. I., M. Prewett, et al. (1995). "Biological efficacy of a chimeric antibody to the epidermal growth factor receptor in a human tumor xenograft model." Clinical Cancer Research **1**(11): 1311-1318.

Goon, I. Y., L. M. H. Lai, et al. (2009). "Fabrication and Dispersion of Gold-Shell-Protected Magnetite Nanoparticles: Systematic Control Using Polyethyleneimine." Chemistry of Materials **21**(4): 673-681.

Gopalan, B., I. Ito, et al. (2004). "Nanoparticle based systemic gene therapy for lung cancer: Molecular mechanisms and strategies to suppress nanoparticle-mediated inflammatory response." Technology in Cancer Research & Treatment **3**(6): 647-657.

Grabar, K. C., K. J. Allison, et al. (1996). "Two-dimensional arrays of colloidal gold particles: A flexible approach to macroscopic metal surfaces." Langmuir **12**(10): 2353-2361.

Gratton, S. E. A., P. A. Ropp, et al. (2008). "The effect of particle design on cellular internalization pathways." Proceedings of the National Academy of Sciences of the United States of America **105**(33): 11613-11618.

Gupta, P., C. K. Hall, et al. (1998). "Effect of denaturant and protein concentrations upon protein refolding and aggregation: A simple lattice model." Protein Science **7**(12): 2642-2652.

Han, M. Y., C. H. Quek, et al. (1999). "A simple and effective chemical route for the preparation of uniform nonaqueous gold colloids." Chemistry of Materials **11**(4): 1144-1147.

Hiemenz, P. C. and R. Rajagopalan (1997). Principles of Colloid and Surface Chemistry. New York, Marcel Dekker, Inc.

Hiemenz, P. C., R. Rajagopalan, et al. (1997). Principles of Colloid and Surface Chemistry, Third Edition, Revised and Expanded.

Hirsch, L. R., R. J. Stafford, et al. (2003). "Nanoshell-mediated near-infrared thermal therapy of tumors under magnetic resonance guidance." Proceedings of the National Academy of Sciences of the United States of America **100**(23): 13549-13554.

Hirsch, L. R., R. J. Stafford, et al. (2003). "Nanoshell-mediated near-infrared thermal therapy of tumors under magnetic resonance guidance." Proc. Nat. Acad. Sci. **100**(23): 13549-13554.

Hostetler, M. J., J. E. Wingate, et al. (1998). "Alkanethiolate gold cluster molecules with core diameters from 1.5 to 5.2 nm: Core and monolayer properties as a function of core size." Langmuir **14**(1): 17-30.

Hu, Y., S. J. Noelck, et al. (2010). "Symmetry Breaking in Gold-Silica-Gold Multilayer Nanoshells." Acs Nano **4**(3): 1521-1528.

Huang, W., S. Tamilmani, et al. (2003). "Dissolution of copper thin films in hydroxylamine-based solutions." International Journal of Mineral Processing **72**(1-4): 365-372.

Huang, X., I. H. El-Sayed, et al. (2006). "Cancer Cell Imaging and Photothermal Therapy in the Near-Infrared Region by Using Gold Nanorods." Journal of the American Chemical Society **128**(6): 2115-2120.

Huang, X., X. Peng, et al. (2010). "A Reexamination of Active and Passive Tumor Targeting by Using Rod-Shaped Gold Nanocrystals and Covalently Conjugated Peptide Ligands." Acs Nano.

Jaffer, F. A., P. Libby, et al. (2006). "Molecular and cellular imaging of atherosclerosis - Emerging applications." Journal of the American College of Cardiology **47**(7): 1328-1338.

Jana, N. R., L. Gearheart, et al. (2001). "Evidence for seed-mediated nucleation in the chemical reduction of gold salts to gold nanoparticles." Chemistry of Materials **13**(7): 2313-2322.

Jeong, U., X. Teng, et al. (2007). "Superparamagnetic colloids: controlled synthesis and niche applications." Advanced Materials (Weinheim, Germany) **19**(1): 33-60.

Ji, X., X. Song, et al. (2007). "Size Control of Gold Nanocrystals in Citrate Reduction: The Third Role of Citrate." Journal of the American Chemical Society **129**(45): 13939-13948.

Ji, X. H., X. N. Song, et al. (2007). "Size control of gold nanocrystals in citrate reduction: The third role of citrate." Journal of the American Chemical Society **129**(45): 13939-13948.

Jiang, W., B. Y. S. Kim, et al. (2008). "Nanoparticle-mediated cellular response is size-dependent." Nature Nanotechnology **3**(3): 145-150.

Jiang, Y. Q., N. N. Horimoto, et al. (2009). "Bioimaging with Two-Photon-Induced Luminescence from Triangular Nanoplates and Nanoparticle Aggregates of Gold." Advanced Materials **21**(22): 2309-+.

Jimenez, V. L., D. G. Georganopoulou, et al. (2004). "Hexanethiolate monolayer protected 38 gold atom cluster." Langmuir **20**(16): 6864-6870.

Josephson, L., M. F. Kircher, et al. (2002). "Near-Infrared Fluorescent Nanoparticles as Combined MR/Optical Imaging Probes." Bioconjugate Chemistry **13**(3): 554-560.

Ke, S., X. X. Wen, et al. (2003). "Near-infrared optical imaging of epidermal growth factor receptor in breast cancer xenografts." Cancer Research **63**(22): 7870-7875.

Kim, J. W., E. I. Galanzha, et al. (2009). "Golden carbon nanotubes as multimodal photoacoustic and photothermal high-contrast molecular agents." Nature Nanotechnology **4**(10): 688-694.

Knight, M. W. and N. J. Halas (2008). "Nanoshells to nanoeggs to nanocups: optical properties of reduced symmetry core-shell nanoparticles beyond the quasistatic limit." New Journal of Physics **10**(Oct.).

Knight, M. W. and N. J. Halas (2008). "Nanoshells to nanoeggs to nanocups: optical properties of reduced symmetry core-shell nanoparticles beyond the quasistatic limit." New Journal of Physics **10**.

Kooi, M. E., V. C. Cappendijk, et al. (2003). "Accumulation of ultrasmall superparamagnetic particles of iron oxide in human atherosclerotic plaques can be detected by in vivo magnetic resonance imaging." Circulation **107**(19): 2453-2458.

Kumar, S., J. Aaron, et al. (2008). "Directional conjugation of antibodies to nanoparticles for synthesis of multiplexed optical contrast agents with both delivery and targeting moieties." Nat. Protocols **3**(2): 314-320.

Kumar, S., J. Aaron, et al. (2008). "Directional conjugation of antibodies to nanoparticles for synthesis of multiplexed optical contrast agents with both delivery and targeting moieties." Nature Protocols **3**(2): 314-320.

Kumar, S., J. Aaron, et al. (2008). "Directional conjugation of antibodies to nanoparticles for synthesis of multiplexed optical contrast agents with both delivery and targeting moieties." Nature Protocols **3**(2): 314-320.

Kumar, S., N. Harrison, et al. (2007). "Plasmonic Nanosensors for Imaging Intracellular Biomarkers in Live Cells." Nano Letters **7**(5): 1338-1343.

Kuo, C. H. and M. H. Huang (2005). "Synthesis of branched gold nanocrystals by a seeding growth approach." Langmuir **21**(5): 2012-2016.

Larson, T. A., J. Bankson, et al. (2007). "Hybrid plasmonic magnetic nanoparticles as molecular specific agents for MRI/optical imaging and photothermal therapy of cancer cells." Nanotechnology **18**(32): 325101/325101-325101/325108.

Lazarides, A. A. and G. C. Schatz (2000). "DNA-linked metal nanosphere materials: Structural basis for the optical properties." Journal of Physical Chemistry B **104**(3): 460-467.

Lee, D., R. L. Donkers, et al. (2004). "Electrochemistry and optical absorbance and luminescence of molecule-like Au-38 nanoparticles." Journal of the American Chemical Society **126**(19): 6193-6199.

Leff, D. V., P. C. Ohara, et al. (1995). "Thermodynamic Control of Gold Nanocrystal Size - Experiment and Theory." Journal of Physical Chemistry **99**(18): 7036-7041.

Levin, C. S., C. Hofmann, et al. (2009). "Magnetic-Plasmonic Core-Shell Nanoparticles." Acs Nano **3**(6): 1379-1388.

Li, L. M. and J. Weng (2010). "Enzymatic synthesis of gold nanoflowers with trypsin." Nanotechnology **21**(30).

Lim, J., A. Eggeman, et al. (2008). "Synthesis and single-particle optical detection of low-polydispersity plasmonic-superparamagnetic nanoparticles." Advanced Materials **20**(9): 1721-1726.

Lim, J., R. D. Tilton, et al. (2007). "Design and synthesis of plasmonic magnetic nanoparticles." Journal of Magnetism and Magnetic Materials **311**(1): 78-83.

Lim, J. K., S. A. Majetich, et al. (2009). "Stabilization of Superparamagnetic Iron Oxide Core-Gold Shell Nanoparticles in High Ionic Strength Media." Langmuir **25**(23): 13384-13393.

Lo, C. K., D. Xiao, et al. (2007). "Homocysteine-protected gold-coated magnetic nanoparticles: synthesis and characterization." Journal of Materials Chemistry **17**(23): 2418-2427.

Loo, C., A. Lowery, et al. (2005). "Immunotargeted nanoshells for integrated cancer imaging and therapy." Nano Letters **5**(4): 709-711.

Lu, L. H., K. Ai, et al. (2008). "Environmentally friendly synthesis of highly monodisperse biocompatible gold nanoparticles with urchin-like shape." Langmuir **24**(3): 1058-1063.

Lyon, J. L., D. A. Fleming, et al. (2004). "Synthesis of Fe Oxide Core/Au Shell Nanoparticles by Iterative Hydroxylamine Seeding." Nano Letters **4**(4): 719-723.

Ma, L. L., A. Borwankar, et al. (2011). "Growth of Textured Thin Au Shells on Iron Oxide Nanoparticles." Prepare for Submitting.

Ma, L. L., M. D. Feldman, et al. (2009). "Small Multifunctional Nanoclusters (Nanoroses) for Targeted Cellular Imaging and Therapy." Acs Nano **3**(9): 2686-2696.

Ma, L. L., J. O. Tam, et al. (2011). "Selective Targeting of Antibody Conjugated Multifunctional Nanoclusters (Nanoroses) to Epidermal Growth Factor Receptors in Cancer Cells." Langmuir **27**(12): 7681-7690.

Ma, Y., N. Li, et al. (2005). "One-step synthesis of amino-dextran-protected gold and silver nanoparticles and its application in biosensors." Analytical and Bioanalytical Chemistry **382**(4): 1044-1048.

Maeda, H., J. Fang, et al. (2003). "Vascular permeability enhancement in solid tumor: various factors, mechanisms involved and its implications." International Immunopharmacology **3**(3): 319-328.

Mallidi, S., T. Larson, et al. (2009). "Multiwavelength Photoacoustic Imaging and Plasmon Resonance Coupling of Gold Nanoparticles for Selective Detection of Cancer." Nano Letters **9**(8): 2825-2831.

Mandal, M., S. Kundu, et al. (2005). "Magnetite nanoparticles with tunable gold or silver shell." Journal of Colloid and Interface Science **286**(1): 187-194.

Matijevic, E. (2007). "Nanosize precursors as building blocks for monodispersed colloids." Colloid Journal **69**(1): 29-38.

Matsumura, Y. and H. Maeda (1986). "A New Concept for Macromolecular Therapeutics in Cancer-Chemotherapy - Mechanism of Tumoritropic Accumulation of Proteins and the Antitumor Agent Smancs." Cancer Research **46**(12): 6387-6392.

Mazumder, V., M. F. Chi, et al. (2010). "Core/Shell Pd/FePt Nanoparticles as an Active and Durable Catalyst for the Oxygen Reduction Reaction." Journal of the American Chemical Society **132**(23): 7848-7849.

Mehrmohammadi, M., J. Oh, et al. (2007). Imaging of iron oxide nanoparticles using magneto-motive ultrasound. 2007 Ieee Ultrasonics Symposium Proceedings, Vols 1-6. New York, Ieee**:** 652-655.

Nehl, C. L., H. W. Liao, et al. (2006). "Optical properties of star-shaped gold nanoparticles." Nano Letters **6**(4): 683-688.

Nie, S. M. (2010). "Understanding and overcoming major barriers in cancer nanomedicine." Nanomedicine **5**(4): 523-528.

Ofir, Y., B. Samanta, et al. (2008). "Polymer and biopolymer mediated self-assembly of gold nanoparticles." Chemical Society Reviews **37**(9): 1814-1823.

Oh, J., M. D. Feldman, et al. (2006). "Detection of magnetic nanoparticles in tissue using magneto-motive ultrasound." Nanotechnology **17**(16): 4183-4190.

Oldenburg, S. J., R. D. Averitt, et al. (1998). "Nanoengineering of optical resonances." Chemical Physics Letters **288**(2,3,4): 243-247.

Onn, A., A. M. Correa, et al. (2004). "Synchronous overexpression of epidermal growth factor receptor and HER2-neu protein is a predictor of poor outcome in patients with stage I non-small cell lung cancer." Clinical Cancer Research **10**(1): 136-143.

Oshannessy, D. J., M. J. Dobersen, et al. (1984). "A Novel Procedure for Labeling Immunoglobulins by Conjugation to Oligosaccharide Moieties." Immunology Letters **8**(5): 273-277.

Paranjape, A. S., R. Kuranov, et al. (2010). "Depth resolved photothermal OCT detection of macrophages in tissue using nanorose." Biomedical Optics Express **1**(1): 2-16.

Park, H.-Y., M. J. Schadt, et al. (2007). "Fabrication of Magnetic Core@Shell Fe Oxide@Au Nanoparticles for Interfacial Bioactivity and Bio-separation." Langmuir **23**(17): 9050-9056.

Park, J., J. Joo, et al. (2007). "Synthesis of monodisperse spherical nanocrystals." Angewandte Chemie-International Edition **46**(25): 4630-4660.

Park, J., V. Privman, et al. (2001). "Model of formation of monodispersed colloids." Journal of Physical Chemistry B **105**(47): 11630-11635.

Pease, L. F., J. T. Elliott, et al. (2008). "Determination of Protein Aggregation With Differential Mobility Analysis: Application to IgG Antibody." Biotechnology and Bioengineering **101**(6): 1214-1222.

Pissuwan, D., S. M. Valenzuela, et al. (2007). "Targeted destruction of murine macrophage cells with bioconjugated gold nanorods." Journal of Nanoparticle Research **9**(6): 1109-1124.

Prodan, E., P. Nordlander, et al. (2003). "Electronic structure and optical properties of gold nanoshells." Nano Letters **3**(10): 1411-1415.

Qian, X. M., X. H. Peng, et al. (2008). "In vivo tumor targeting and spectroscopic detection with surface-enhanced Raman nanoparticle tags." Nature Biotechnology **26**(1): 83-90.

Qiu, L., T. A. Larson, et al. (2007). "Single gold nanorod detection using confocal light absorption and scattering spectroscopy." Ieee Journal of Selected Topics in Quantum Electronics **13**(6): 1730-1738.

Qu, M., S. Mallidi, et al. (2009). "Combined photoacoustic and magneto-acoustic imaging." Conf Proc IEEE Eng Med Biol Soc **2009**: 4763-4766.

Rasch, M. R., K. V. Sokolov, et al. (2009). "Limitations on the Optical Tunability of Small Diameter Gold Nanoshells." Langmuir **25**(19): 11777-11785.

Reddy, S. T., M. A. Swartz, et al. (2006). "Targeting dendritic cells with biomaterials: developing the next generation of vaccines." Trends in Immunology **27**(12): 573-579.

Robinson, D. R., Y. M. Wu, et al. (2000). "The protein tyrosine kinase family of the human genome." Oncogene **19**(49): 5548-5557.

Ryoo, W., S. E. Webber, et al. (2003). "Water-in-Carbon Dioxide Microemulsions with Methylated Branched Hydrocarbon Surfactants." Industrial & Engineering Chemistry Research **42**(25): 6348-6358.

Sahoo, Y., A. Goodarzi, et al. (2005). "Aqueous Ferrofluid of Magnetite Nanoparticles: Fluorescence Labeling and Magnetophoretic Control." Journal of Physical Chemistry B **109**(9): 3879-3885.

Schipper, M. L., G. Iyer, et al. (2009). "Particle Size, Surface Coating, and PEGylation Influence the Biodistribution of Quantum Dots in Living Mice." Small **5**(1): 126-134.

Senapati, D., A. K. Singh, et al. (2010). "Real time monitoring of the shape evolution of branched gold nanostructure." Chemical Physics Letters **487**(1-3): 88-91.

Shah, J., S. Park, et al. (2008). "Photoacoustic imaging and temperature measurement for photothermal cancer therapy." Journal of biomedical optics **13**(3): 034024.

Shevchenko, E. V., M. I. Bodnarchuk, et al. (2008). "Gold/iron oxide core/hollow-shell nanoparticles." Advanced Materials (Weinheim, Germany) **20**(22): 4323-4329.

Skrabalak, S. E., J. Chen, et al. (2007). "Gold nanocages for biomedical applications." Advanced Materials **19**(20): 3177-3184.

Sokolov, K., M. Follen, et al. (2003). "Real-time vital optical imaging of precancer using anti-epidermal growth factor receptor antibodies conjugated to gold nanoparticles." Cancer Research **63**(9): 1999-2004.

Stewart, M. E., C. R. Anderton, et al. (2008). "Nanostructured plasmonic sensors." Chemical Reviews **108**(2): 494-521.

Talapin, D. V., A. L. Rogach, et al. (2001). "Evolution of an ensemble of nanoparticles in a colloidal solution: Theoretical study." Journal of Physical Chemistry B **105**(49): 12278-12285.

Tam, J. M., A. K. Murthy, et al. (2010). "Kinetic Assembly of Near-IR-Active Gold Nanoclusters Using Weakly Adsorbing Polymers to Control the Size." Langmuir **26**(11): 8988-8999.

Tam, J. M., J. O. Tam, et al. (2010). "Controlled Assembly of Biodegradable Plasmonic Nanoclusters for Near-Infrared Imaging and Therapeutic Applications." Acs Nano **4**(4): 2178-2184.

Tong, G. J., S. C. Hsiao, et al. (2009). "Viral Capsid DNA Aptamer Conjugates as Multivalent Cell-Targeting Vehicles." Journal of the American Chemical Society **131**(31): 11174-11178.

Trigari, S., A. Rindi, et al. (2011). "Synthesis and modelling of gold nanostars with tunable morphology and extinction spectrum." Journal of Materials Chemistry **21**(18): 6531-6540.

Urbanska, K., B. Romanowska-Dixon, et al. (2002). "Indocyanine green as a prospective sensitizer for photodynamic therapy of melanomas." Acta Biochimica Polonica **49**(2): 387-391.

Van de Broek, B., F. Frederix, et al. (2011). "Shape-controlled synthesis of NIR absorbing branched gold nanoparticles and morphology stabilization with alkanethiols." Nanotechnology **22**(1).

Wang, A. Z., V. Bagalkot, et al. (2008). "Superparamagnetic iron oxide nanoparticle-aptamer bioconjugates for combined prostate cancer imaging and therapy." ChemMedChem **3**(9): 1311-1315.

Wang, H., D. W. Brandl, et al. (2006). "Nanorice: A Hybrid Plasmonic Nanostructure." Nano Letters **6**(4): 827-832.

Wang, L., J. Luo, et al. (2005). "Monodispersed Core-Shell Fe3O4@Au Nanoparticles." Journal of Physical Chemistry B **109**(46): 21593-21601.

Wang, S. P., N. Mamedova, et al. (2002). "Antigen/antibody immunocomplex from CdTe nanoparticle bioconjugates." Nano Letters **2**(8): 817-822.

Wang, W. (2005). "Protein aggregation and its inhibition in biopharmaceutics." International Journal of Pharmaceutics **289**(1-2): 1-30.

Wang, W., X. Yang, et al. (2008). "Growth Mechanism of Flowerlike Gold Nanostructures: Surface Plasmon Resonance (SPR) and Resonance Rayleigh Scattering (RRS) Approaches to Growth Monitoring." Journal of Physical Chemistry C **112**(42): 16348-16353.

Wang, Z. D., J. Q. Zhang, et al. (2010). "DNA-Mediated Control of Metal Nanoparticle Shape: One-Pot Synthesis and Cellular Uptake of Highly Stable and Functional Gold Nanoflowers." Nano Letters **10**(5): 1886-1891.

Watzky, M. A. and R. G. Finke (1997). "Transition metal nanocluster formation kinetic and mechanistic studies. A new mechanism when hydrogen is the reductant: Slow, continuous nucleation and fast autocatalytic surface growth." Journal of the American Chemical Society **119**(43): 10382-10400.

Weissleder, R. (2006). "Molecular Imaging in Cancer." Science **312**(5777): 1168-1171.

Wilcoxon, J. P., J. E. Martin, et al. (1989). "AGGREGATION IN COLLOIDAL GOLD." Physical Review A **39**(5): 2675-2688.

Wu, D. J., X. D. Xu, et al. (2008). "Influence of dielectric core, embedding medium and size on the optical properties of gold nanoshells." Solid State Communications **146**(1-2): 7-11.

Xia, Y., Y. J. Xiong, et al. (2009). "Shape-Controlled Synthesis of Metal Nanocrystals: Simple Chemistry Meets Complex Physics?" Angewandte Chemie-International Edition **48**(1): 60-103.

Xu, M. H. and L. H. V. Wang (2006). "Photoacoustic imaging in biomedicine." Review of Scientific Instruments **77**(4).

Xu, Z., Y. Hou, et al. (2007). "Magnetic Core/Shell Fe3O4/Au and Fe3O4/Au/Ag Nanoparticles with Tunable Plasmonic Properties." Journal of the American Chemical Society **129**(28): 8698-8699.

Yin, Y. and A. P. Alivisatos (2005). "Colloidal nanocrystal synthesis and the organic-inorganic interface." Nature (London, United Kingdom) **437**(7059): 664-670.

Yin, Y. and A. P. Alivisatos (2005). "Colloidal nanocrystal synthesis and the organic-inorganic interface." Nature **437**(7059): 664-670.

Yin, Y. and A. P. Alivisatos (2005). "Colloidal nanocrystal synthesis and the organic–inorganic interface." Nature **437**(7059): 664-670.

Yu, H., M. Chen, et al. (2005). "Dumbbell-like bifunctional Au-Fe3O4 nanoparticles." Nano Letters **5**(2): 379-382.

Zeng, H. and S. Sun (2008). "Syntheses, properties, and potential applications of multicomponent magnetic nanoparticles." Advanced Functional Materials **18**(3): 391-400.

Zhang, J., K. Sasaki, et al. (2007). "Stabilization of platinum oxygen-reduction electrocatalysts using gold clusters." Science **315**(5809): 220-222.

Zhao, L. L., X. H. Ji, et al. (2009). "Formation and Stability of Gold Nanoflowers by the Seeding Approach: The Effect of Intraparticle Ripening." Journal of Physical Chemistry C **113**(38): 16645-16651.

Zhu, J., K. T. Yong, et al. (2010). "Additive controlled synthesis of gold nanorods (GNRs) for two-photon luminescence imaging of cancer cells." Nanotechnology **21**(28).

Zou, X. Q., E. B. Ying, et al. (2006). "Seed-mediated synthesis of branched gold nanoparticles with the assistance of citrate and their surface-enhanced Raman scattering properties." Nanotechnology **17**(18): 4758-4764.